Investigation of Two-dimensional Boron Structures on Metal Surfaces

ファラハナ, ジェスミン, トゥリ

Investigation of Two-dimensional Boron Structures on Metal Surfaces

Farhana Jesmin Tuli

Department of Molecular and Material Sciences

Faculty of Interdisciplinary Graduate School of Engineering Sciences

Kyushu University

Supervised by

Assoc. Prof. Takeshi Nakagawa

A dissertation submitted as part of satisfying the degree of

Doctor of Philosophy

September, 2021

Abstract

This thesis focuses on the investigation of boron (B) growth on two different phases of refractory metals by low energy electron diffraction (LEED), scanning tunneling microscopy (STM), and X-ray photoelectron spectroscopy (XPS) in ultra-high vacuum (UHV) condition. The surface structure and interfacial properties are analyzed in detail. The structural analysis for B adsorbed on W(100) surface revealed a superstructure, W(100) c(2×2)-B, formed on W(100) surface upon B deposition followed by annealing at high temperature. The best-fit structure obtained from LEED structural analysis manifested that B atom positioned at the four-fold hollow site with the coverage of 0.5 ML forming a metal rich boride compound, W_2B, on W(100) surface. The W atoms beneath B atoms moved downward to form B-W bonds for stabilizing the surface atoms. Formation of ordered c(2×2) structure because of B atoms positioning a hollow site of W(100) was evidenced by STM as well. Obtaining a sharp c(2×2) structure after B deposition and annealing required lower coverage of B on W(100) surface, which was determined from XPS measurements as the peak intensity of B1s for that ordered surface was found to be very small. Analyzing the chemical interaction by XPS confirmed B1s peak shifting towards lower binding energy compared to pure B1s peak, indicating the charge transfer from W atom to B atom. The analysis of these experimental results makes it plausible to attribute the W(100) c(2×2)-B superstructure to W_2B ordered surface alloy. On the other hand, a novel phase of two-dimensional (2D) B sheet was grown on Mo(110) surface by depositing pure B at room temperature followed by annealing. STM measurements combined with LEED measurements revealed the formation of χ- type borophene structure which is distinctive from all the earlier reported structures of borophene. This planar B allotrope on Mo(110) was single phased with hexagonal hole density, $\eta = 5/28$. The observation of borophene growth on strongly interacting substrate promotes the interest for synthesizing borophene on various substrates, which can be applicable in future devices.

Preface

The research work on analyzing the surface structures and interfacial properties of boron on refractory metal surfaces is presented in this thesis. In the first chapter, a general overview of the research work with a summary of previous works related to this topic and the motivation for this research work are described.

The background of surface science with the details of experimental procedures, and the materials used for this research to determine the surface properties are discussed in the second chapter.

In the third chapter, the obtained results for B adsorption on W(100) surface are discussed in detail, and the results for the B adsorption on Mo(110) surface are discussed in the fourth chapter.

In the fifth chapter, the summary of experimental results discussed in the previous chapters is delineated.

Another work on investigating interfacial properties of Fe on MoS_2, which is not directly related to my primary research, is described in Appendix.

Table of contents

Abstract ..... **i**

Preface ..... **ii**

Table of contents ..... **iii**

Chapter 1: Introduction **1**

1.1 General overview 2

1.2 Literature review 5

1.3 Motivation of research work 16

Chapter 2: Fundamentals and Methodologies **31**

2.1 Basics of surface crystallography 32

2.1.1 Surface physics 32

2.1.2 Overview of 2D lattice 35

2.1.3 Miller indices 36

2.1.4 Surface relaxation and reconstruction 37

2.1.5 Surface structure notation 41

2.2 Materials 43

2.2.1 Boron 43

2.2.2 Refractory metals 49

2.3 Experiment 53

2.3.1 Low energy electron diffraction (LEED) 55

2.3.2 X-ray photoelectron spectroscopy (XPS) 66

2.3.3 Scanning tunneling microscopy (STM) 69

Chapter 3: B adsorption on W(100) **78**

3.1 Introduction 79

3.2 Experiment and calculation 80

3.3 Results and discussion 82

Chapter 4: B adsorption on Mo(110) **112**

4.1 Introduction 113

4.2 Experiment 114

4.3 Results and discussion 114

Chapter 5: Conclusions and future prospects 128
5.1 Conclusions 129
5.2 Future prospects 131
Appendix 134
Acknowledgements 157

CHAPTER 1:

INTRODUCTION

1.1 General overview

Surfaces and interfaces, known as phase boundaries, play an important role in material performance for the application in nanodevices [1–3]. Several types of surfaces are merged to form various interfaces, such as, solid-solid, solid-liquid, solid-gas, liquid-liquid, and liquid-gas. When any surface of material comes in contact with another phase, its interaction with the other phase initiates alteration of properties for both phases at the interface. Moreover, the surface of a specific phase without any contact shows different characteristics from the bulk properties. In modern surface science, dealing with crystalline surfaces in ultra-high vacuum (UHV) within the thickness ~10 Å, ensures the presence of discrepancy in bulk and surface properties of any material. The deviation in bulk and surface properties is crucial to understand the scientific curiosities and achieving control over these surfaces, which are essential in nanomaterials and future applications.

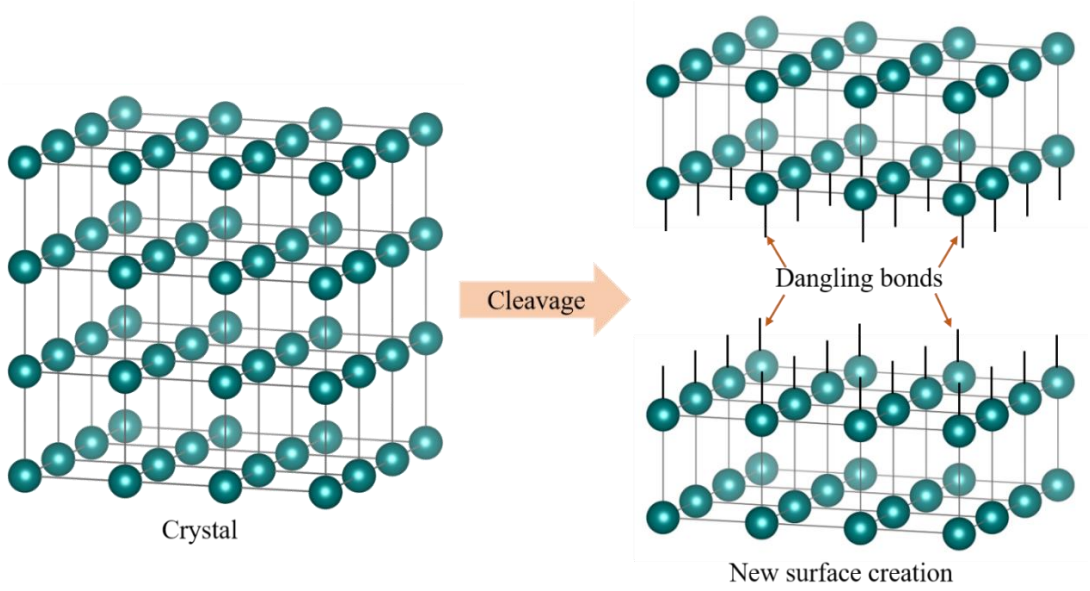

Figure 1.1. Schematic of a simple crystal and the creation of new surfaces.

The reason behind the unusual behavior of the surface is the bonding nature of atoms. The geometric configuration suggests that a crystal forms by the regular arrangement of basic building blocks, including atoms, ions, or molecules. These building blocks stay

together due to the presence of strong and attractive interactions between them. In Figure 1.1, a simple crystal structure is shown assuming that atoms are covalently bonded. Preparing a certain surface, it is necessary to cut the bonds between all the atoms of both sides of the cleavage plane. As shown in Figure 1.1, the atoms of the resulting two new surfaces are deprived of some bonds with previous neighboring atoms. Due to this splitting a crystal into two, surface atoms are only bonded with neighboring atoms of one side and the other side is vacuum while the atoms in bulk are surrounded by all nearest atoms. Consequently, the surface atoms can be accessed freely from the outer side as well as these surface atoms will be the first to be contacted with the atoms or other molecules of different phases. In addition, the energy required to break the bonds will be stored in the 'broken bonds' or 'dangling bonds' of surface atoms. Thus, surface atoms must possess higher energy comparative to the bulk atoms.

However, the formation of surface is not simple truncation of bulk material. The behavior of surface varies depending on the nature of bulk material. The surface of a metal is different from the surface of a semiconductor due to having delocalized electron gas in metal. The bond formed in any metal is not directed like a semiconducting material which inhibits to form dangling bonds on the surface. Therefore, the effect of breaking bonds on the surface is more prominent for the semiconductors. Even though, all crystals will try to reduce the extra energy of surface atoms to become stable. Surface atoms may move closer to the next layer perpendicularly without any parallel movement referred to as 'surface relaxation' or rearrange their atomic arrangement in parallel directions referred to as 'surface reconstruction' to reduce the additional energy. Along with, adsorption of foreign elements, such as atoms or molecules on any clean surface, can create new bonds with surface atoms leading to lower the surface energy by reconstructing the surface structure as well.

While semiconductor surfaces exhibit complex surface reconstruction because of their directional covalent bonding, different mechanism initiates surface relaxation or reconstruction for metal surfaces due to absence of directional bonds. Redistribution of free charge over the metal surfaces experiences charge imbalance which leads to inward

movements of surface layer which is shown in Figure 1.2. With some exception, most of the metal surfaces exhibit surface relaxation.

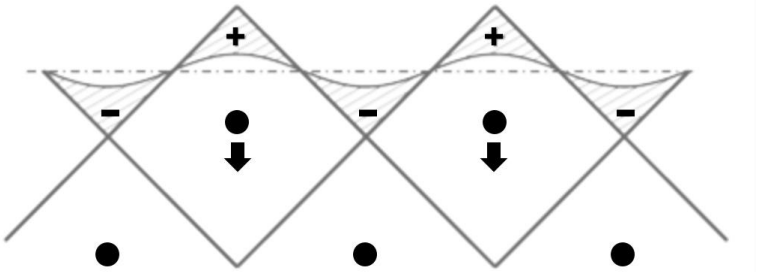

Figure 1.2. Schematic representation of charge distribution of metal surface.

Though, in 'surface relaxation', atomic arrangement for surface layer remains unchanged, 'surface reconstruction' alters the structure of surface layer leading to form new superstructure. It is apparent that structural alteration occurs for the surface and its nearest atoms which will further change the physical and chemical properties of that surface and few layers near the surface from the respective properties of bulk. Thus, investigating the surface properties is very crucial, especially for two-dimensional (2D) materials due to having high surface area. For the past several decades, investigations of solid surfaces were carried out with or without adsorbing foreign materials in UHV conditions. However, adsorbate-induced surface reconstruction has become a significant subject of research due to the formation of new surface alloy or 2D sheet over the surface, which can be used in future applications for enhancing material's performance.

LEED is considered as one of the most powerful techniques to determine the surface structure by using the low energy electrons in the range of 20-1000 eV to limit the penetration depth less than 20 Å. STM is another fascinating technique to visualize the surface structure atom by atom, and the chemical properties of the surface can be determined by using XPS.

Recently, the adsorption of the lightest metalloid, boron (B) on different substrates has drawn tremendous research interests both experimentally and theoretically for analyzing the surface properties. B atom, positioned next to carbon (C), exhibits unique nature and complex bonding configurations due to its electron deficiency which leads to forming multi-center-two-electrons bonds [4]. The formation of multicenter bonds enables to form a vast number of B allotropes, including B_{12} icosahedra, small B clusters, and spuericosahedra in its bulk form [5]. Despite that, small clusters of B can form simple planar or quasiplanar structures, which are different from their 3D bulk structures [5–7]. The formation of planner clusters indicates that B may exhibit many characteristics of its neighboring element, carbon [8,9]. However, fabrication of monolayer B sheet took great research efforts compared to 2D sp^2 hybridized graphene due to the electron-deficient nature of boron atom, making its structures fluxional [10,11]. To overcome the instability of the honeycomb B sheet due to the lack of electron, Tang et al.,[12] predicted the atomically flat B sheet comprising triangular and honeycomb motifs to make the 2D sheet more stable. Moreover, several stable 2D structures of boron were proposed by varying boron vacancy in triangular lattice [13]. In addition, deposition of B on other substrates for fabricating 2D B sheets was proposed for the compensation of electron deficiency [14].

The dependency of B growth on substrates enhances the opportunities to analyze the properties of B adsorbed surface which will help in realizing the surface structure with other properties for employing this in future applications. In this thesis, the growth of B on different substrates is analyzed to realize the surface structure as well as the interaction of B with substrate material at the interface.

1.2 Literature review

After the invention of graphene in 2004 [15], 2D materials including phosphorene [16], antimonene [17], arsenene [18], stanene [19], germanene [20], silicene [21], etc. have drawn tremendous research interests in both experimentally and theoretically because of

their significant physical properties and potential applications in the next generation nanoscale devices [6,22,23]. Recently, 2D boron (B) sheet, referred to as borophene, consisting of B atoms arranged in triangular lattice with hollow hexagons, draws considerable attention due to its intriguing properties, such as high mechanical flexibility [22], metallicity [24], optical transparency [25], presence of Dirac cones [26–29], superconductivity [30,31], magnetism [32] etc. Moreover, the polymorphic nature of borophene thrives the research interest in predicting stable borophene structure with its unique properties [4,7,10,13,14,29,33–36] as well as experimental development of B sheet on different substrates [11,22,37–43]. However, monolayer 2D B sheet cannot be prepared by exfoliating from the bulk materials like graphene and phosphorene, as B does not have layered like bulk counterparts. Thus, synthesis of 2D B sheet is possible by thermal evaporation deposition, chemical vapor deposition (CVD), or molecular beam epitaxy (MBE). Despite the formation of 2D B sheet, the structure of B grown on various substrates is also a matter of interest. Previous studies concerning the effect of substrates as well as their faces for the growth of B are summarized briefly in this section.

More than five decades ago, Tucker conducted his research to understand the interaction of B with various crystalline faces of a refractory metal, tungsten, W. He deposited B by e-beam evaporation on (100), (110), (211), (310) and (111) faces of W crystal and observed that B oriented randomly over all faces at room temperature. No other superstructure was observed after annealing the substrate at a higher temperature except W(100) surface. A superstructure with (2×1) pattern observed on W(100) surface after annealing at 750˚C. On the other hand, for W(111) surface, W atoms at the surface got distorted upon B deposition followed by annealing at 850˚C due to the B atom's orientation in crystallographic positions [44] as shown in Figure 1.3.

In 1987, the interactivity of B with another transition metal, molybdenum, Mo was investigated by XPS. They found that the bonding between B and Mo was dependent on B coverage as B 1s peak position was different for low and high coverage phase [45]. Magkoev et al. [46] observed that B atoms on Mo(110) at room temperature were stable and started to diffuse into the bulk with the increase of annealing temperature and B-Mo bond formed at 1150 K as revealed by XPS results. B nanowire was found to be developed

on Mo(110) surface after exposing borazine onto the substrate by marinating the substrate temperature at 1170 K in 2007 by Allan et al. [47]. They found 1 μm long nanowire with 2-10 nm width by STM and LEED pattern supported STM result as it showed perfect periodicity along a certain direction which is shown in Figure 1.4.

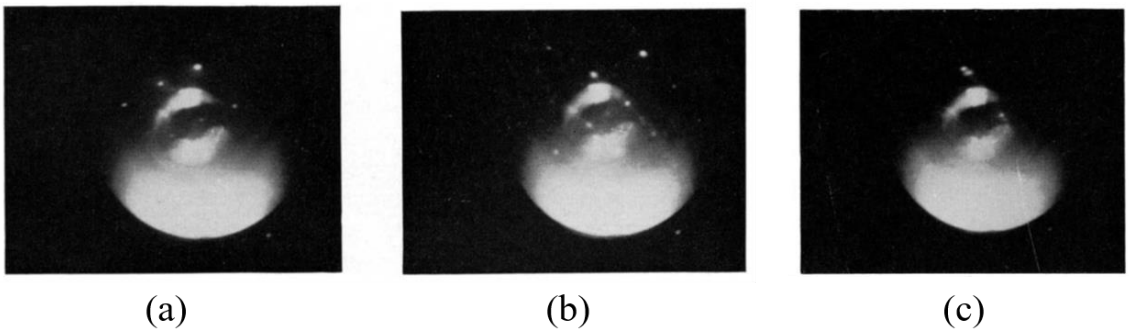

Figure 1.3. LEED patterns of B deposited on (a) W(211) surface after annealed at 500˚C, (b) W(100) surface after annealed at 750˚C, and (c) W(111) surface after annealed at 850˚C [44].

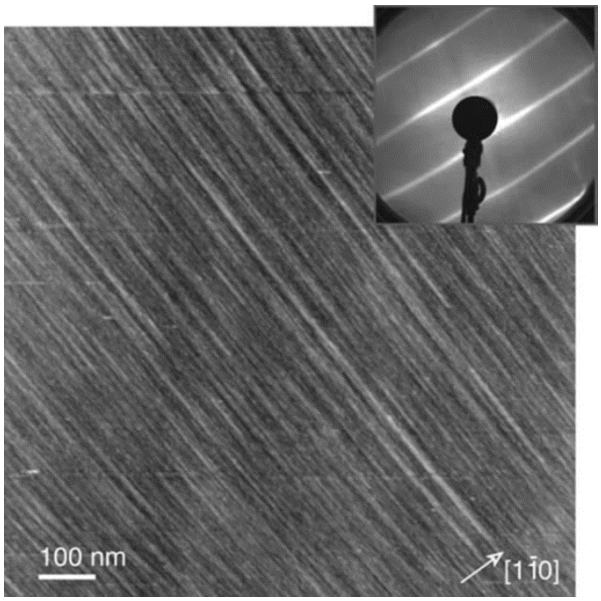

Figure 1.4. STM image of B nanowire on Mo(110) surface and inset showing the LEED pattern of this sample [47].

Later, extensive theoretical investigations on the formation of 2D B sheets for a long period of time initiate its development experimentally. In 2013, Liu et al. [14] predicted using first principles calculations that single layer borophene can form on several metal substrates, such as Ag, Cu, Au; as well as on metal boride substrates, such as MgB_2, TiB_2 by exchanging electrons with the substrates to balance the electron deficiency of B. Moreover, Zhao et al. proposed borophene formation on Cu(111) surface from B cluster in 2013 [48], and in 2015, some preferred borophene structures on Ag, Cu, Ni and Au substrates were suggested by Zhang et al. [10]. These theoretical predictions of forming monolayer B sheets on substrates paves the way for the experimental growth of borophene on various substrates.

In 2015, Xu et al. prepared 2D B sheet on Si wafers by using the CVD technique and diborane was used as B source, and Tai et al. also synthesized ultra-thin B films on Cu foils using the CVD method [49,50], these two experiments could not be able to realize atomically thin B sheet similar to graphene. Mannix et al. first successfully synthesized single layer B sheet on Ag(111) surface in UHV condition by adopting the MBE method in 2015 [51]. They deposited B by electron beam evaporator on clean Ag(111) surface and observed two phases of borophene, named as, homogenous phase and stripped phase, formation on this substrate depending on deposition condition and substrate temperature which were metallic in nature. In Figure 1.5, the experimental condition of borophene preparation (a), STM images of prepared samples (b), and atomic model of stripped phase borophene (c) are shown.

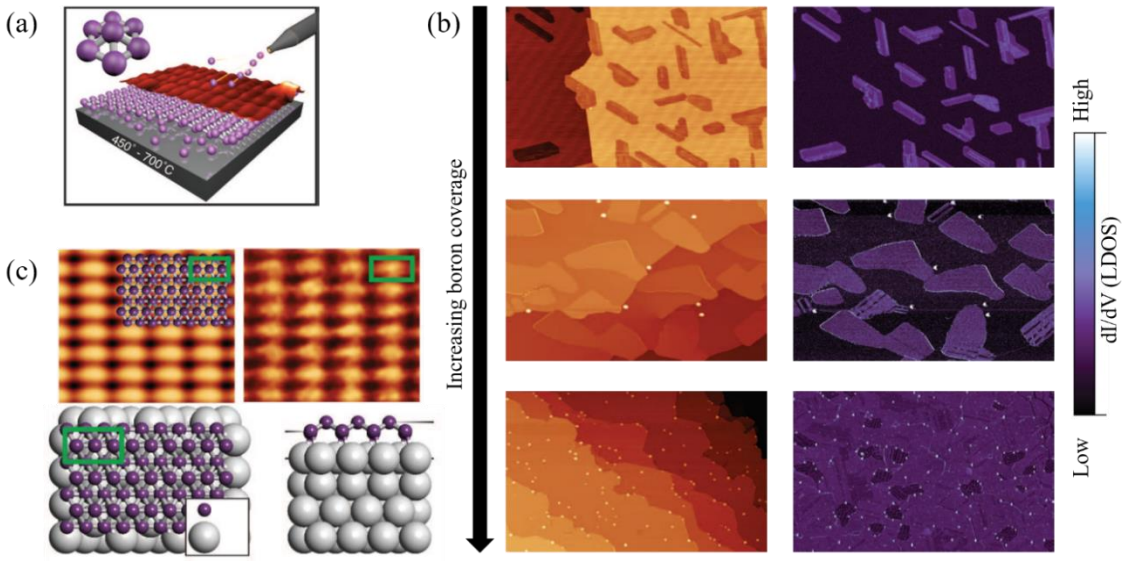

Figure 1.5. (a) Schematic of B growth setup with atomic model, (b) large scale STM topographic (left) and closed-loop dI/dV (right) images of borophene sheet on Ag(111) and (c) simulated (top-left) STM image with superimposed atomic structure and experimental (top-right) STM image with unit cell of borophene over Ag(111) surface, and top (bottom-left) and side (bottom-right) views of atomic model of borophene structure [51].

Another research group at the same time also found growth of borophene on Ag(111), which was extremely substrate temperature dependent [37]. They observed two distinct phases defined as S1 phase and S2 phase. S1 phase developed on Ag(111) surface when the substrate annealed at 570 K, and this phase corresponded to the 6 predicted β_{12} sheet [10] as shown in Figure 1.6(a-d). With the increase of annealing temperature of substrate to 650 K, another phase, S2 phase was formed which corresponded to the proposed χ_3 sheet [13], shown in Figure 1.6(e-h).

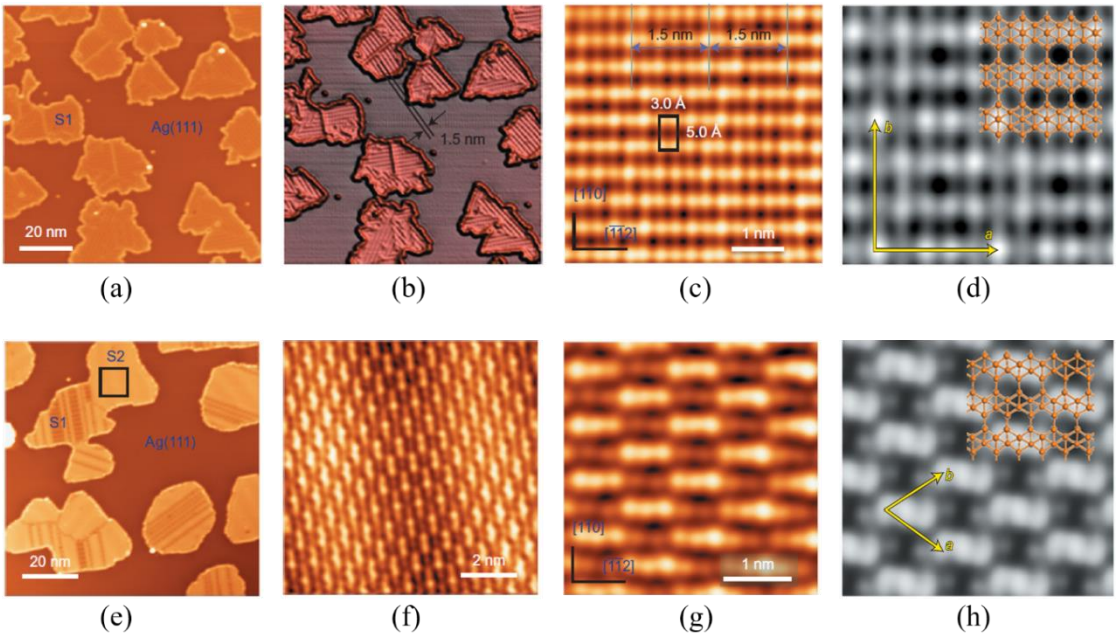

Figure 1.6. (a) STM image of B structure on Ag(111) which is named as S1 phase, (b) 3D version of (a), (c) high resolution STM images of S1 phase, (d) simulated STM image of S1 phase superimposed with β_{12} sheet; (e) STM image of B structure on Ag(111) which is named as S2 phase, (f) STM image of the marked area by black square in (e), (g) high resolution STM image of S2 phase and (h) simulated STM image of S2 phase superimposed with χ_3 sheet [37].

Later, in 2017, four types of B nanoribbons were discerned by Zhong et al. on Ag(110) surface [38]. Despite β_{12} and χ_3 sheet, two new phases β and β_8 were observed from STM analysis which are shown in Figure 1.7. Here, P1 phase resembles as χ_3 sheet, P2 and P3 phase explain by β sheet and P4 denotes as β_8 sheet. They also observed that all phases of borophene consisted of full-filled B chains separated by one row of hexagonal holes.

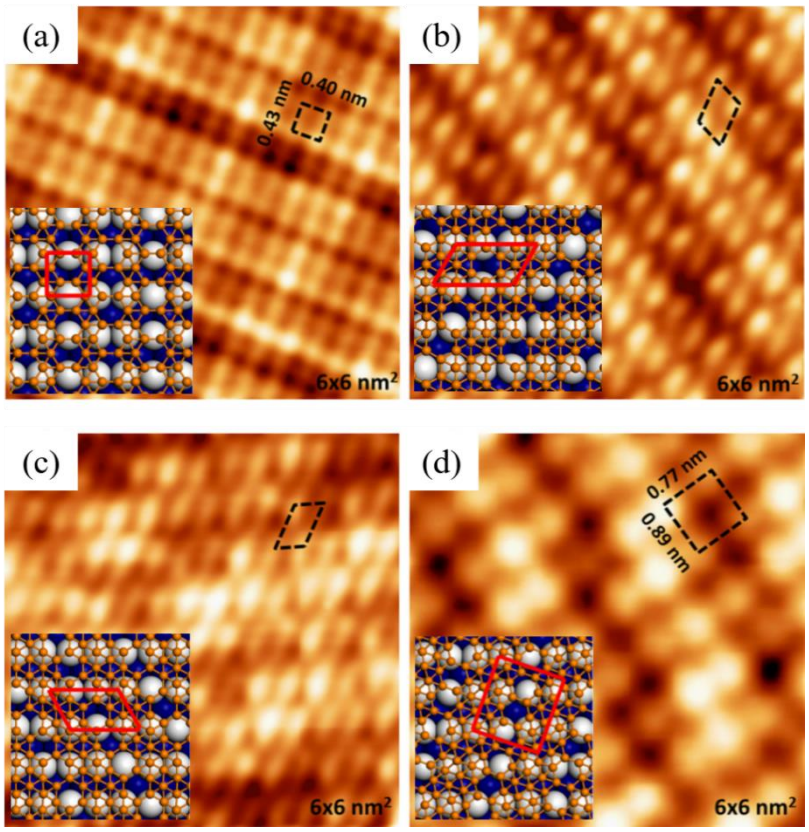

Figure 1.7. High resolution STM images of four types B nanoribbons leveled as (a) P1, (b) P2, (C)P3, and (d) P4 formed on Ag(110) surface with their respective atomic models [38].

Moreover, the effect of the crystalline phase of a substrate on the formation of B sheet was more clearly understood from the experimental realization of borophene chains on Ag(100) surface. Wang et al. [42] noticed three different phases of borophene on Ag(100) in which two phases consisted of a mixed arrangement of (2,3) and (2,2) chains with the ratios of 2:1 (phase A) and 1:2 (phase C) and phase B consisted of four (2,3) parallel chains with various brightness level which are shown in Figure 1.8. Here, in (m,n), m and n denote the number of B atoms in the broadened and smallest regions, respectively.

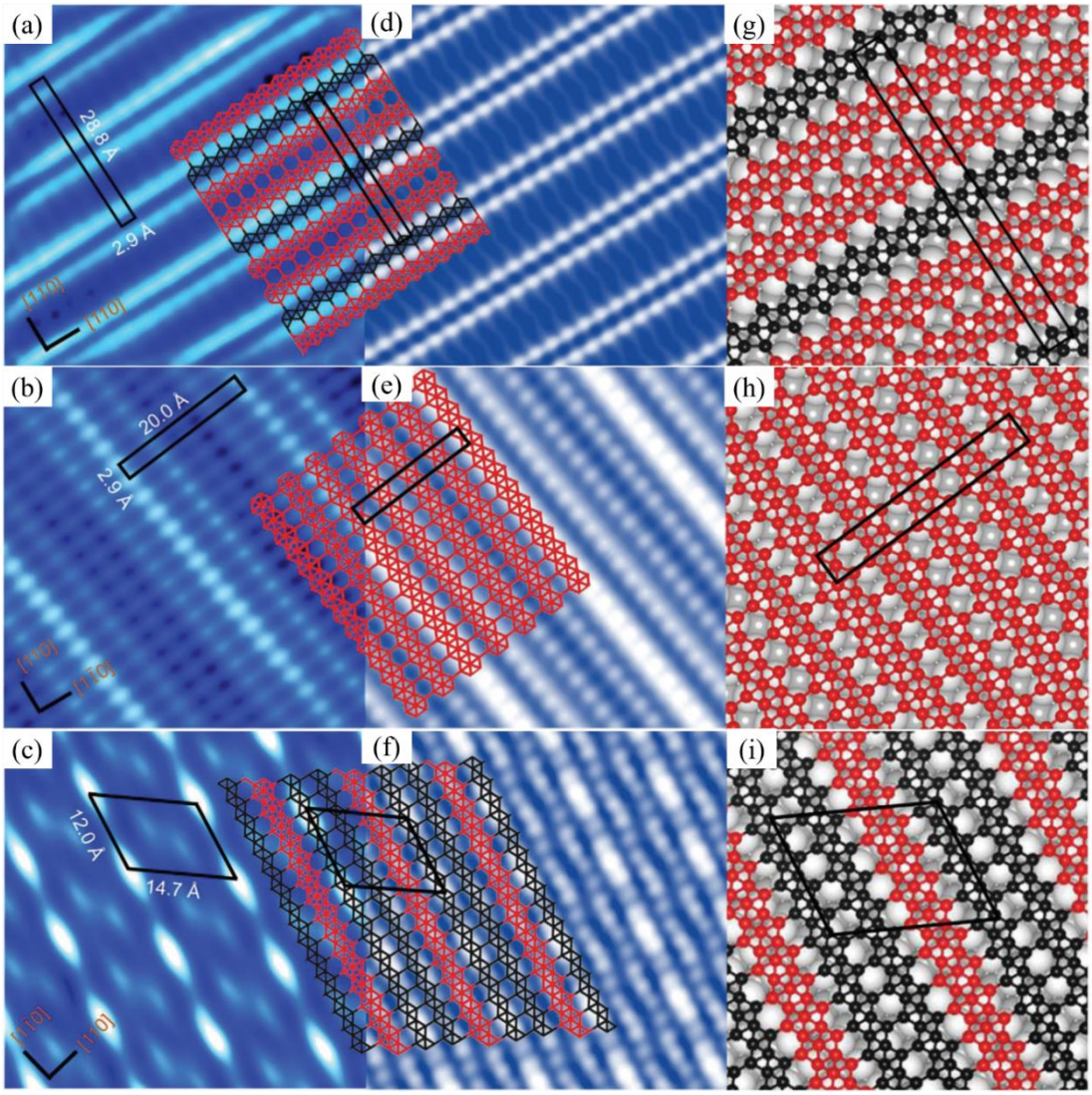

Figure 1.8. Experimental STM images of borophene on Ag(100) named as (a) phase A, (b) phase B and (c) phase C; simulated STM images of (d) phase A, (e) phase B and (f) phase C; and atomic configurations of (g) phase A, (h) phase B and (i) phase C [42].

On the other hand, graphene-like honeycomb borophene was realized by Li et al. [11] on Al(111) surface by STM measurements, as shown in Figure 1.9. They prepared the sample by MBE method in UHV condition and claimed that almost one electron was transferred from the substrate to B atom to stabilize the honeycomb structure which was absent in borophene on Ag(111).

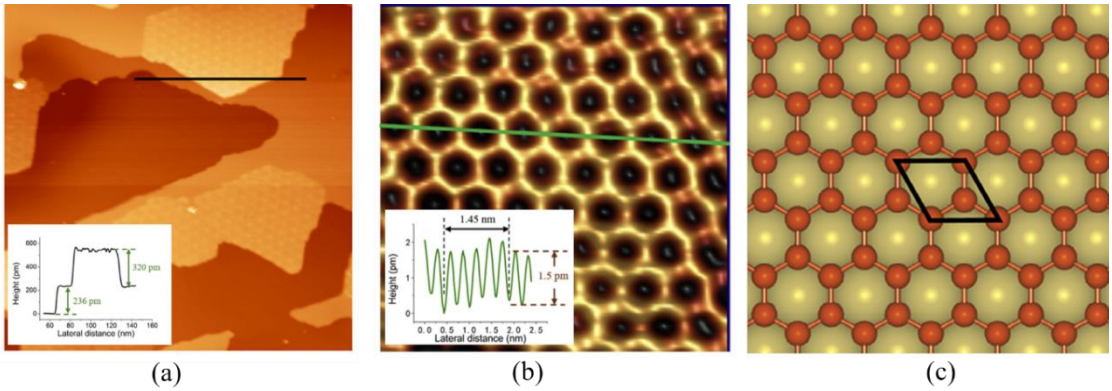

Figure 1.9. (a) Large scale and (b) high resolution STM images of single layer borophene on Al(111) surface, and (c) top view of the structural model of honeycomb borophene on Al(111) surface [11].

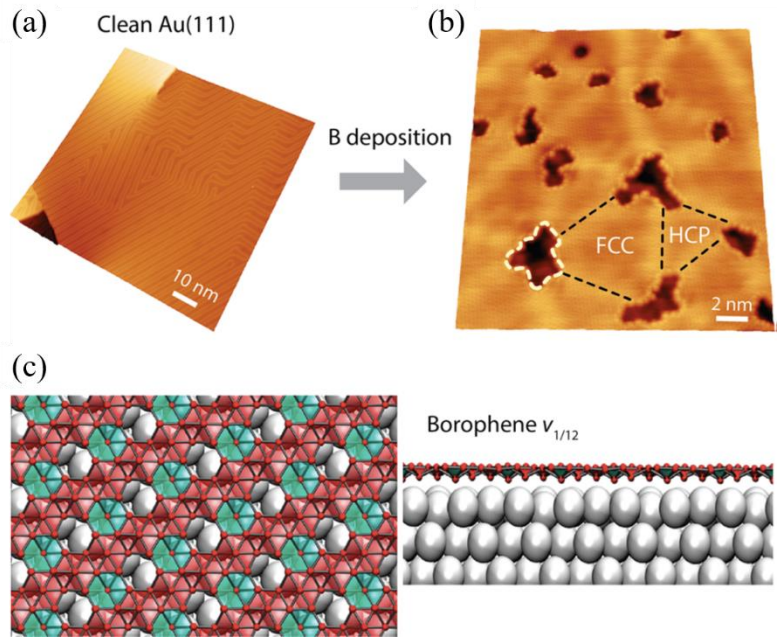

Figure 1.10. STM images of (a) clean Au(111) surface and (b) B covered Au(111) surface, and (c) atomic structural model of borophene, v_{12}, predicted for Au(111) surface [41].

Recently, borophene was synthesized on Au(111) surface in UHV. The growth condition for borophene on Au(111) was different from Ag(111) as B diffused into the Au substrate at elevated temperature and started to segregate to the surface after cooling down. They reported formation of $\nu_{1/12}$ structure of borophene on Au(111) surface [41], which is shown in Figure 1.10. In addition, a novel structure of borophene with a hexagonal hole density of 1/5 was reported by Wu et al. on Cu(111) surface [40]. One atom thick borophene growth was confirmed by atomic force microscopy (AFM), as shown in Figure 1.11(a). From LEED and low energy electron microscopy (LEEM) images (Figure 1.11(b)), it was demonstrated that borophene sheets consisted of large single crystal domains.

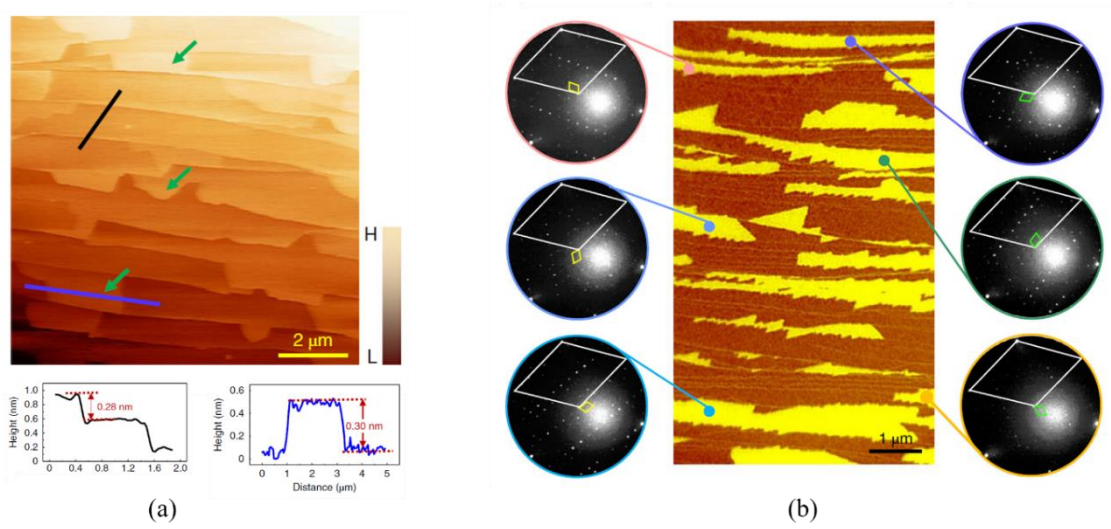

Figure 1.11. (a) Topographic AFM image of B covered Cu(111) surface with 0.1 ML coverage and (b) bright-field LEEM image of borophene on Cu(111) (center), LEED patterns (left and right) of selected area [40].

In 2019, the formation of single phase of borophene was observed by Vinogradov et al. on Ir (111) surface by depositing elemental B on the substrate and consequent annealing [43]. They demonstrated this borophene structure as χ_6 type with hexagonal hole density of 1/6 and B atom density of 0.326 $Å^{-2}$. Borophene on Ir(111) surface changed (1×1) LEED pattern of clean Ir(111) to (6×2) superstructure (Figure 1.12(a-b)) and showed a stripy appearance on STM image, which is shown in Figure 1.12(c).

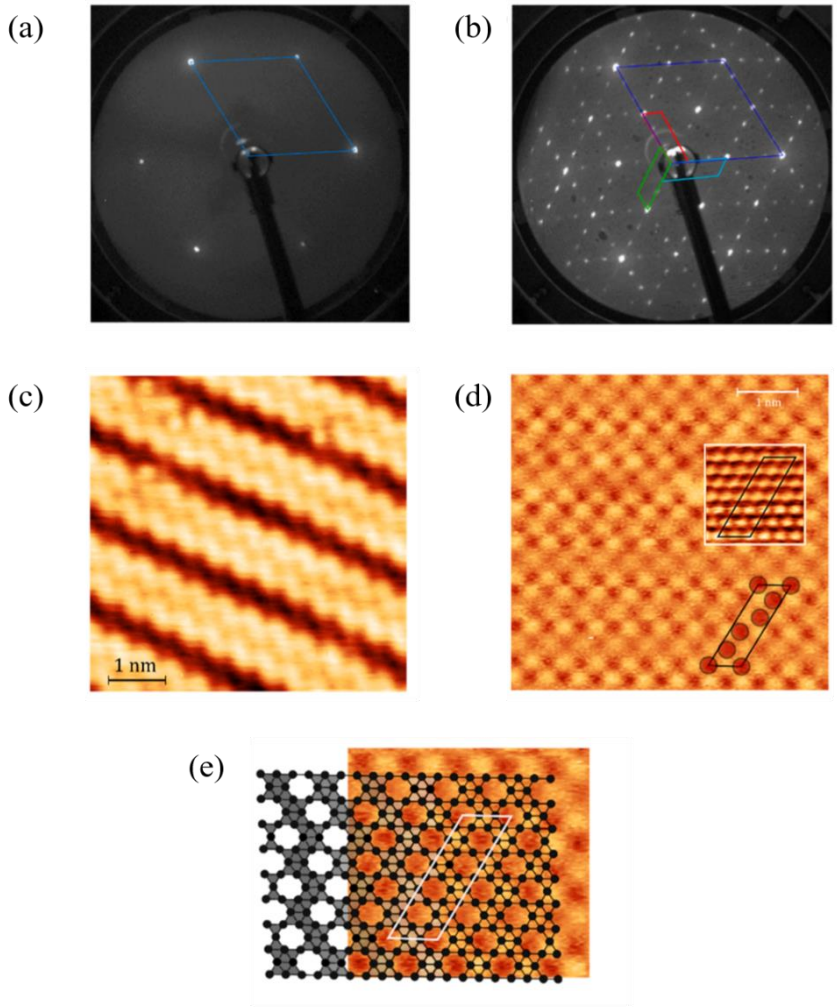

Figure 1.12. LEED patterns of (a) clean Ir(111) surface and (b) borophene on Ir(111), High resolution of STM images of borophene on Ir(111) with different conditions (c) V_{bias} = 1 V, I_t = 500 pA and (d) V_{bias} = 0.9 V, I_t = 400 pA; and (e) proposed atomic model for borophene on Ir(111) [43].

Therefore, after numerous theoretical prediction of borophene growth from 2015 to present date, a lot of efforts have been taken for the successful growth of 2D B sheet on several metal substrates to achieve stable borophene structure which can be a potential candidate to use in photoelectronic devices [52], storing hydrogen [53,54], sensing materials [55,56], rechargeable ion batteries [57–59], nanoelectronics [60], flexible devices [4], catalytic activities [61,62] etc.

1.3 Motivation of research work

Very recently introduced 2D B sheet, borophene, has achieved great research interests due to its extraordinary properties which make this a prominent material for future applications among other 2D materials. These intriguing characteristics are depicted in Figure 1.13. Borophene exhibits anisotropic and polymorphic structure because of the diverse orientation of hexagonal holes in the triangular lattice. It is found that most of the B sheets are metallic having anisotropic behaviors, in contrast to the semi-metallic nature of graphene; therefore, borophene can be referred to the lightest 2D metal [6].

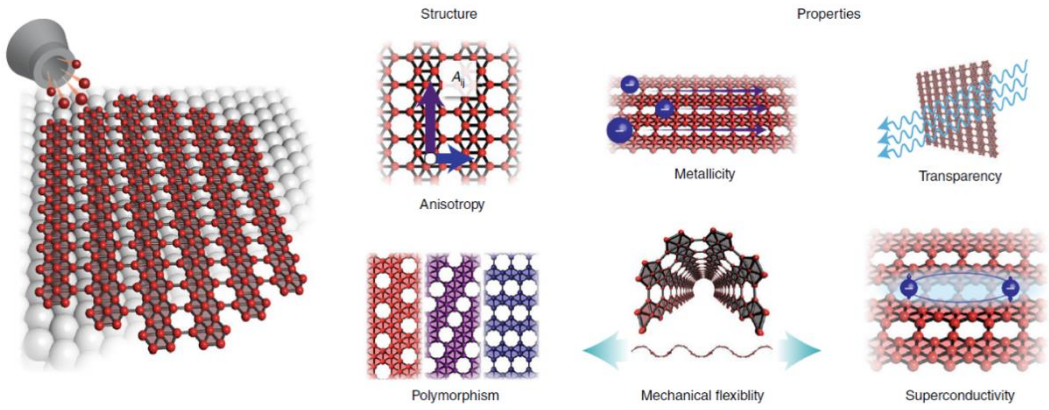

Figure 1.13. Overview of borophene structure with its extraordinary properties [Copied from ref [6]*].*

The metallic behavior of borophene structures is confirmed by scanning tunneling spectroscopy (STS) [37]. Specifically, the extraordinary electronic structures such as Dirac cones are predicted to be existed in χ_3, β_{12} and hydrogenated δ_6 borophene structures according to the theoretical calculations [63]. Experimental analysis by angle resolved photoemission spectroscopy (ARPES) confirms the presence of anisotropic Dirac cones in χ_3 and β_{12} sheets formed on Ag(111) surface [26,29] which are different from isotropic Dirac cone of graphene [64]. Interaction between borophene with the substrate plays a vital role in Dirac cone, i.e, β_{12} phase of borophene on Ag(111) leads to split the Dirac cone due to strong hybridization between β_{12} sheet and Ag; while χ_3 phase has weak interaction with Ag(111) which preserves the Dirac cones which is shown in Figure 1.14.

The Fermi velocity of borophene is comparable with that of graphene, but varies along different direction confirming the anisotropic behavior [29].

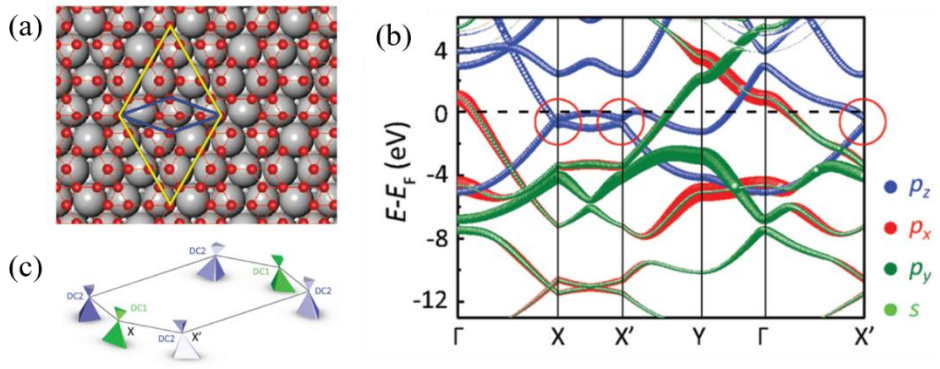

Figure 1.14. Electronic properties of χ_3 borophene on Ag(111) surface. (a) χ_3 borophene structure on Ag(111), (b) band structure of this borophene structure and (c) schematic representation of Dirac cones (black lines indicates the Brillouin zone) [Copied from ref [29]*]*

Moreover, single layer B sheet can be more strong and flexible compared to graphene. It was calculated that Young's modulation at the certain direction of borophene structure is 398 GPa·nm which is slightly higher than graphene (340 GPa·nm) [51]. It is expected that borophene can act as superconductor at relatively higher temperature, ranging from 10-20 K [6]. These extraordinary properties of borophene, along with the theoretically predicted many applications of borophene indicate the great future of borophene.

However, experimental development of this 2D material is still lacking. So far, borophene can only be synthesized experimentally on a few substrates, such as, Ag, Al, Cu, Au, Ir, by the MBE method. As a consequence, many researchers are now focusing on developing borophene on several substrates at a large scale for making this applicable. It is evident that the growth of borophene is strongly dependent on the substrates and their crystalline faces, and other factors during preparation which is described in the previous section.

It was observed that borophene was first successfully synthesized on Ag(111) substrate and this substrate is considered as one of the most promising substrates for the growth of borophene since Ag-B shows phase separation. Interaction between B and substrate is another important fact for B structure, which is very weak for B and Ag as observed from phase diagram of Ag-B which is shown in Figure 1.15.

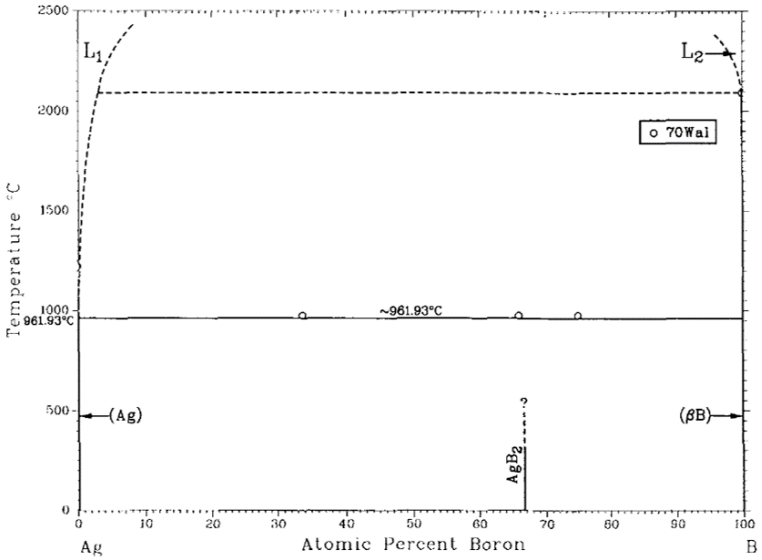

Figure 1.15. Phase diagram of Ag-B [65].

Considering the importance of substrates and their crystalline faces for 2D B sheet growth, adsorption of B on refractory metal surfaces (which are strongly reactive with B), such as, W, Mo etc. has become a major research interest recently. From the phase diagrams of W-B and Mo-B which are shown in Figure 1.16, it is evident that different metal borides are formed based on the B concentration and temperature; which indicates the presence of strong interaction between B and refractory metals.

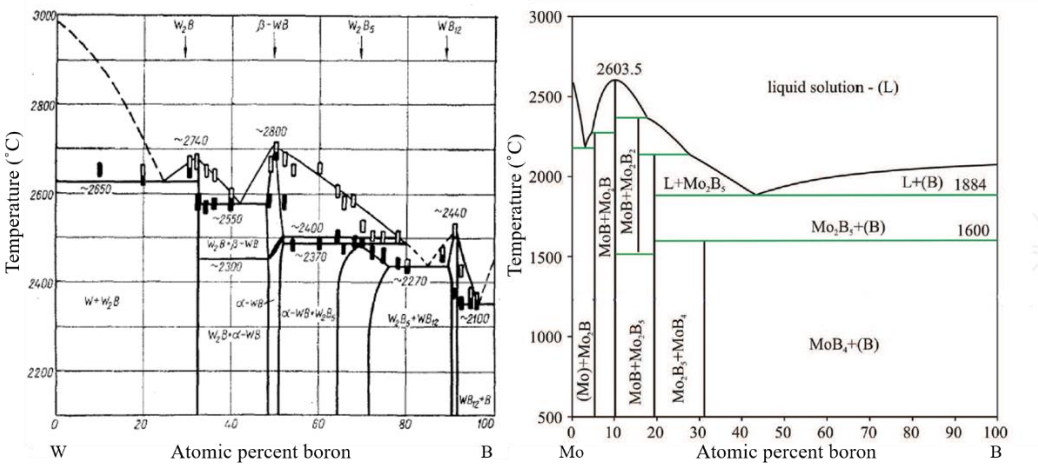

Figure 1.16. Phase diagrams of W-B [66] *and Mo-B* [67].

Moreover, it was reported theoretically earlier that a new phase of borophene named as, π phase, could be formed on W(110) surface [68]. The prediction of borophene formation on W(110) surface inspires the experimental investigation of B structure on refractory metal surfaces. In this thesis, I extensively investigated the B structures on two different crystal faces of BCC refractory metals, W(100) and Mo(110). Since W and Mo substrates are exhibiting similar characteristics due to having almost same properties, such as nearly same lattice constant, high melting point etc.; the crystal faces are important for investigating B structures on these substrates. Therefore, the reasons behind selecting these two surfaces are that W(100) is one of the most extensively studied transition metal surfaces due to its structural phase transition from (1×1) to c(2×2) structure below room temperature [69–72] and Mo(110) surface is considered as one of the most suitable surfaces for the growth of thin films and adsorption because of its stability and flatness [46]. However, another low index surface, (111) of W/Mo is the most unstable surface due to having high surface energy which makes this surface not suitable for forming any superstructure and it was observed earlier that metal adsorption on W(111) or Mo(111) surface induced a faceting transformation [73]. Moreover, low atomic density of (111) surface and small atomic size B atoms lead to diffuse B atoms into the bulk easily which hinders to form any superstructure upon B adsorption. Hence, we choose (100) and (110) crystal faces for investigating B structures and omit (111) surface.

Previously, modification of refractory metal surfaces by adsorbing different elements has been carried out because of their growing demand in the industry due to having high melting point and excellent thermal stability [45,74], and researches were conducted for the adsorbates with high electropositivity, such as alkali metals, or electronegativity, such as O, N, S; compared to transition metals [46,75,76]. For W(100) surface, adsorption of foreign materials including metals, such as Cu, Ag, Au, Na, K, Cs etc. and molecules, such as, H_2, N_2, CO were carried out by LEED to understand the impact of surface reconstruction due to the surface interaction between W and those materials [77–80]; and adsorption of various elements including alkali metals, Cu, Au, Pd, O, H, B, rare earth elements etc. on Mo(110) surface were carried out earlier [46,81-90].

Currently, extensive investigation of the metalloid-metal interface by the deposition B on transition metal surfaces is required to determine the B growth on transition metal substrates. In previous works, Tucker only investigated the interaction of B with the different crystal surfaces of W substrate by LEED [44]. The interactions between B and Mo was observed by Magkoev et al. and Fryberger et al. [45,46] using XPS and AES. Though the interaction of B and Mo with the change of temperature was analyzed earlier, the B arrangement over the Mo(110) surface at different temperatures has remained unspecified. In addition, the structure formed on transition metal surfaces after adsorbing B atoms as well as the surface relaxation of the underlying substrate have not been reported in earlier works.

In this thesis, firstly, the reconstruction of W(100) surface due to the deposition of B atoms was investigated extensively by quantitative LEED analysis for getting the information about B atoms arrangement on the W(100) surface with the bonding interaction between B and W atoms as well as surface relaxation of W atoms for the first few layers beneath B atoms. Besides, XPS analysis was conducted to understand the chemical interaction between B and W. To confirm the obtained best structural model from LEED analysis, STM measurements were carried out as well. In the following work, the growth of B on Mo(110) surface at various temperatures has been reported by STM and LEED to determine the structural condition of B atoms over Mo(110) surface. Thereby, the analyses of structural and chemical properties by LEED, STM and XPS

come up with the understanding of B structure formed on two different transition metal surfaces with their interactivities with each other which will provide significant information in the field of surface science.

References

[1] R. Tran, Z. Xu, B. Radhakrishnan, D. Winston, W. Sun, K.A. Persson, S.P. Ong, Surface energies of elemental crystals, Sci. Data. 3 (2016) 160080. https://doi.org/10.1038/sdata.2016.80.

[2] K. Wandelt, Introduction: An intuitive approach to surface and interface science, 2013. Surf. Interface Sci. (2013) 1-12. https://doi.org/10.1002/9783527680535.ch1.

[3] D.G. Castner, Surface analysis: From single crystals to biomaterials, Surf. Interface Anal. 50 (2018) 981–990. https://doi.org/10.1002/sia.6422.

[4] Z. Zhang, Y. Yang, E.S. Penev, B.I. Yakobson, Elasticity, flexibility, and ideal strength of borophenes, Adv. Funct. Mater. 27 (2017) 1605059. https://doi.org/10.1002/adfm.201605059.

[5] X. Sun, X. Liu, J. Yin, J. Yu, Y. Li, Y. Hang, X. Zhou, M. Yu, J. Li, G. Tai, W. Guo, Two-dimensional boron crystals: structural stability, tunable properties, fabrications and applications, Adv. Funct. Mater. 27 (2017) 1603300. https://doi.org/10.1002/adfm.201603300.

[6] A.J. Mannix, Z. Zhang, N.P. Guisinger, B.I. Yakobson, Borophene as a prototype for synthetic 2D materials development, Nat. Nanotechnol. 13 (2018) 444–450. https://doi.org/10.1038/s41565-018-0157-4.

[7] S. Xie, Y. Wang, X. Li, Flat Boron: A new cousin of graphene, Adv. Mater. 31 (2019) 1900392. https://doi.org/10.1002/adma.201900392.

[8] H.-J. Zhai, B. Kiran, J. Li, L.-S. Wang, Hydrocarbon analogues of boron clusters — planarity, aromaticity and antiaromaticity, Nat. Mater. 2 (2003) 827–833. https://doi.org/10.1038/nmat1012.

[9] Z.A. Piazza, H. Hu, W. Li, Y. Zhao, J. Li, L. Wang, Planar hexagonal B_{36} as a potential basis for extended single-atom layer boron sheets, Nat. Commun. (2014). https://doi.org/10.1038/ncomms4113.

[10] Z. Zhang, Y. Yang, G. Gao, B.I. Yakobson, Two-dimensional boron monolayers mediated by metal substrates, Angew. Commun. 54 (2015) 13022–13026. https://doi.org/10.1002/anie.201505425.

[11] W. Li, L. Kong, C. Chen, J. Gou, S. Sheng, W. Zhang, H. Li, L. Chen, P. Cheng, K. Wu, Experimental realization of honeycomb borophene, Sci. Bull. 63 (2018)

282–286. https://doi.org/10.1016/j.scib.2018.02.006.

[12] H. Tang, S. Ismail-Beigi, Novel precursors for boron nanotubes: The competition of two-center and three-center bonding in boron sheets, Phys. Rev. Lett. 99 (2007) 115501. https://doi.org/10.1103/PhysRevLett.99.115501.

[13] X. Wu, J. Dai, Y. Zhao, Z. Zhuo, J. Yang, X.C. Zeng, Two-dimensional boron monolayer sheets, ACS Nano. 6 (2012) 7443–7453. https://doi.org/10.1021/nn302696v.

[14] Y. Liu, E.S. Penev, B.I. Yakobson, Probing the synthesis of two-dimensional boron by first-principles computations, Angew. Chemie Int. Ed. 52 (2013) 3156–3159. https://doi.org/10.1002/anie.201207972.

[15] I.V.G. and A.A.F. K. S. Novoselov, A. K. Geim, S. V. Morozov, D. Jiang, Y. Zhang, S. V. Dubonos, Electric field effect in atomically thin carbon films, Science. 306 (2016) 666–669.

[16] M. Akhtar, G. Anderson, R. Zhao, A. Alruqi, J.E. Mroczkowska, G. Sumanasekera, J.B. Jasinski, Recent advances in synthesis, properties, and applications of phosphorene, 2D Mater. Appl. 1 (2017) 5. https://doi.org/10.1038/s41699-017-0007-5.

[17] J. Ji, X. Song, J. Liu, Z. Yan, C. Huo, S. Zhang, M. Su, L. Liao, W. Wang, Z. Ni, Y. Hao, H. Zeng, Two-dimensional antimonene single crystals grown by van der Waals epitaxy, Nat. Commun. 7 (2016) 1–9. https://doi.org/10.1038/ncomms13352.

[18] J. Shah, W. Wang, H.M. Sohail, R.I.G. Uhrberg, Experimental evidence of monolayer arsenene: An exotic 2D semiconducting material, 2D Mater. 7 (2020). https://doi.org/10.1088/2053-1583/ab64fb.

[19] M. Maniraj, B. Stadtmüller, D. Jungkenn, M. Düvel, S. Emmerich, W. Shi, J. Stöckl, L. Lyu, J. Kollamana, Z. Wei, A. Jurenkow, S. Jakobs, B. Yan, S. Steil, M. Cinchetti, S. Mathias, M. Aeschlimann, A case study for the formation of stanene on a metal surface, Commun. Phys. 2 (2019) 1–9. https://doi.org/10.1038/s42005-019-0111-2.

[20] A. Acun, L. Zhang, P. Bampoulis, M. Farmanbar, A. Van Houselt, A.N. Rudenko, M. Lingenfelder, G. Brocks, B. Poelsema, M.I. Katsnelson, H.J.W. Zandvliet, Germanene: The germanium analogue of graphene, J. Phys. Condens. Matter. 27 (2015) 443002. https://doi.org/10.1088/0953-8984/27/44/443002.

[21] P. Vogt, P. Capiod, M. Berthe, A. Resta, P. De Padova, T. Bruhn, G. Le Lay, B.

Grandidier, Synthesis and electrical conductivity of multilayer silicene, Appl. Phys. Lett. 104 (2014) 021602. https://doi.org/10.1063/1.4861857.

[22] Z. Zhang, A.J. Mannix, Z. Hu, B. Kiraly, N.P. Guisinger, M.C. Hersam, B.I. Yakobson, Substrate-induced nanoscale undulations of borophene on silver, Nano Lett. 16 (2016) 6622–6627. https://doi.org/10.1021/acs.nanolett.6b03349.

[23] Z. Luo, X. Fan, Y. An, First-principles study on the stability and stm image of borophene, Nanoscale Res. Lett. 12 (2017). https://doi.org/10.1186/s11671-017-2282-7.

[24] B. Feng, J. Zhang, R.Y. Liu, T. Iimori, C. Lian, H. Li, L. Chen, K. Wu, S. Meng, F. Komori, I. Matsuda, Direct evidence of metallic bands in a monolayer boron sheet, Phys. Rev. B. 94 (2016) 2–6. https://doi.org/10.1103/PhysRevB.94.041408.

[25] L. Adamska, S. Sadasivam, J.J. Foley, P. Darancet, S. Sharifzadeh, First-principles investigation of borophene as a monolayer transparent conductor, J. Phys. Chem. C. 122 (2018) 4037–4045. https://doi.org/10.1021/acs.jpcc.7b10197.

[26] B. Feng, O. Sugino, R.Y. Liu, J. Zhang, R. Yukawa, M. Kawamura, T. Iimori, H. Kim, Y. Hasegawa, H. Li, L. Chen, K. Wu, H. Kumigashira, F. Komori, T.C. Chiang, S. Meng, I. Matsuda, Dirac fermions in borophene, Phys. Rev. Lett. 118 (2017) 1–6. https://doi.org/10.1103/PhysRevLett.118.096401.

[27] X.F. Zhou, X. Dong, A.R. Oganov, Q. Zhu, Y. Tian, H.T. Wang, Semimetallic two-dimensional boron allotrope with massless Dirac fermions, Phys. Rev. Lett. 112 (2014) 1–5. https://doi.org/10.1103/PhysRevLett.112.085502.

[28] S. Gupta, A. Kutana, B.I. Yakobson, Dirac cones and nodal line in borophene, J. Phys. Chem. Lett. 9 (2018) 2757–2762. https://doi.org/10.1021/acs.jpclett.8b00640.

[29] B. Feng, J. Zhang, S. Ito, M. Arita, C. Cheng, L. Chen, K. Wu, F. Komori, O. Sugino, K. Miyamoto, T. Okuda, S. Meng, I. Matsuda, Discovery of 2D anisotropic Dirac cones, Adv. Mater. 30 (2018) 1704025. https://doi.org/10.1002/adma.201704025.

[30] E.S. Penev, A. Kutana, B.I. Yakobson, Can two-dimensional boron superconduct ?, Nano Lett. 16 (2016) 2522–2526.https://doi.org/10.1021/acs.nanolett.6b00070.

[31] M. Gao, Q.Z. Li, X.W. Yan, J. Wang, Prediction of phonon-mediated superconductivity in borophene, Phys. Rev. B. 95 (2017) 1–9.

https://doi.org/10.1103/PhysRevB.95.024505.

[32] X.F. Zhou, A.R. Oganov, Z. Wang, I.A. Popov, A.I. Boldyrev, H.T. Wang, Two-dimensional magnetic boron, Phys. Rev. B. 93 (2016) 1–6. https://doi.org/10.1103/PhysRevB.93.085406.

[33] W.-L. Li, X. Chen, T. Jian, T. Chen, J. Li, L.-S. Wang, From planar boron clusters to borophenes and metalloborophenes, Nat. Rev. Chem. 1 (2017) 0071. https://doi.org/10.1038/s41570-017-0071.

[34] L. Liu, Z. Zhang, X. Liu, X. Xuan, B.I. Yakobson, M.C. Hersam, W. Guo, Borophene concentric superlattices via self-assembly of twin boundaries, Nano Lett. 20 (2020) 1315–1321. https://doi.org/10.1021/acs.nanolett.9b04798.

[35] C.Ö. Zdoğan, S. Mukhopadhyay, W. Hayami, Z.B. Güvenc, R. Pandey, S. Boustani, The unusually stable B_{100} Fullerene, structural transitions in boron nanostructures, and a comparative study of α- and γ-boron and sheets, J. Phys. Chem. C. 114 (2010) 4362–4375. https://doi.org/10.1021/jp911641u.

[36] E.S. Penev, S. Bhowmick, A. Sadrzadeh, B.I. Yakobson, Polymorphism of two-dimensional boron, Nano Lett. 12 (2012) 2441–2445. https://doi.org/10.1021/nl3004754.

[37] B. Feng, J. Zhang, Q. Zhong, W. Li, S. Li, H. Li, P. Cheng, S. Meng, L. Chen, K. Wu, Experimental realization of two-dimensional boron sheets, Nat. Chem. 8 (2016) 563–568. https://doi.org/10.1038/nchem.2491.

[38] Q. Zhong, L. Kong, J. Gou, W. Li, S. Sheng, S. Yang, P. Cheng, H. Li, K. Wu, L. Chen, Synthesis of borophene nanoribbons on Ag(110) surface, Phys. Rev. Mater. 1 (2017) 021001. https://doi.org/10.1103/PhysRevMaterials.1.021001.

[39] R. Wu, A. Gozar, I. Božović, Large-area borophene sheets on sacrificial Cu(111) films promoted by recrystallization from subsurface boron, Quantum Mater. 4 (2019) 40. https://doi.org/10.1038/s41535-019-0181-0.

[40] R. Wu, I.K. Drozdov, S. Eltinge, P. Zahl, S. Ismail-Beigi, I. Božović, A. Gozar, Large-area single-crystal sheets of borophene on Cu(111) surfaces, Nat. Nanotechnol. 14 (2019) 44–49. https://doi.org/10.1038/s41565-018-0317-6.

[41] B. Kiraly, X. Liu, L. Wang, Z. Zhang, A.J. Mannix, B.L. Fisher, B.I. Yakobson, M.C. Hersam, N.P. Guisinger, Borophene synthesis on Au(111), ACS Nano. 13 (2019) 3816–3822. https://doi.org/10.1021/acsnano.8b09339.

[42] Y. Wang, L. Kong, C. Chen, P. Cheng, B. Feng, K. Wu, L. Chen, Realization of

regular-mixed quasi-1D borophene chains with long-range order, Adv. Mater. 32 (2020) 1–6. https://doi.org/10.1002/adma.202005128.

[43] N.A. Vinogradov, A. Lyalin, T. Taketsugu, A.S. Vinogradov, A. Preobrajenski, Single-phase borophene on Ir(111): Formation, structure, and decoupling from the support, ACS Nano. 13 (2019) 14511–14518. https://doi.org/10.1021/acsnano.9b08296.

[44] W. Tucker, Interaction of boron with tungsten single crystal substrates, Surf. Sci. 5 (1966) 179–186. https://doi.org/10.1016/0039-6028(66)90079-3.

[45] T.B. Fryberger, J.L. Grant, P.C. Stair, Adsorption of boron on molybdenum(100) and its effect on chemisorption of carbon monoxide, ethene, propene, and 3,3,3-trifluoropropene, Langmuir. 3 (1987) 1015–1025. https://doi.org/10.1021/la00078a024.

[46] T.T. Magkoev, A.M. Turiev, N.I. Tsidaeva, D.G. Panteleev, G.G. Vladimirov, G.A. Rump, Adsorption of boron on a Mo(110) surface, J. Phys. Condens. Matter. 20 (2008) 485007. https://doi.org/10.1088/0953-8984/20/48/485007.

[47] M.P. Allan, S. Berner, M. Corso, T. Greber, J. Osterwalder, Tunable self-assembly of one-dimensional nanostructures with orthogonal directions, Nanoscale Res. Lett. 2 (2007) 94–99. https://doi.org/10.1007/s11671-006-9036-2.

[48] H. Liu, J. Gao, J. Zhao, From boron cluster to two-dimensional boron sheet on Cu(111) surface: Growth mechanism and hole formation, Sci. Rep. 3 (2013) 27–30. https://doi.org/10.1038/srep03238.

[49] J. Xu, Y. Chang, L. Gan, Y. Ma, T. Zhai, Ultrathin single-crystalline boron nanosheets for enhanced electro-optical performances, Adv. Sci. 2 (2015) 1–11. https://doi.org/10.1002/advs.201500023.

[50] G. Tai, T. Hu, Y. Zhou, X. Wang, J. Kong, T. Zeng, Y. You, Q. Wang, Synthesis of atomically thin boron films on copper foils, Angew. Chemie - Int. Ed. 54 (2015) 15473–15477. https://doi.org/10.1002/anie.201509285.

[51] A.J. Mannix, X.F. Zhou, B. Kiraly, J.D. Wood, D. Alducin, B.D. Myers, X. Liu, B.L. Fisher, U. Santiago, J.R. Guest, M.J. Yacaman, A. Ponce, A.R. Oganov, M.C. Hersam, N.P. Guisinger, Synthesis of borophenes: Anisotropic, two-dimensional boron polymorphs, Science. 350 (2015) 1513–1516. https://doi.org/10.1126/Xscience.aad1080.

[52] Y. An, Y. Hou, H. Wang, J. Li, R. Wu, T. Wang, H. Da, J. Jiao, Unveiling the electric-current-limiting and photodetection effect in two-dimensional

hydrogenated borophene, Phys. Rev. Appl. 11 (2019). https://doi.org/10.1103/PhysRevApplied.11.064031.

[53] C.S. Liu, X. Wang, X.J. Ye, X. Yan, Z. Zeng, Curvature and ionization-induced reversible hydrogen storage in metalized hexagonal B36, J. Chem. Phys. 141 (2014). https://doi.org/10.1063/1.4902062.

[54] A. Lebon, R.H. Aguilera-del-Toro, L.J. Gallego, A. Vega, Li-decorated Pmmn8 phase of borophene for hydrogen storage. A van der Waals corrected density-functional theory study, Int. J. Hydrogen Energy. 44 (2019) 1021–1033. https://doi.org/10.1016/j.ijhydene.2018.10.241.

[55] V. Shukla, J. Wärnå, N.K. Jena, A. Grigoriev, R. Ahuja, Toward the realization of 2D borophene based gas sensor, J. Phys. Chem. C. 121 (2017) 26869–26876. https://doi.org/10.1021/acs.jpcc.7b09552.

[56] C. Xiao, K. Ma, G. Cai, X. Zhang, E. Vessally, Borophene as an electronic sensor for metronidazole drug: A computational study, J. Mol. Graph. Model. 96 (2020) 107539. https://doi.org/10.1016/j.jmgm.2020.107539.

[57] O. Folorunso, Y. Hamam, R. Sadiku, S.S. Ray, G.J. Adekoya, Theoretical analysis of borophene for lithium ion electrode, Mater. Today Proc. 38 (2019) 485–489. https://doi.org/10.1016/j.matpr.2020.02.285.

[58] L. Zhang, P. Liang, H.B. Shu, X.L. Man, F. Li, J. Huang, Q.M. Dong, D.L. Chao, Borophene as efficient sulfur hosts for lithium-sulfur batteries: suppressing shuttle effect and improving conductivity, J. Phys. Chem. C. 121 (2017) 15549–15555. https://doi.org/10.1021/acs.jpcc.7b03741.

[59] H.R. Jiang, W. Shyy, M. Liu, Y.X. Ren, T.S. Zhao, Borophene and defective borophene as potential anchoring materials for lithium-sulfur batteries: A first-principles study, J. Mater. Chem. A. 6 (2018) 2107–2114. https://doi.org/10.1039/c7ta09244j.

[60] A. Rubab, N. Baig, M. Sher, M. Sohail, Advances in ultrathin borophene materials, Chem. Eng. J. 401 (2020) 126109. https://doi.org/10.1016/j.cej.2020.126109.

[61] L. Shi, C. Ling, Y. Ouyang, J. Wang, High intrinsic catalytic activity of two-dimensional boron monolayers for the hydrogen evolution reaction, Nanoscale. 9 (2017) 533–537. https://doi.org/10.1039/C6NR06621F.

[62] S.H. Mir, S. Chakraborty, P.C. Jha, J. Wärnå, H. Soni, P.K. Jha, R. Ahuja, Two-dimensional boron: Lightest catalyst for hydrogen and oxygen evolution reaction,

Appl. Phys. Lett. 109 (2016). https://doi.org/10.1063/1.4960102.

[63] D. Li, J. Gao, P. Cheng, J. He, Y. Yin, Y. Hu, L. Chen, Y. Cheng, J. Zhao, 2D Boron sheets: structure, growth, and electronic and thermal transport properties, Adv. Funct. Mater. 30 (2020) 1–32. https://doi.org/10.1002/adfm.201904349.

[64] X.F. Zhou, H.T. Wang, Low-dimensional boron: searching for Dirac materials, Adv. Phys. X. 1 (2016) 412–424. https://doi.org/10.1080/23746149.2016.1209432.

[65] Okamoto, H. Ag-B (silver-boron). J. Phase Equilibria. 13 (1992) 211-212. https://doi.org/10.1007/BF02667492.

[66] K.I. Portnoi, V.M. Romashov, Y. V. Levinskii, I. V. Romanovich, Phase diagram of the system tungsten-boron, Sov. Powder Metall. Met. Ceram. 6 (1967) 398–402. https://doi.org/10.1007/BF00775398.

[67] J. Karwan-Baczewska, B. Onderka, Sintering prealloyed powders Fe-Ni-Cu-Mo modified by boron base on thermodynamic investigations, Powder Metall. - Fundam. Case Stud. (2017) 53–71. https://doi.org/10.5772/66875

[68] Z.H. Cui, E. Jimenez-Izal, A.N. Alexandrova, Prediction of two-dimensional phase of boron with anisotropic electric conductivity, J. Phys. Chem. Lett. 8 (2017) 1224–1228. https://doi.org/10.1021/acs.jpclett.7b00275.

[69] M.K. Debe, D.A. King, The clean thermally induced W {001} (1 × 1) → (√2 × √2) R 45° surface structure transition and its crystallography, Surf. Sci. 81 (1979) 193–237. https://doi.org/10.1016/0039-6028(79)90513-2.

[70] G. Schmidt, H. Zagel, H. Landskron, K. Heinz, K. Müller, J.B. Pendry, The clean and H-induced reconstruction of W(100) studied by LEED at slanting primary bean incidence, Surf. Sci. 271 (1992) 416–426. https://doi.org/10.1016/0039-6028(92)90905-L.

[71] R.A. Barker and P.J. Estrup, Structural models of the reconstructed W{001} surface, Solid State Commun. 32 (1978) 147–156. https://doi.org/10.1016/0038-1098(78)90079-0.

[72] T.E. Felter, R.A. Barker, P.J. Estrup, Phase transition on Mo(100) and W(100) surfaces, Phys. Rev. Lett. 38 (1977) 1138–1142. https://doi.org/10.1103/PhysRevLett.38.1138.

[73] J. Che, C. Chan, W.E. Jian, T. Leung, Surface atomic structures, surface energies, and equilibrium crystal shape of molybdenum, Phys. Rev. B - Condens. Matter

Mater. Phys. 57 (1998) 1875–1880. https://doi.org/10.1103/PhysRevB.57.1875.

[74] D.R. Glasson, J.A. Jones, Formation and reactivity of borides, carbides and silicides. I. Review and introduction, J. Appl. Chem. 19 (2007) 125–137. https://doi.org/10.1002/jctb.5010190501.

[75] J. Cousty, R. Riwan, P. Soukiassian, Adsorption of alkali metals on W(100): an EELS study, J. Phys. Paris. 46 (1985) 1693–1698. https://doi.org/10.1051/jphys:0198500460100169300.

[76] S. Murphy, G. Manai, I. V Shvets, Oxygen-induced p(3 × 1) reconstruction of the W(100) surface, Surf. Sci. 579 (2005) 65–72. https://doi.org/10.1016/j.susc.2005.01.048.

[77] P. Hu, A. Wander, L.M. de la Garza, M.P. Bessent, D.A. King, An adsorbate-stabilised vacancy structure for Cu on W{100}: A surface alloy, Surf. Sci. 286 (1993) 542–546. https://doi.org/10.1016/0039-6028(93)90546-V.

[78] G.A. Attard, D.A. King, Temperature-induced surface structural transformations: silver and gold on W{100}, Surf. Sci. 222 (1989) 360–370. https://doi.org/10.1016/0039-6028(89)90366-X.

[79] K. Kankaala, T. Ala-Nissila, S.C. Ying, Theory of adsorbate-induced surface reconstruction on W(100), Phys. Rev. B. 47 (1993) 2333–2343. https://doi.org/10.1103/PhysRevB.47.2333.

[80] K. Yonehara, L.D. Schmidt, A LEED study of structures ptoduced by H_2 on (100)W, Surf. Sci. 25 (1971) 238–260. https://doi.org/10.1016/0039-6028(71)90245-7.

[81] J. Kröger, D. Bruchmann, S. Lehwald, H. Ibach, Adsorption of lithium on Mo(110): An EELS study of the adsorbate vibrations and substrate phonons, Surf. Sci. 449 (2000) 227–235. https://doi.org/10.1016/S0039-6028(00)00058-3.

[82] S. Thomas, T.W. Haas, LEED/Auger spectroscopy study of the adsorption of alkali metals on Mo(110), J. Vac. Sci. Technol. 9 (1972) 840–843. https://doi.org/10.1116/1.1317798.

[83] M. Paunov, E. Bauer, An adsorption-desorption study of Cu on Mo(110), Appl. Phys. A Solids Surfaces. 44 (1987) 201–208. https://doi.org/10.1007/BF00626424.

[84] A. Krupski, Scanning tunnelling microscopy study of Au growth on Mo(110), Surf. Sci. 605 (2011) 424–428. https://doi.org/10.1016/j.susc.2010.11.012.

[85] A. Krupski, Pb on Mo(110) studied by scanning tunneling microscopy, Phys. Rev. B - Condens. Matter Mater. Phys. 80 (2009). https://doi.org/10.1103/PhysRevB.80.035424.

[86] K. Kośmider, A. Krupski, P. Jelínek, L. Jurczyszyn, Atomic and electronic properties of the Pb/Mo(110) adsorption system, Phys. Rev. B - Condens. Matter Mater. Phys. 80 (2009). https://doi.org/10.1103/PhysRevB.80.115424.

[87] M.L. Colaianni, J.G. Chen, W.H. Weinberg, J.T. Yates, Oxygen on Mo(110): low-temperature adsorption and high-temperature oxidation, Surf. Sci. 279 (1992) 211–222. https://doi.org/10.1016/0039-6028(92)90547-J.

[88] M.L. Ernst-Vidalis, E. Bauer, Hydrogen on Mo(110): Adsorption and electron stimulated H+ desorption, Surf. Sci. 215 (1989) 378–384. https://doi.org/10.1016/0039-6028(89)90267-7.

[89] S.A. Shakirova, V.A. Pleshkov, G.A. Rump, Adsorption of rare-earth metals (Tb,Dy,Er) on a Mo(110) surface, Surf. Sci. 279 (1992) 113–118. https://doi.org/10.1016/0039-6028(92)90747-T.

[90] M. Wiejak, M. Jankowski, I. Yakovkin, J. Kołaczkiewicz, Adsorption of Nd on the Mo(110) surface, Appl. Surf. Sci. 256 (2010) 4834–4838. https://doi.org/10.1016/j.apsusc.2010.01.112.

CHAPTER 2: FUNDAMENTALS AND METHODOLOGIES

2.1 Basics of surface crystallography

2.1.1 Surface physics

The study of solid surface and its interface starts from crystal structure in which atoms are oriented infinitely in a periodic pattern in three dimensions (3D). The most fundamental part for bulk 3D crystal is known as lattice which is the geometrical pattern of a crystal. Lattice is also defined by a set of three fundamental translation vectors, a, b, and c as;

$$\boldsymbol{r} = \boldsymbol{r}' + n_1\,\boldsymbol{a} + n_2\,\boldsymbol{b} + n_3\,\boldsymbol{c}$$

where, n_1, n_2, and n_3 are integers. The crystal can be visualized as the same when it is observed from r and r'. An atom or a group of atoms positioning to each lattice point is known as basis. Therefore, the repeated orientation of basis to each lattice point forms a crystal structure which is depicted in Figure 2.1.

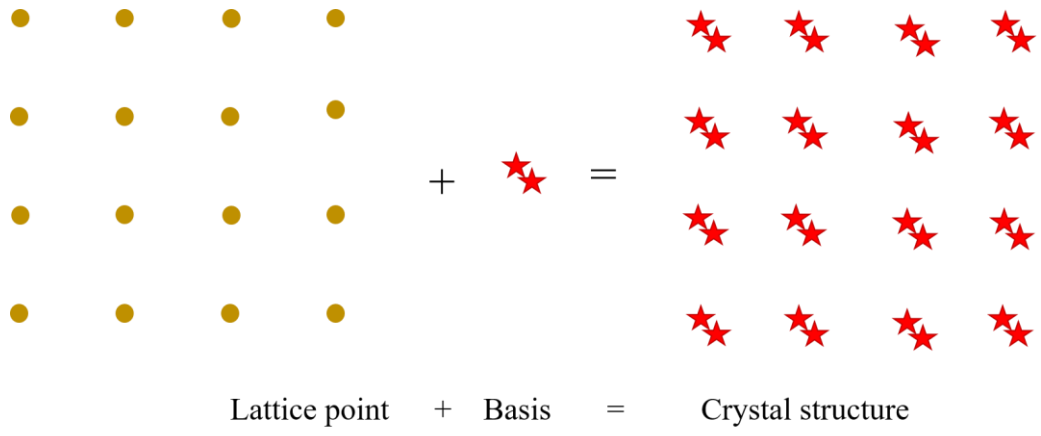

Figure 2.1. A crystal structure defined by lattice point and basis.

Lattice is classified into two groups, Bravais and non Bravais based on the lattice point. Fourteen different Bravais lattice points are discovered by mathematician Auguste

Bravais which are grouped into seven crystal systems (Table 2.1). The lattice parameters for three crystal directions are denoted by **a**, **b** and ***c***, and their respective angles are shown in Figure 2.2. In addition, each crystal structure is defined in two spaces, real space and reciprocal space. The lattice in reciprocal space known as reciprocal lattice is defined by a new vector as-

$$\boldsymbol{G} = n_1\,\boldsymbol{a}' + n_2\,\boldsymbol{b}' + n_3\,\boldsymbol{c}'$$

where, n_1, n_2 and n_3 are integers and, **a**', **b**' and **c**' are the axis vectors of reciprocal lattice which are related to the axis vectors of real lattice. These axis vectors in reciprocal space can be determined by the following equations:

$$\boldsymbol{a}' = 2\pi\,\frac{\boldsymbol{b}\times\boldsymbol{c}}{\boldsymbol{a}\cdot(\boldsymbol{b}\times\boldsymbol{c})}$$

$$\boldsymbol{b}' = 2\pi\,\frac{\boldsymbol{c}\times\boldsymbol{a}}{\boldsymbol{a}\cdot(\boldsymbol{b}\times\boldsymbol{c})}$$

$$\boldsymbol{c}' = 2\pi\,\frac{\boldsymbol{a}\times\boldsymbol{b}}{\boldsymbol{a}\cdot(\boldsymbol{b}\times\boldsymbol{c})}$$

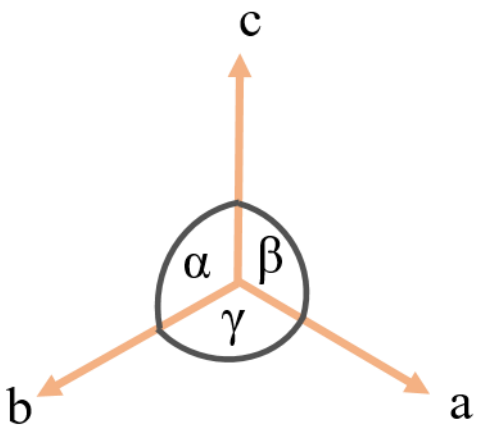

Figure 2.2. Axis parameters for 3D crystal.

Table 2.1. Fourteen Bravais lattices categorized into seven crystal system with their geometrical parameters.

System	Bravais lattice	Unit cell parameter
Cubic	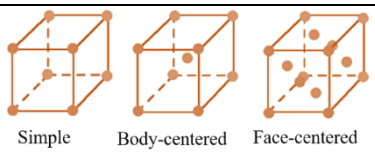	a = b = c, α = β = γ = 90°
Tetragonal	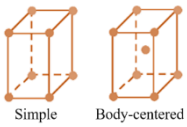	a = b ≠ c, α = β = γ= 90°
Orthorhombic	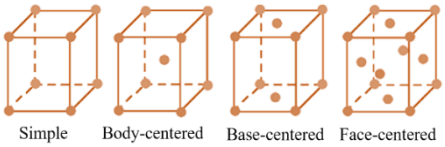	a ≠ b ≠ c, α = β = γ= 90°
Rhombohedral		a = b = c, α = β = γ ≠ 90°
Hexagonal	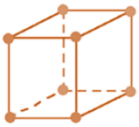	a = b ≠ c, α = β = 90°, γ = 120°
Monoclinic	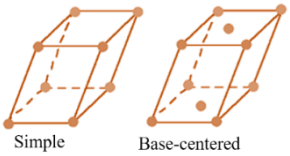	a ≠ b ≠ c, α = γ = 90°, β ≠ 90°
Triclinic		a ≠ b ≠ c, α ≠ β ≠ γ

2.1.2 Overview of 2D lattice

In surface crystallography, this surface is undoubtedly 2D objects showing periodicity in two directions. The surface lattice is defined by using two translational vectors, **a** and **b,** which can be expressed as-

$$\boldsymbol{r} = \boldsymbol{r}' + n_1\,\boldsymbol{a} + n_2\,\boldsymbol{b}$$

Table 2.2. Five 2D Bravais lattices including their geometric parameters.

Bravais lattice	Structure	Unit cell parameter
Square	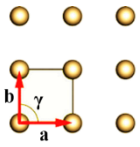	a = b, $\gamma = 90^{\circ}$
Rectangular	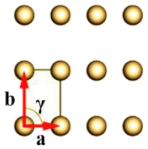	a ≠ b, $\gamma = 90^{\circ}$
Oblique	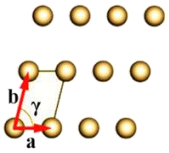	a ≠ b, $\gamma \neq 90^{\circ}$
Centered-rectangular	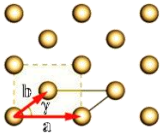	a ≠ b, $\gamma \neq 90^{\circ}$
Hexagonal	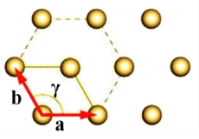	a = b, $\gamma = 120^{\circ}$

To understand the surface structure, it is necessary to define this structure in terms of its 2D lattice and basis, which follows the same concept of the bulk crystal. All the surface lattices are grouped into five types which are known as 2D *Bravais* lattices. In Table 2.2, five 2D *Bravais* lattices are listed with their geometric parameters.

2.1.3 Miller indices

A particular plane of a crystal is denoted by Miller index, which is determined from the intercepts of the plane along the three crystallographic axes and represented by (hkl). A group of equivalent planes and the direction of that plane are denoted by {hkl} and [hkl], respectively. Some planes of cubic crystal are shown in Figure 2.3.

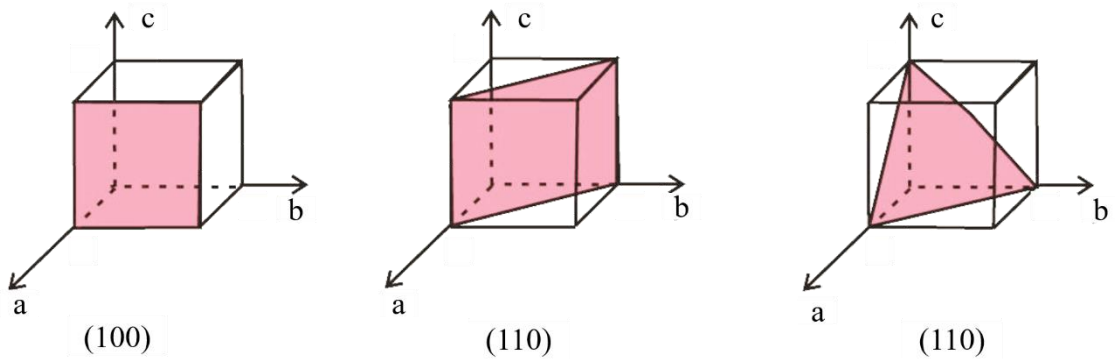

Figure 2.3. Miller indices of cubic crystal structure.

Inter-distance between two equivalent planes can be measured from Miller indices by the following equation-

$$d_{hkl} = \frac{a}{\sqrt{h^2 + k^2 + l^2}}$$

here, a is the lattice constant of a cubic crystal.

Miller indices are classified into two groups: low index Miller plane and high index Miller plane. Low index Miller planes are referred to as those planes which the cut along the closely packed plane. High index Miller planes are cut along the rest of the directions, such as, along the steps of the surface.

2.1.4 Surface relaxation and reconstruction

Surface properties are different from bulk crystal which can be described in terms of surface energy. Atoms of the surface possess higher energy compared to bulk atoms due to the broken bonds. The number of broken bonds, also known as dangling bonds, varies based on the orientation of surface atoms. The energy of the surface is calculated by the following equation-

$$\gamma = \frac{1}{2} N_b \, \varepsilon \, \rho_a$$

here, N_b is the number of broken bonds for the formation of the surface, ε is the energy of the bond, and ρ_a is the number of atoms per unit area on the surface.

The excess energy of the surface due to the lack of neighboring atoms forces the structure of top layers to be modified to reduce this energy. This phenomenon leads to relax or reconstruct the top atomic layers of crystal.

However, the modification of surface atoms depends on the configuration of bulk structure. The surfaces of metal and semiconductor exhibit different phenomena as the metal possesses not directed metallic bond with delocalized electron gas while directional bonding is found in semiconductor. Hence, the effect of breaking bond during surface preparation is more prominent for semiconductor.

2.1.4.1 Surface relaxation

In normal surface relaxation, interlayer spacing between the first few atomic layers of crystal are modified by keeping the atomic position of surface atoms same as bulk atoms. In most cases, first interlayer spacing is contracted compared to the bulk interlayer spacing and this change in spacing is damped in an oscillatory way for the deeper region. Along with, the surface atomic layer can be displaced in parallel direction with respect to the bulk layer which is known as parallel or lateral relaxation. In Figure 2.4, surface relaxation in two ways is shown.

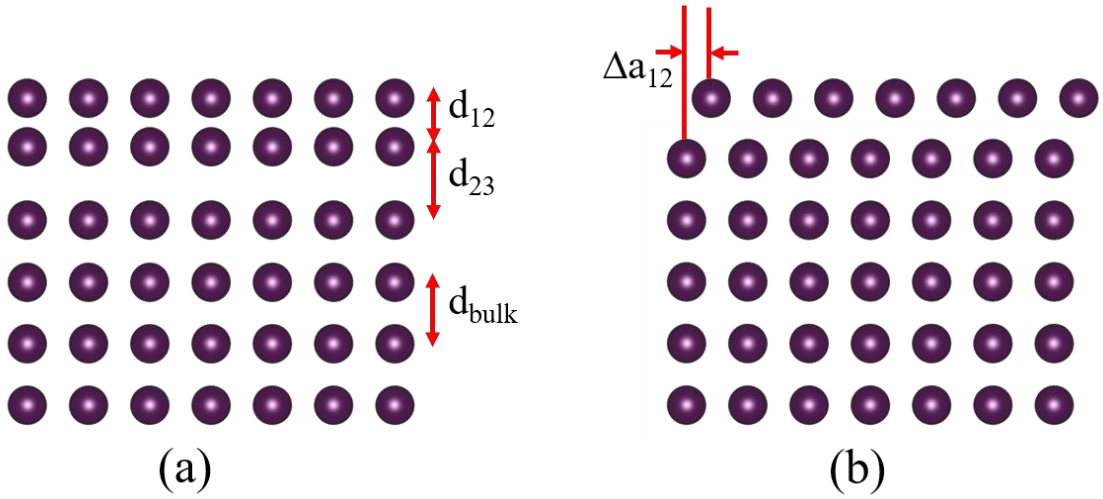

Figure 2.4. Schematic presentation of (a) normal and (b) lateral surface relaxation.

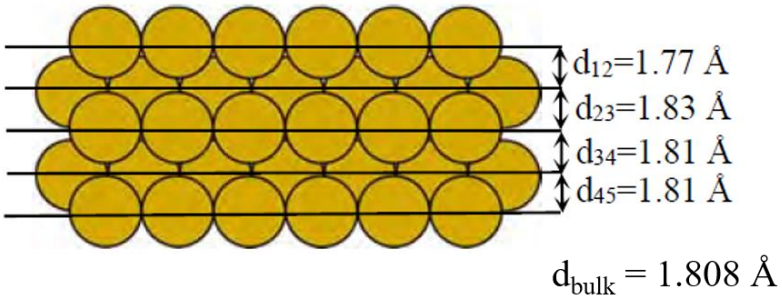

Figure 2.5. Surface relaxation of clean Cu(100) [Copied from ref [1]*].*

Most of the metal surfaces, such as, Cu(100) [2], Al(110) [3] etc. show normal relaxation with some exceptions due to the lack of localized directional bonding which is considered as the main reason for the reconstruction of the surface. In Figure 2.5, relaxation of clean Cu(100) surface is shown in which the vertical shifting of atoms is indicated.

2.1.4.2 Surface reconstruction

Reconstruction of surface involves alteration of the atomic structure of surface layer compared to the bulk structure. The symmetry and periodicity of reconstructed surfaces are different from those of bulk structure in most cases. Preservation of the number of atoms on the top layer classifies surface reconstruction into two ways- conservative reconstruction and non-conservative reconstruction.

In conservative reconstruction, atoms are only displaced from their original position, maintaining the same number of atoms on the surface as in bulk. While in non-conservative reconstruction, the number of atoms on the surface layers is different from the number of atoms in the bulk layer. A pictorial view of both surface reconstructions is shown in Figure 2.6.

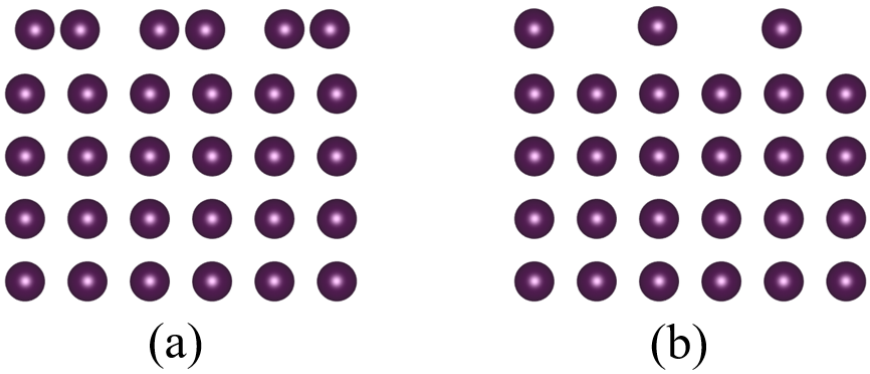

Figure 2.6. Schematic representation of (a) conservative and (b) non-conservative surface reconstruction.

2.1.4.2.1 Reconstruction of clean surface

Surface reconstruction is generally occurred for semiconductors due to having covalent bonding which is directional. While, reconstruction is also observed on the clean (100) surface of bcc refractory metals, i.e., W, Mo, below room temperature as well as some 5d fcc metals, including Pt, Ir, Au, are exhibited significant reconstruction [4–7]. In these cases, tensile surface stress for the unreconstructed surface is too large which lead to rearrange the surface atoms in parallel directions and regain the charge density similar to the bulk.

It was found that non-reconstructed ideal W(100) surface exhibiting square periodicity formed a zigzag structure on the surface by the lateral movement of W atoms along [110] and [$\bar{1}\bar{1}$0] directions and thus formed c(2×2) structure below temperature. The transition of W(100) surface from (1×1) to c(2×2) is reversible [8]. The reconstruction for W(100) surface might be related to the high density of d-electron states at the Fermi level. Moreover, for Pt(100), a loosely packed surface having (1×1) structure formed a close-packed quasi hexagonal (1×5) structure to become stable [9]. A schematic of the reconstructed Pt(110) surface is shown in Figure 2.7 in which missing row reconstruction is occurred by making the surface rougher.

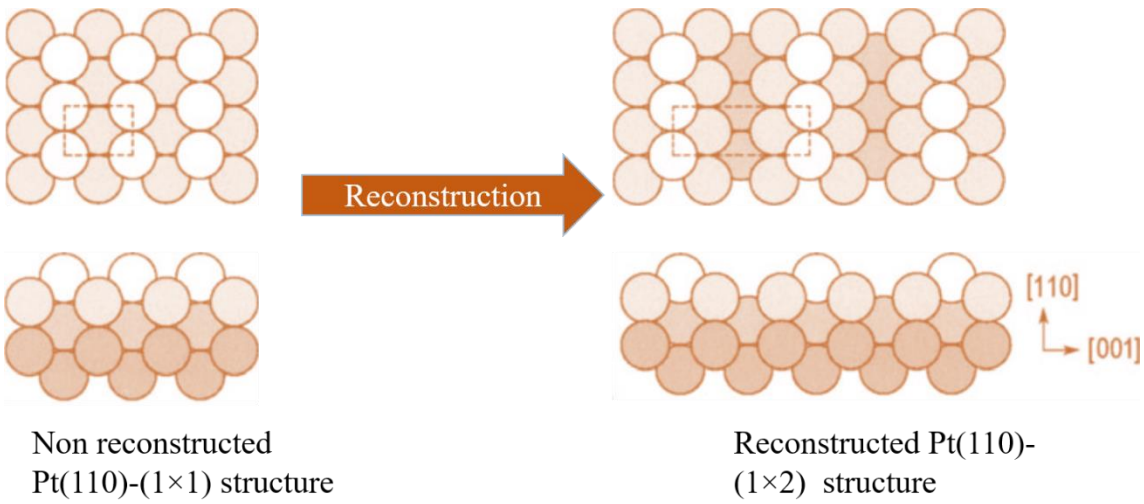

Figure 2.7. Surface reconstruction of clean Pt(110) surface.

2.1.4.2.2 Reconstruction of adsorbate induced surface

Foreign material deposition on a clean surface forms new chemical bonds between adsorbate and adsorbent or adsorbate and adsorbate, altering the surface structure. It has already been claimed that adsorption of several adsorbates, such as oxygen, hydrogen, alkali metals etc., on clean, non-reconstructed ideal metal surface undergoes reconstruction. For example, alkali metal, Li, adsorption onto the clean surfaces of Al(100) and Si(100) forms (2×2) and (2×1) superstructures, respectively [10,11].

The superstructure formed on any substrate is dependent on adsorbate's coverage. In addition, hydrogen adsorption on W(100) generates c(2×2) structure at room temperature by modifying the movement of surface atoms which is different from the c(2×2) structure of clean W(100) surface [12]. As the surface reconstruction due to adsorption of foreign atoms depends on some factors, including the interaction between substrate and adsorbate, surface coverage, and ambient condition, researches are carrying on to understand the reconstruction of the surface.

2.1.5 Surface structure notation

As the surface is not necessarily similar to its bulk structure, naming the overlayer with respect to the bulk is essential. The surface structure can be defined in two ways, matrix notation and Wood's notation. In Figure 2.8, schematic views of these two surface notations are shown.

2.1.5.1 Matrix notation

Park and Madden introduced matrix notation in 1968 [13] to define the 2D surface structure by establishing a relation between the surface translational vectors (**a_s** and **b_s)** and the vectors of the ideal substrate plane (**a** and **b)**. In matrix notation, these vectors are linked by the following equations-

$$\boldsymbol{a_s} = G_{11}\boldsymbol{a} + G_{12}\boldsymbol{b}$$

$$\boldsymbol{b_s} = G_{21}\boldsymbol{a} + G_{22}\boldsymbol{b}$$

Then, the superstructure is defined by the following matrix-

$$G = \begin{pmatrix} G_{11} & G_{12} \\ G_{21} & G_{22} \end{pmatrix}$$

The surface structure, whether commensurate or incommensurate, can be recognized from the values of the elements of the matrix.

2.1.5.2 Wood's notation

Wood's notation proposed by Elizabeth A. Wood [14] is mainly suited for commensurate structure. This notation is specified by considering the ratio of the lengths of translational vectors of surface and bulk plane as well as the rotation of unit mesh of surface with respect to the substrate. If a superstructure forms on the substrate surface M(hkl) with the translational vectors of-

$$|\boldsymbol{a_s}| = m|\boldsymbol{a}| \text{ and } |\boldsymbol{b_s}| = n|\boldsymbol{b}|$$

and with an angle of rotation α˚; then, Wood's notation of superstructure is defined as-

$$M(hkl)(m \times n) - R\alpha^{\circ} - A$$

Here, A is the chemical symbol of surface atoms; for clean surface A=M.

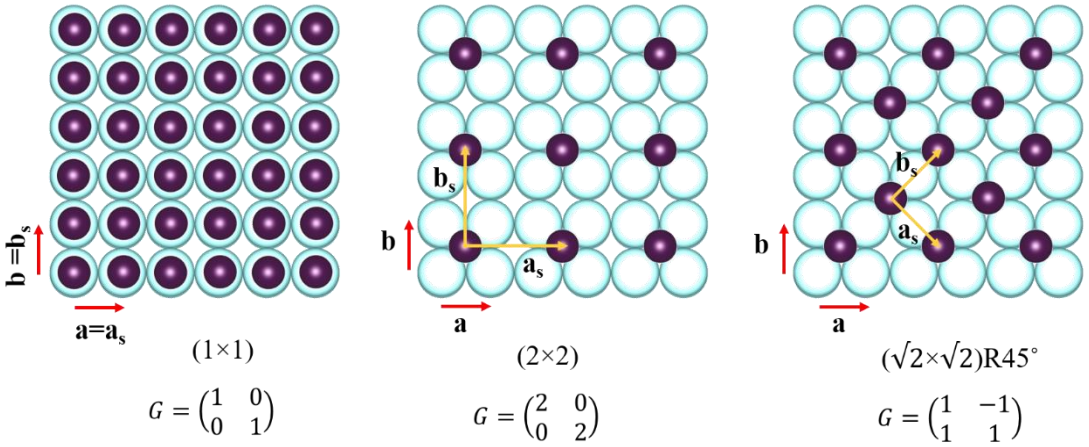

Figure 2.8. Representation of matrix and Wood's notation of some superstructures on the square lattice.

2.2 Materials

2.2.1 Boron

Boron (B) is a half metal element that is rare in its elemental form on earth. Naturally, it is found in compounds, especially as borate minerals. B was first recognized as an element in 1808 by Sir Humphry Davy, Joseph Louis Gay-Lussac, and Louis Jacques Thénard [15]. Weintraub prepared pure B in 1909 after continuing long research on bulk B allotropes [16].

B atom positioned next to carbon in the periodic table consists of 5 electrons. The electron configuration of B is $1s^2 2s^2 2p^1$ which indicates the lack of electron in valence orbital. The presence of electron deficiency in B atom leads to form multi-center-two electrons bonds and the two-center-two-electrons (2c-2e) bond, which allowing B to construct several B allotropes and compounds with other materials [17].

2.2.1.1 Structures of bulk boron

The crystal structure of B allotropes is unique and complicated due to having complex bonding configurations. The building block of crystalline B structure is B_{12} icosahedron which is shown in Figure 2.9 along two other icosahedra, B_{21} and B_{28}.

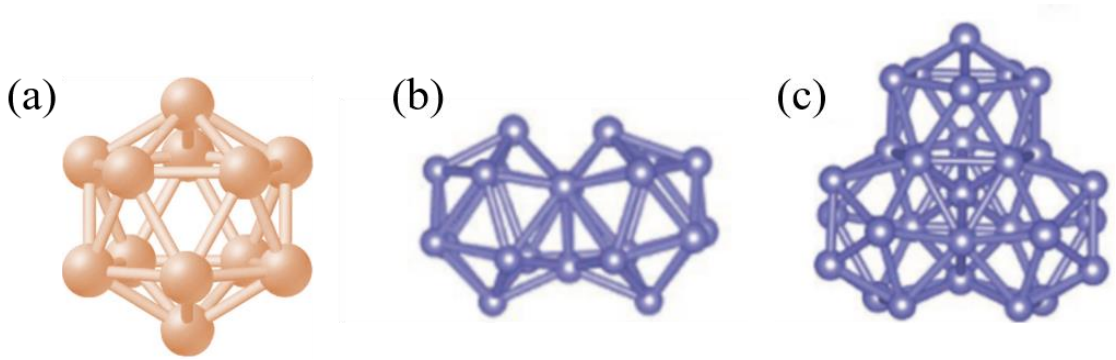

Figure 2.9. The structures of (a) B_{12}, (b) B_{21}, and (c) B_{28} icosahedra [Copied from ref [18]].

Among reported 16 B allotropes, only four allotropes, named as, α-rhombohedral, β-rhombohedral, β-tetragonal, and γ-orthorhombic, are thermodynamically stable [18]. Some allotropes of boron are shown in Figure 2.10.

As the B is electron-deficient atom, in the icosahedron of B, every B atom creates bonds with neighboring five atoms forming 3c-2e bonds with having maximum electron density at the middle of the triangular B structure. α-rhombohedral B containing one B_{12} icosahedron per rhombohedral unit cell which forms both 2c-2e and 3c-2e bonds (Figure 2.10(a)); was recognized in 1958 [19,20] and β-rhombohedral B is possessing larger unit cell comprising of 1 single B atom at center, 8 and 12 B_{12} icosahedra at the corner and middle of the edges of the unit cell, respectively; and two B_{28} (Figure 2.9(c)) (3 icosahedra fused together) icosahedra inside the unit cell (Figure 2.9(b)) [21]. Among these two structures of B, α-rhombohedral B is more stable at low temperature than β-rhombohedral B. α-tetragonal and β-tetragonal B structures as shown in Figure 2.10(d,e)) are composed of B_{12} icosahedra, B_{21} (2 icosahedra fused together) icosahedra (Figure 2.9(b)) and B interstitials. γ-orthorhombic B structure consists of 2 B_{12} icosahedra and 2 B_2 pairs in each

unit cell which is stable at high temperature and high pressure (Figure 2.10(c)). Icosahedra of γ-orthorhombic B structure are attached by 2c-1e bonds as well as strong 3c-2e and 2c-2e are existed in B_2 pairs and in the connection between icosahedra and B_2 [18].

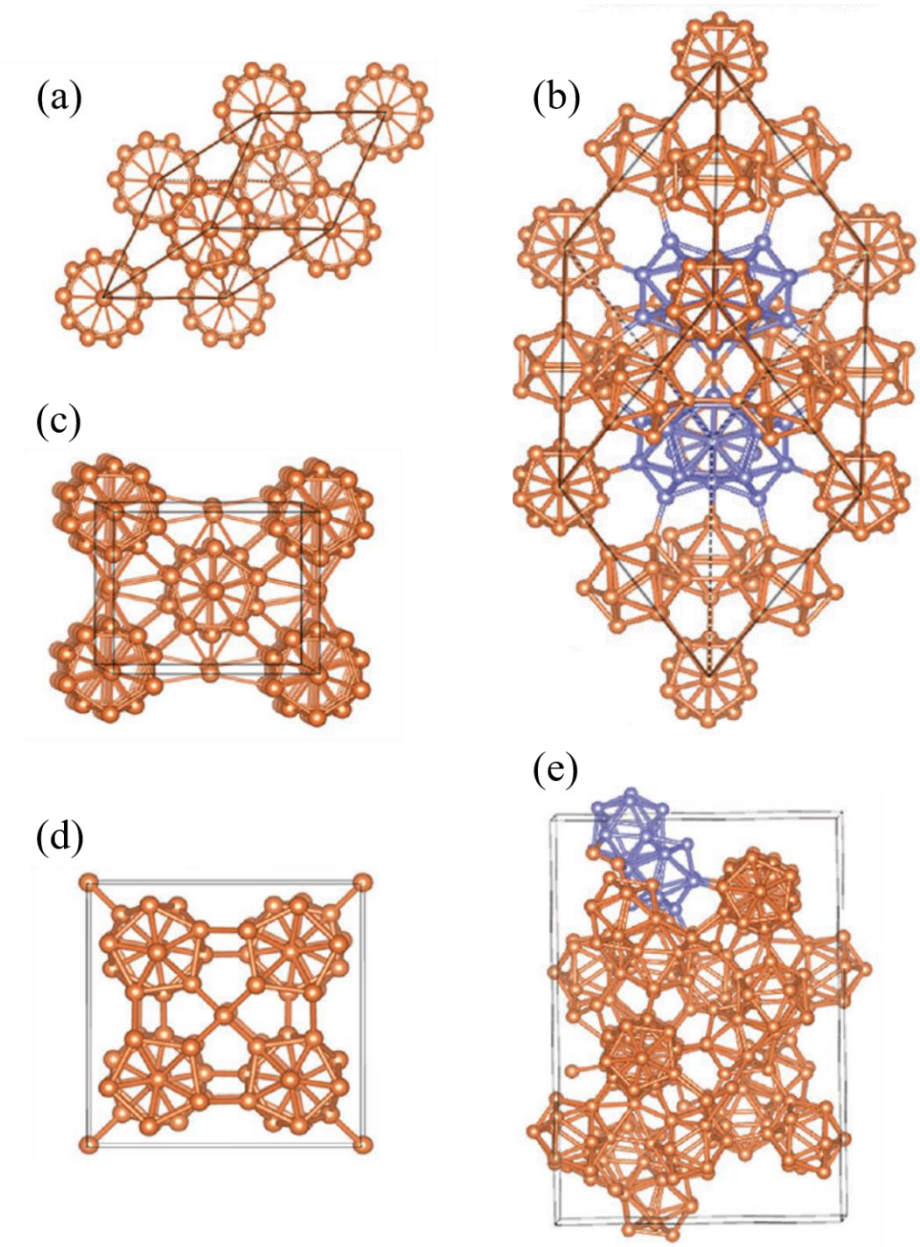

Figure 2.10. The structure of B allotropes [Copied from ref [18]*]. [(a) α-rhombohedral, (b) β-rhombohedral, (c) γ-orthorhombic, (d) α-tetragonal and (e) β-tetragonal B structure]*

2.2.1.2 Boron clusters in planner form

For the crystalline structure of B allotropes, B_{12} icosahedron is considered as the building block. Apart from this, B cluster in both cage and planar has drawn research interest after the theoretical prediction of B clusters by Boustani in 1997 [22]. Until now, B clusters with the number of B atoms ranging from 3 to 40 were introduced [23,24].

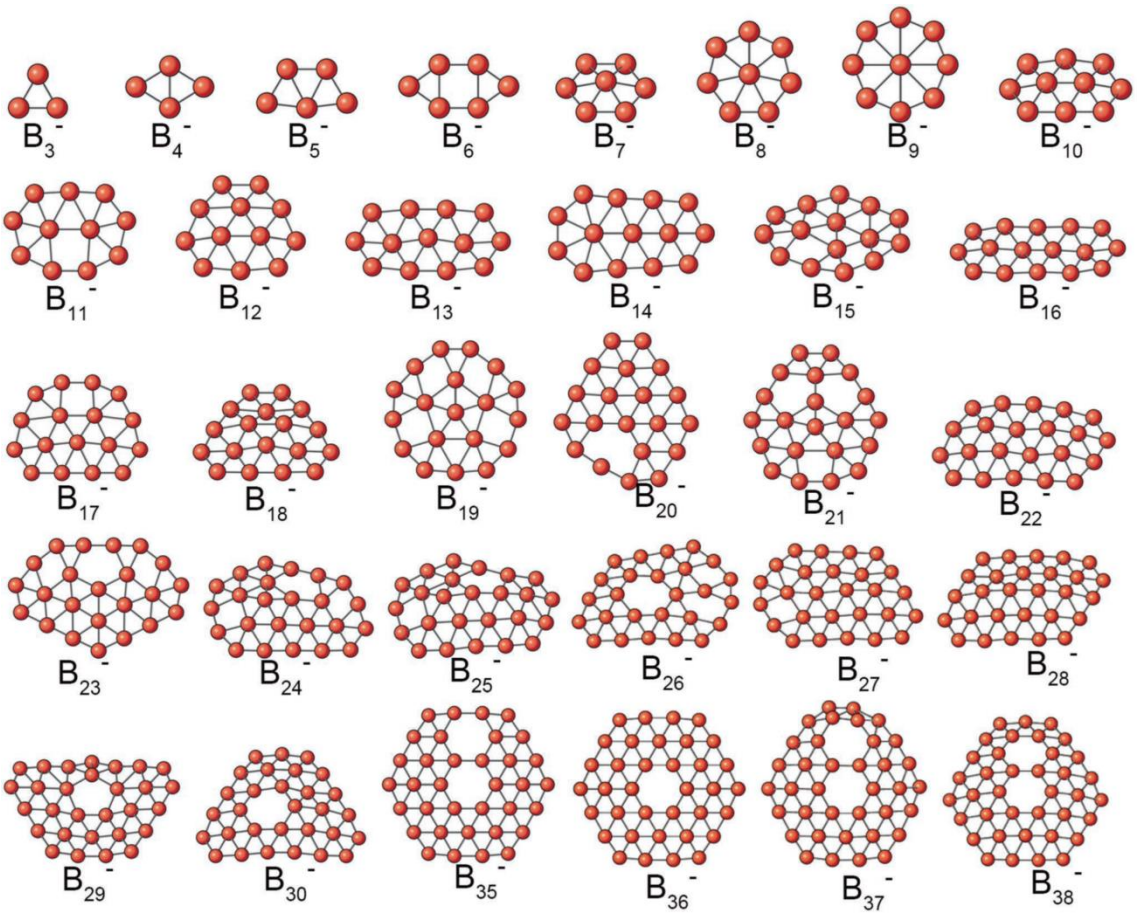

Figure 2.11. Structure of boron clusters [Copied from ref [32]*].*

Boustani proposed some stable B clusters in quasi planar form comprised of hexagonal pyramids using 'Aufbau principle', which is considered as the initial form of the 2D planar B. In 1988, the preparation of B cluster experimentally was reported by Hanley et al. [25]. However, the confirmation of structure by spectroscopy with ab initio calculations was done in 2020 and the electronic properties of B_5^- and B_5 with their chemical bonds was explained experimentally [26]. Afterward, B_8^- and B_9^- planar

structures with aromaticity were proposed by Zhai et al. in 2003 [27]. Aromatic clusters (B_{11}^-, B_{12}^- and B_{15}^-) and antiaromatic clusters (B_{13}^- and B_{14}^-) were deduced [28]. Later, other planar B structures such as, B_{16}^-, B_{19}^-, B_{20}^-, B_{22}^- and B_{23}^-, were reported experimentally [29,30]. In addition, a planar B cluster, B_{36}^- with a hexagonal hole at the center was deduced by Piazza et al., in 2014, which was the first experimental evidence of forming 2D B sheet with hollows [31]. Some B clusters are shown in Figure 2.11.

2.2.1.3 2D boron structure

Transformation of quasi planar/ planar structure of B into cage like structure with the increase of the size of B cluster enhanced the possibility of forming 2D flat B earlier. B_{80} buckyball was proposed by Szwacki et al. in 2007, which is similar to C_{60} in both structural and symmetrical ways [33]. It was observed that flattening B_{80} will create a B sheet, named as α-sheet. While graphene exhibits a simple honeycomb structure due to the sp^2 hybridization of carbon atom, 2D B sheet shows complicated structure because of its rich chemistry. Electron deficiency in B atom makes the honeycomb structure unstable. Moreover, multi-center-two electron bonds formed in bulk B structure also indicate the complexities of fabricating single layer of B. To overcome the instability due to the lack of electron, Tang et al. claimed that B monolayer with honeycomb motif and triangular motifs may balance the electron deficiency to make this stable [34]. Thereby, numerous 2D B structures were proposed by changing the B vacancy in a triangular sheet. The hole concentration in triangular sheet is defined by hexagonal hole density, η as:

$$\eta = \frac{Number\ of\ hexagonal\ holes\ in\ B\ sheet}{Number\ of\ B\ atoms\ in\ triangular\ B\ sheet}$$

B sheet was named differently, such as, α-sheet, β-sheet, χ-sheet, δ-sheet by considering the coordination number for B atoms in 2D B sheet, which is listed in Table 2.3.

Table 2.3. Naming of B sheet based on the coordination number.

Name of B sheet	Coordination number
α-sheet	5,6
β-sheet	4,5,6
χ-sheet	4,5
ψ-sheet	3,4,5
δ-sheet	One single value

In addition, to compensate the electron deficiency of B, another way was predicted; to use foreign substrate, which will be the source of extra electron required to form B sheet. Theoretically, it was proposed that a stable B sheet can be formed on several substrates such as, Cu, Ag, Au or metal boride by Liu et al. [35]. Fabricated B sheets can be buckled or non-buckled depending on the interaction of B atoms with the substrate. After theoretical prediction of B sheet over two decades, the first B sheet was experimentally synthesized in 2015 by Mannix et al. [36]. Recently, many attempts are carried out to fabricated 2D flat B sheet on several substrates. Few structures of B sheet are shown in Figure 2.12.

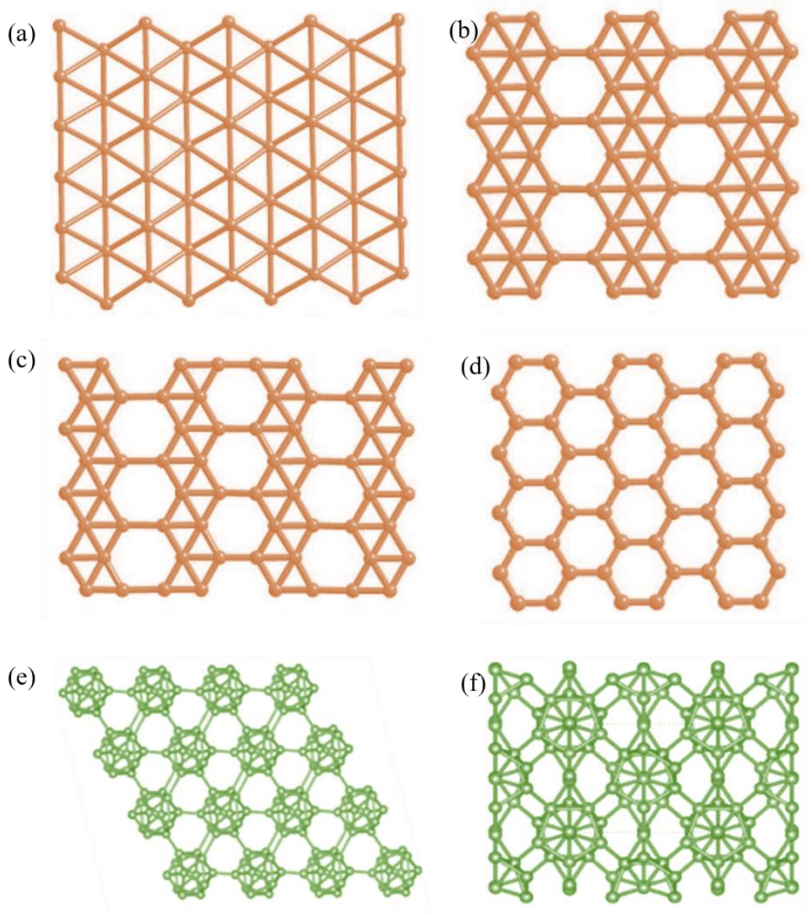

Figure 2.12. Structure of 2D boron sheets- (a)stripped B sheet, (b)β_{12} sheet, (c)χ_3 sheet, (d) graphene like sheet, (e) α icosahedral sheet and (f) γ icosahedral sheet.

2.2.2 Refractory metals

Refractory metals are unique metals due to possessing high resistance to heat, wear and corrosion. Form the basic definition, five elements from group 5 and 6 are considered as refractory metals. These are- niobium (Nb), molybdenum (Mo), tantalum (Ta), tungsten (W) and rhenium (Re). All of these metals show quite similar properties, such as high metal point, more than 2200˚C. Some additional elements are also recognized as refractory metals based on wider definition which includes metals having melting point above 1850˚C. In Figure 2.13, refractory elements are shown in the periodic table.

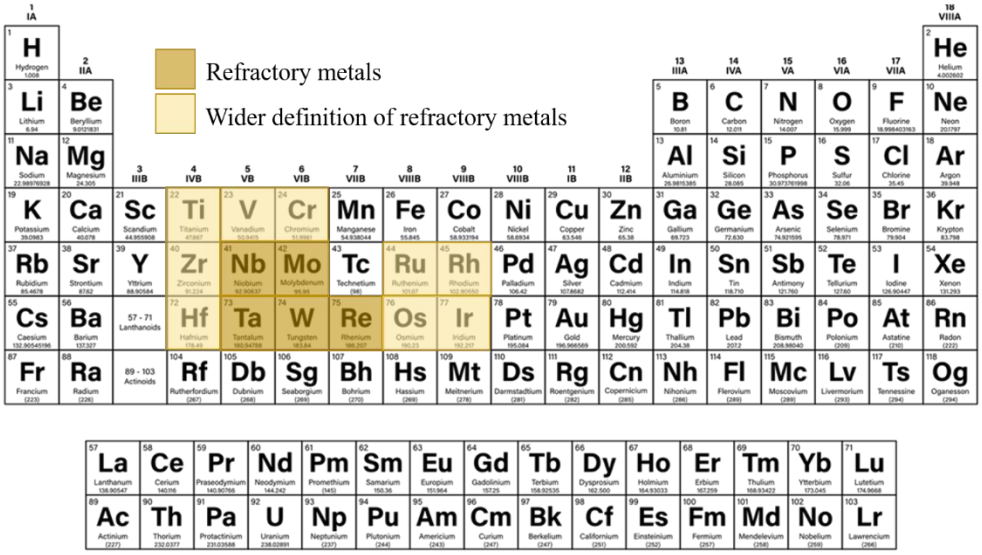

Figure 2.13. Periodic table showing the refractory metals.

The remarkable physical properties of these metals include hardness, high melting and boiling points, good conductivity, high density and so on. These are very important in technology. Moreover, these elements can form numerous stable compounds with each other and different metallic elements in two or more oxidation states [37].

2.2.2.1 Tungsten

Tungsten, also known as wolfram, is a chemical element with the symbol of W. This is a refractory metal positioned in group 6 of the periodic table, which is naturally available, especially in compounds with different elements. W is a rigid steel grey brittle metal at room temperature that can be turned into fine thin wire by mechanical work at high temperature. As W can form numerous alloy, this is suitable for lamb bulb filament materials, X-ray tubes, radiation shielding etc. Due to its hardness and high density, this is also used in military applications [38]. Elemental properties of W are listed in Table 2.4.

Table 2.4. Elemental properties of W.

Atomic number	74
Electron configuration	[Xe] $4f^{14}5d^{4}6s^{2}$
Atomic mass	183.85
Density	19.3 grams/cm^3
Melting point	3410˚C
Boiling point	5660˚C
Oxidation states	+2, +3, +4, +5, +6
State at 20˚C	Solid

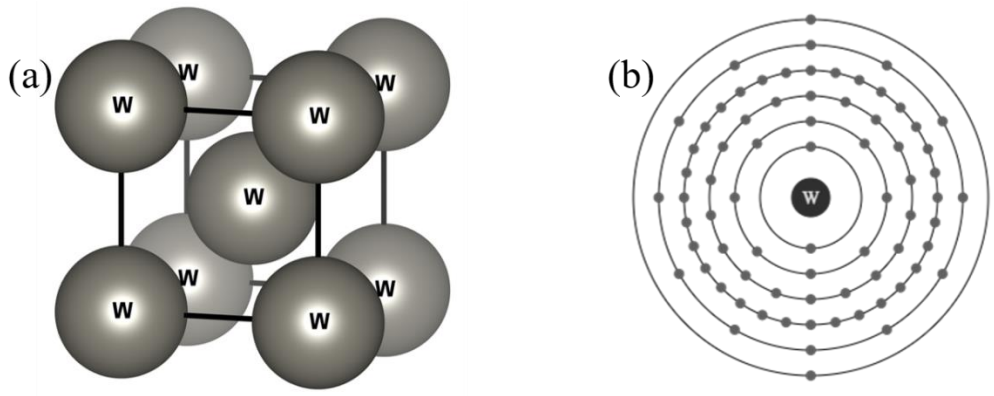

Figure 2.14. (a) Crystal structure of W and (b) electron configuration of W atom.

Naturally, available W exists in five stable isotopes- ^{180}W, ^{182}W, ^{183}W, ^{184}W, and ^{186}W. It has two crystalline phases, α and β phase. α phase of W is more stable than β phase and has body centered cubic (BCC) structure with a lattice constant of 3.16 Å. The crystal structure and electron configuration on W are shown in Figure 2.14.

2.2.2.2 Molybdenum

Molybdenum is a refractory metal with the symbol of Mo. This is not available as a free metal in nature but can be found in minerals as oxidized state. High melting point and strength make this material to be used in military armor, industrial motors, electrical contacts etc. [39]. Elemental properties of Mo are listed in Table 2.5.

Table 2.5. Elemental properties of Mo.

Atomic number	42
Electron configuration	[Kr] $4d^5 5s^1$
Atomic mass	95.95
Density	10.2 grams/cm^3
Melting point	2610˚C
Boiling point	4639˚C
Oxidation states	+2, +3, +4, +5, +6
State at 20˚C	Solid

The crystal structure of Mo is BCC with a lattice parameter of 3.15 Å. Mo can form various compounds by changing its oxidation state from –II to +VI. Till now, 35 isotopes of Mo are found. The crystal structure and electron configuration on Mo are shown in Figure 2.15.

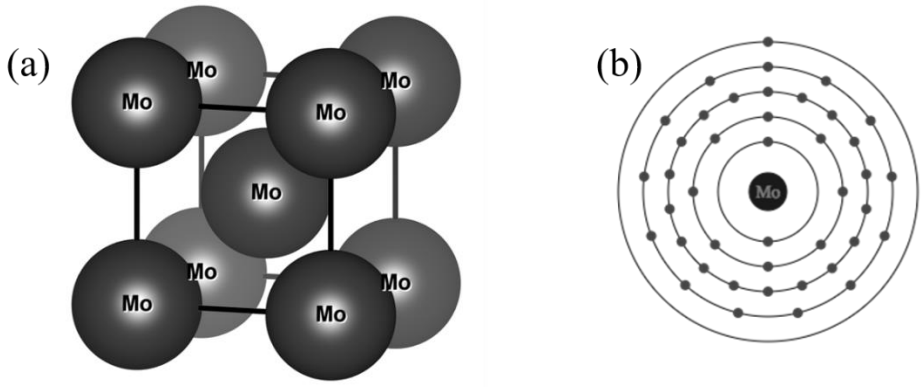

Figure 2.15. (a) Crystal structure of Mo and (b) electron configuration of Mo atom.

2.3 Experiment

All the experiments were conducted in UHV condition maintaining the base pressure around 2×10^{-8} Pa separately. Four pumps, rotary vane pump, turbo molecular pump, ion pump, and Ti sublimation pump, were utilized to achieve this low pressure. First, the rotary vane pump decreased the pressure level of the chamber around 10^{-2} Pa, which further reduced to 10^{-5} Pa by using turbo molecular pump. Afterwards, the combination of ion and Ti sublimation pump lowered the pressure of the chamber rapidly to ~10^{-8} Pa. These all four pumps were required to maintain the UHV condition of chambers.

LEED chamber was equipped with four grid LEED optics and LEED I(E) measurement system. One of the most important parts of LEED system is electron gun which consists of several electronic lenses for controlling electron emission. Filament made by lanthanum hexaboride is used for emitting electrons. In the XPS chamber, measurements were conducted by using a non-monochromatic MgK_α X-ray source with photo energy ($h\upsilon$) of 1253.6 eV. The source emission current was retained at around 15 mA with a 15 KeV of anode voltage, and the pass energy was fixed at 40eV. The STM chamber, samples were scanned at low temperature (77K) using PtIr tip. LEED apparatus is attached in both XPS and STM chamber to confirm the sample preparation. The schematic of the experimental set-up is shown in Figure 2.16.

In each chamber, the sample was held by a non-magnetic holder which was attached with a manipulator for 360˚ rotation of the sample. E beam evaporator was used to deposit source material on substrates. Deposition rate was determined by quartz crystal microbalance (QCM). The samples were annealed at several temperatures by applying DC current and high voltage. An infrared pyrometer was utilized to measure the temperature.

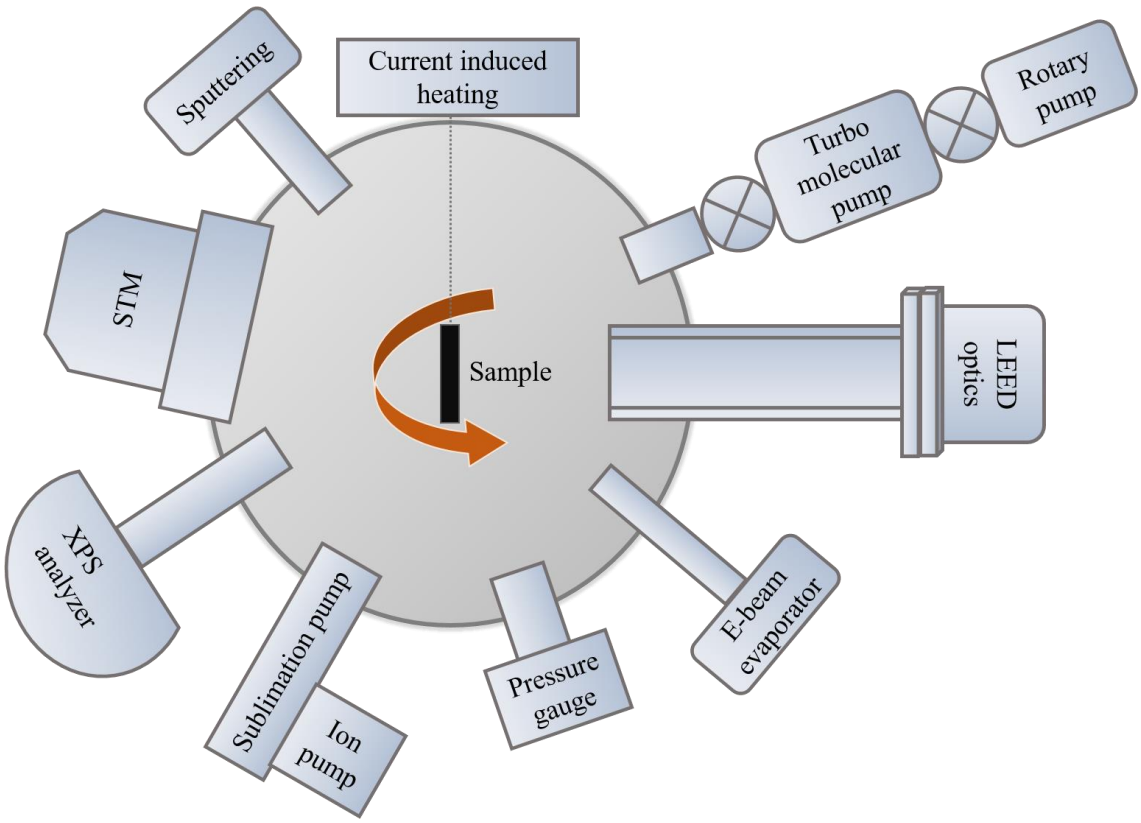

Figure 2.16. Schematic diagram of experimental set-up under UHV condition.

2.3.1 Low energy electron diffraction (LEED)

LEED is considered as one of the most important surface analyzing techniques for the determination of surface structure. The first LEED experiment conducted by Clinton Davisson and Lester Germer in 1927 [40] at Bell labs leads many more experiments with various diffraction techniques to be developed till now [41].

In the robust surface analyzing technique, LEED, highly focused electrons incident on the sample within the energy range of 20-1000 eV. Within this energy range of electron, inelastic mean free paths (IMFP) will be in between 5 – 20 Å, indicating penetration of electron is confined into the first few layers of bulk. The IMFP with the electron energy is calculated by the following equation.

$$\lambda\,(IMFP) = \frac{538\,a}{E^2} + 0.41\,a^{\frac{3}{2}}E^{\frac{1}{2}}$$

here, E is the electron's kinetic energy, and a is the mean atomic diameter. This surface sensitivity with the electron energy is shown in 2.17.

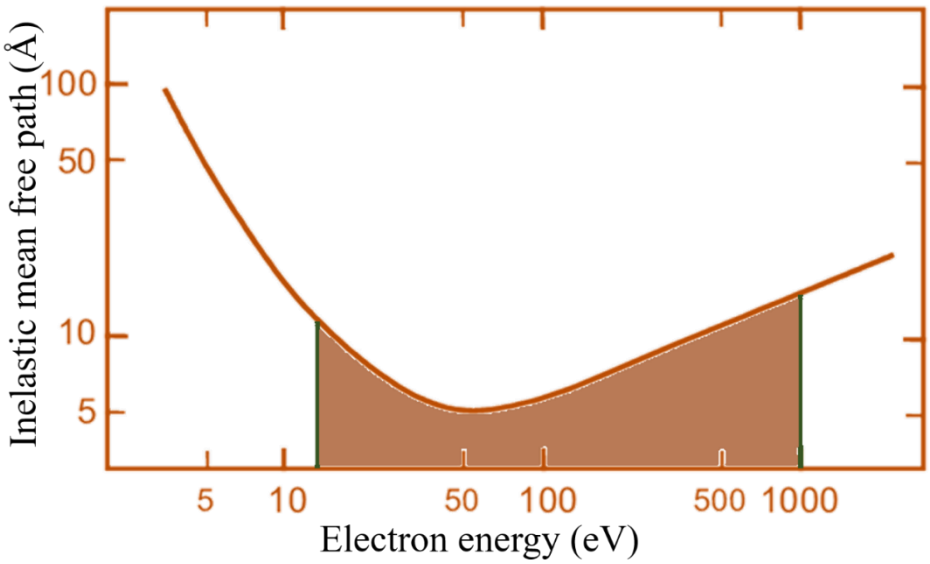

Figure 2.17. Universal curve exhibiting the IMFP variation with change of electron energy.

The wavelength of the ejected electrons in this range is found in between 2.7 – 0.39 Å, which can be determined by using de Broglie equation-

$$\lambda(\text{Å}) = \left(\frac{150.6}{E(eV)}\right)^{\frac{1}{2}}$$

The schematic of the LEED system is shown in Figure 2.18. In this system, monochromatic electron beam with varying the energy in between 20 -1000 eV is incident on the sample from electron gun consisting of cathode and several focusing lenses for generating low energy electrons. Then, the diffracted electrons pass through four grids to filter out the non-elastic electrons. As a result, only remaining elastic electrons direct on the fluorescent screen. These diffracted electrons produce bright pattern on dark background, which resembles the crystal structure of the surface.

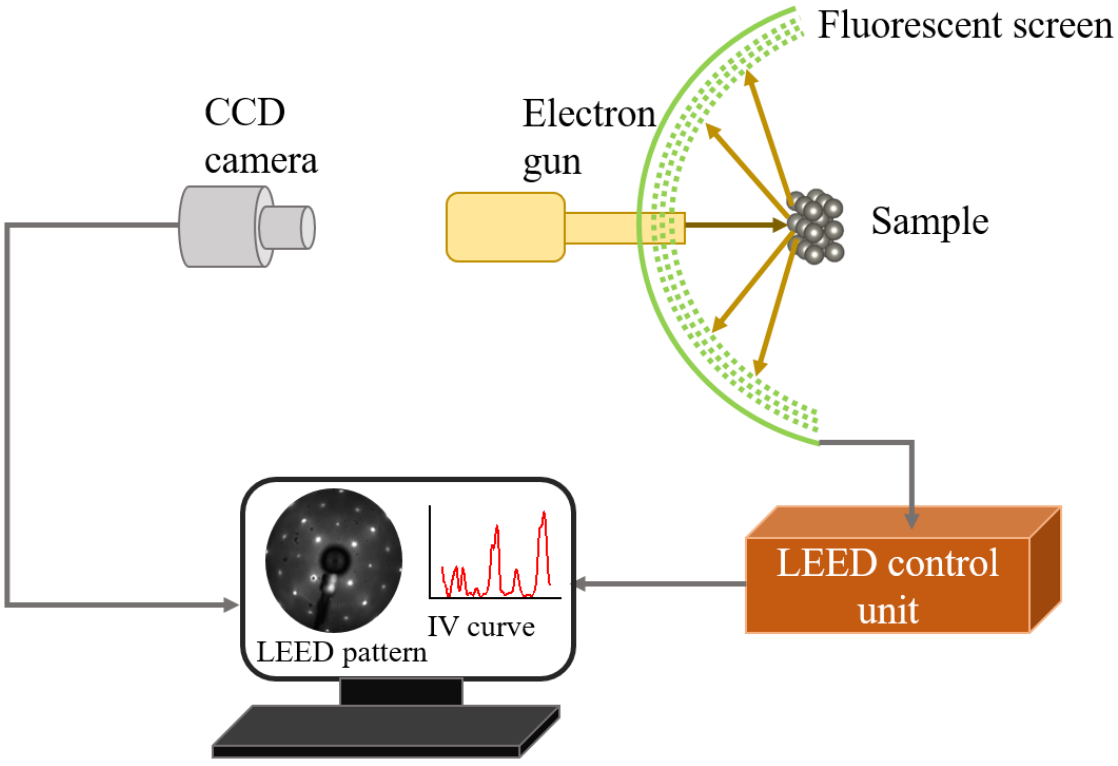

Figure 2.18. Schematic diagram of LEED system.

Obtained results from LEED can be analyzed both quantitatively and qualitatively. In qualitative analysis, lattice spacing with symmetry and periodicities can be obtained from the LEED pattern. Deviation of surface properties with ideal order can be determined from the spot profile in quantitative analysis. The combination of both analyses makes LEED experiment a prominent tool for surface characterization.

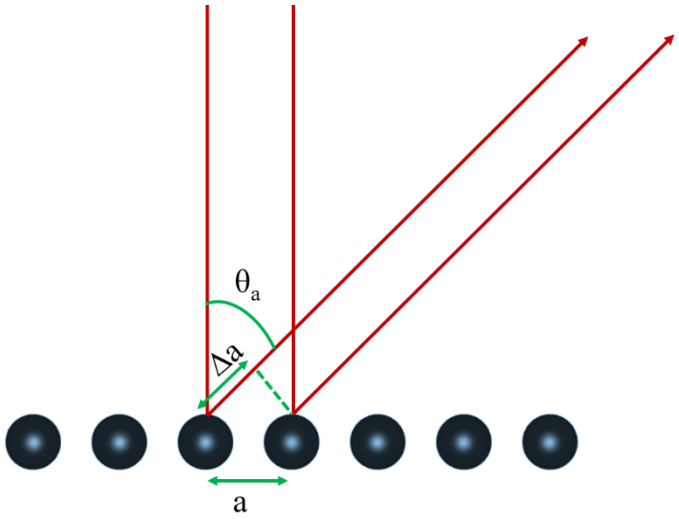

Figure 2.19. Representation of electron diffraction from one dimensional array.

To understand the LEED pattern, first consider the diffraction from one dimensional (1D) array with a lattice constant of, a, which is depicted in Figure 2.19. For constructive interference, the diffraction condition needs to follow the following equation-

$$\Delta a = n\lambda = a\ sin\theta_a$$

Therefore, the path length difference, Δa, needs to be equal to the integer number of wavelengths, λ, of electrons.

Now, it can be rewritten as-

$$sin\theta_a = \frac{n\lambda}{a}$$

Thus, the pattern will be observed in series of lines in the perpendicular direction with the 1D lattice. The periodic spacing in the diffracted pattern is inversely related to the atomic spacing in real space, as shown in Figure 2.20 (a).

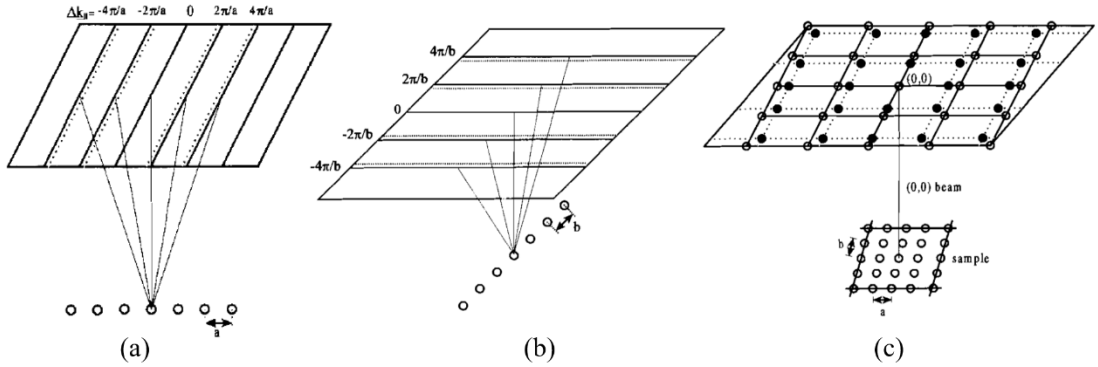

Figure 2.20. Diffraction patterns for (a) 1D array in a certain direction, (b) 1D array in perpendicular direction of Figure (a) and (c) 2D array combining both Figure(a) and (b). [Copied from ref [42] *]*

Alternatively, the diffraction pattern can represent with electron wave vectors and reciprocal lattice vectors. If the incident electron wave vector is $\mathbf{K_0}$, then this can define by-

$$|\boldsymbol{K_0}| = \frac{2\pi}{\lambda}$$

Then, combine the above equation with de Broglie equation -

$$|\boldsymbol{K_0}| sin\theta_a = \left(\frac{2\pi}{a}\right) n$$

In the case of 2D array, another set of diffracted patterns in a series of lines will be generated perpendicularly to the previous one which is shown in Figure 2.20 (b). In this case, constructive interference can be defined in the similar way as-

$$sin\theta_b = \frac{m\lambda}{b}$$

here, b is the path length difference in the second direction and m is an integer.

Alternative representation by electron wave vector for the second direction-

$$|\boldsymbol{K_0}|sin\theta_b = \left(\frac{2\pi}{b}\right)m$$

Thus the diffraction pattern for 2D array shows the intersected points of both 1D reciprocal lattice lines, as shown in Figure 2.20(c). For this 2D case, the reciprocal lattice vector is defined as-

$$\boldsymbol{G} = \left(\frac{2\pi}{a}\right)n + \left(\frac{2\pi}{b}\right)m$$

The condition for the diffracted pattern of 2D surface can define by

$$\boldsymbol{K_0^{||}} = \boldsymbol{K_s^{||}} \pm \boldsymbol{G}$$

$\boldsymbol{K_0^{||}}$and $\boldsymbol{K_s^{||}}$ are the parallel components of incident and scattered electrons.

One simple method to find the number of beams diffracted from the surface at certain electron energy is Ewald sphere construction. In Figure 2.21, the schematic of Ewald sphere construction at different electron energy is shown.

In this case, first the wavelength will be calculated for the certain electron energy by using de Broglie equation-

$$\lambda = \frac{h}{(2mE)^{\frac{1}{2}}}$$

Or,

$$\lambda(\text{Å}) = \sqrt{\frac{150}{E(eV)}}$$

here, E is the electron energy.

Then the magnitude of wave vector for the incoming electrons will be determined by the following equation-

$$|\boldsymbol{K_0}| = \frac{2\pi}{\lambda}$$

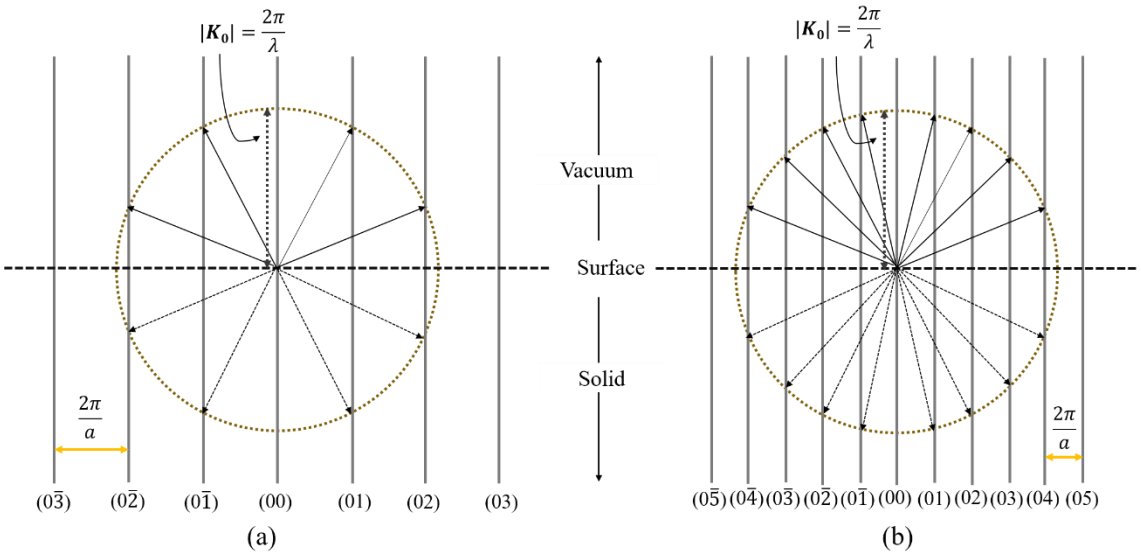

Figure 2.21. Ewald sphere construction for diffraction of the surface with (a) lower and (b) higher electron energy.

From these calculations, when the electron energy is increased, the wavelength will be decreased. Thus, the magnitude of wave vector which the radius of Ewald sphere will be increased. Ewald sphere construction considering these conditions indicates that the diffraction pattern observed at the fluorescent screen is obviously in reciprocal space. This pattern is generated by intersecting the reciprocal lattice rods within the Ewald sphere. Thus, the LEED pattern is dependent on the size of the Ewald sphere. Increasing the radius of Ewald sphere by the increase of electron energy leads the diffraction spots

to come closer to the fixed beam, such as (00) and hence, more diffracted spots become visible.

LEED pattern interpretation

At the beginning of the LEED pattern investigation, the first structural condition of the surface can be understood by visualization. Bright and sharp spots appeared on the LEED pattern with low background indicates that the surface is well-ordered. Due to the presence of defects and crystallographic faults, the spots become broader as well as weaker with changing the background of the pattern. Moreover, no spots in the LEED pattern resemble the amorphous, disordered nature of the surface.

After that, investigation of the geometrical spot positions is the next step. The simplest form of LEED pattern is defined as (1×1), which will be generated from the bulk-like surface structure. Vertical movement of these surface atoms does not change (1×1) pattern. Mostly, the clean metal surfaces, such as, W(110), Mo(110), Pd(111) etc. exhibit (1×1) structure. On the other hand, some unstable clean surfaces shift atoms horizontally to reduce the additional surface energy for becoming stable as well as adsorbing foreign elements on any substrate will produce new ordered structures with larger periodicities compared to the clean surface. These phenomena are known as the formation of 'superstructure'. When a new superstructure is formed, additional spots appeare on LEED pattern known as 'super-spots'. The periodicity of the superstructure in real space can be derived from the LEED pattern in reciprocal space.

First, the reciprocal unit cell vectors of superstructure will be expressed in terms of their substrate lattice vectors in reciprocal space.

$$\boldsymbol{a}_s^* = G_{11}^* \boldsymbol{a}^* + G_{12}^* \boldsymbol{b}^*$$

$$\boldsymbol{b}_s^* = G_{21}^* \boldsymbol{a}^* + G_{22}^* \boldsymbol{b}^*$$

Then, the superstructure is defined by the following reciprocal space matrix-

$$G^* = \begin{pmatrix} G_{11}^* & G_{12}^* \\ G_{21}^* & G_{22}^* \end{pmatrix}$$

This reciprocal space matrix can be converted into the real space matrix by-

$$G = [(G^*)^{-1}]^t = \frac{1}{\det G^*} \begin{pmatrix} G_{22}^* & -G_{21}^* \\ -G_{12}^* & G_{11}^* \end{pmatrix}$$

From this calculation, new periodicity can be determined in real space from the LEED pattern. Two examples of surface structure in real and reciprocal space are shown in Figure 2.22.

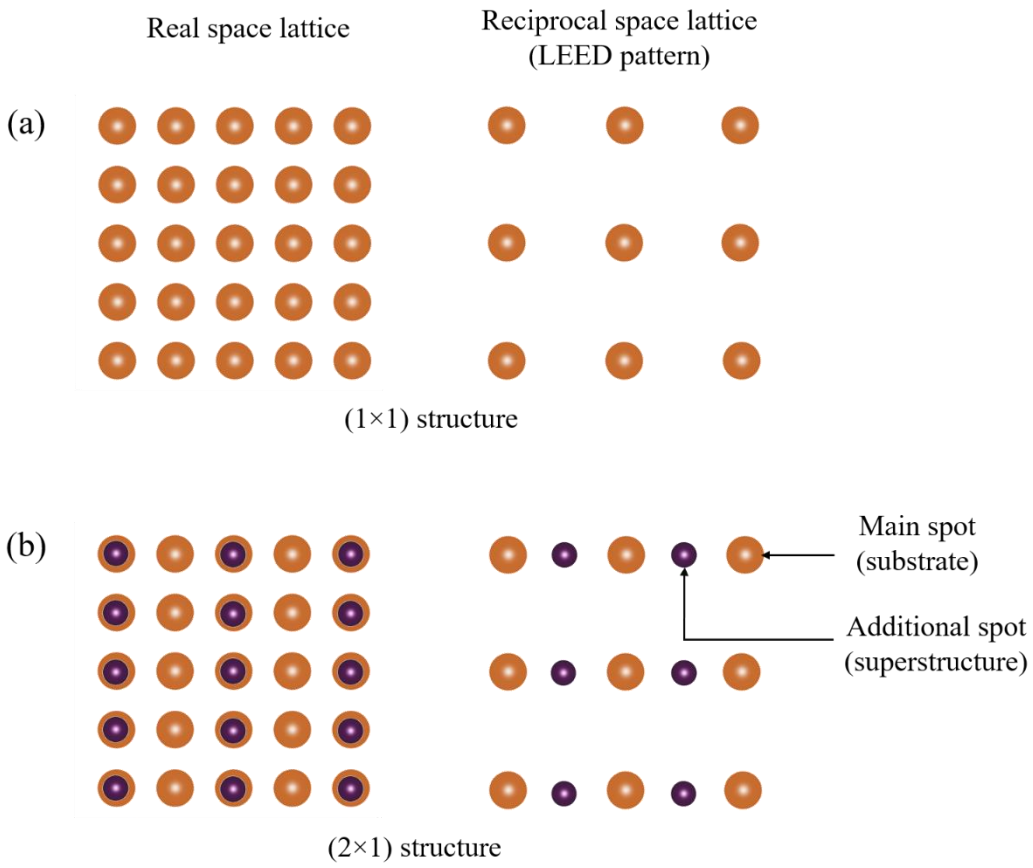

Figure 2.22. Examples of lattices in real and reciprocal space for (a) clean substrate and (b) adsorbate induced substrate.

Quantitative LEED analysis

The arrangement of surface atoms within the unit cell can be evaluated from the spot intensity change with respect to the electron energy which is known as I(E) curve. Figure 2.23 shows an example of spot intensity variation as a function of electron energy. In the LEED system, CCD camera connected with computer is used for data acquisition. Surface structure determination by LEED data cannot be achieved by direct process, instead it requires 'trial and error' process.

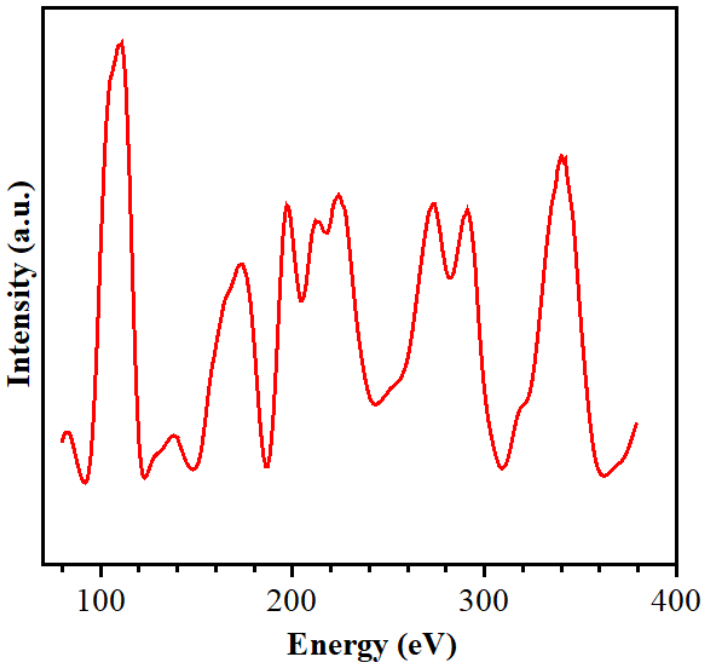

Figure 2.23. LEED I(E) curve of (10) beam for clean W(100) surface.

In this process, the I(E) curves for several number of beams need to be calculated considering the framework of the dynamic theory. This theory considers the high probability of multiple scattering due to the low energy electrons. Then, theoretical I(E) curves are calculated for a good number of model geometries that are consistent with the LEED pattern symmetrically. Theoretical curves are then compared with the experimental ones. This comparison is manifested by a criterion, known as reliability factor or R factor. There are several ways to define this R factor. Zanazzi and Jona [43] proposed a classical form for R factor as-

$$R = \frac{A}{\delta E}\int \omega(E)\left|cI'_{th} - I'_{expt}\right| dE$$

here,

$$c = \frac{\int I_{expt}}{\int I_{th}}$$

$$\omega = \frac{\left|cI''_{th} - I''_{expt}\right|}{\left|I'_{expt}\right| + \epsilon}$$

$$\epsilon = \left|I'_{expt}\right|_{max}$$

and,

$$A = \frac{\delta E}{\left(0.027\int I_{expt}\right)}$$

They claimed that R ≥ 0.2 was considered as better agreement between theoretical and experimental results.

Another R factor proposed by Pendry [44] is the most common one which is called as R_p factor. This factor was derived in the form of logarithmic derivatives-

$$L(E) = \frac{I'}{I}$$

R_p factor is defined as-

$$R = \frac{\sum_g \int (Y_{gth} - Y_{gexpt})^2 \; dE}{\sum_g \int (Y_{gth}^2 + Y_{gexpt}^2)^2 \; dE}$$

here,

$$Y(E) = \frac{L^{-1}}{L^{-2} + V_{oi}^2}$$

The advantageous part of Pendry's R factor is that double derivatives are not required to use, and this can be used in noisy experimental results.

Therefore, determining the surface structure requires significant effort to achieve the minimum R factor, which is the main criteria for the structure. This process of structure determination is shown in Figure 2.24 as a flowchart.

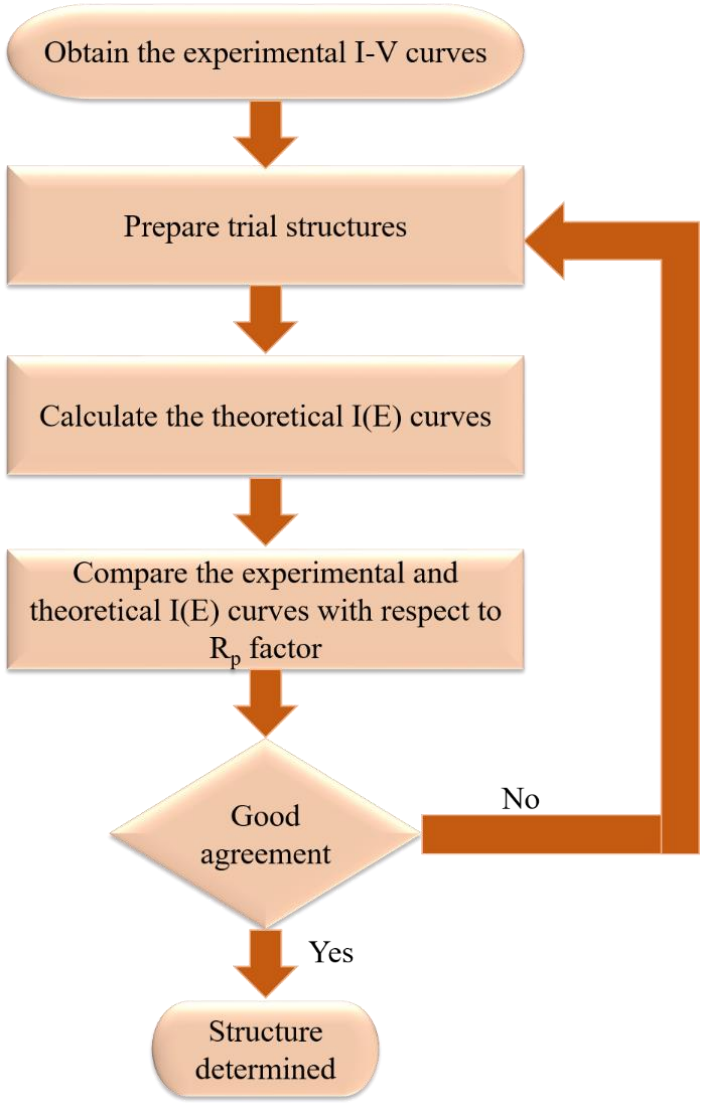

Figure 2.24. Steps required in LEED analysis for surface structure determination.

2.3.2 X-ray photoelectron spectroscopy (XPS)

XPS is known as one of the most reliable techniques for analyzing the chemical properties of surface based on the photoelectric effect. This effect first discovered by Heinrich Rudolf Hertz in 1887 which Albert Einstein was explained in 1905. In mid 1960s, Kai Siegbahn and his research group developed the XPS technique and produced first monochromatic XPS system in 1969. Seigbahn received Nobel prize in 1981 for physics.

XPS measurements are related to photoemission technique. Spectra in XPS are obtained by detecting the ejected electrons from core level of atoms which are irradiated by a beam of X-ray. The process of photoelectron is shown in Figure 2.25, in which an electron of 1s orbital is ejected from the atom.

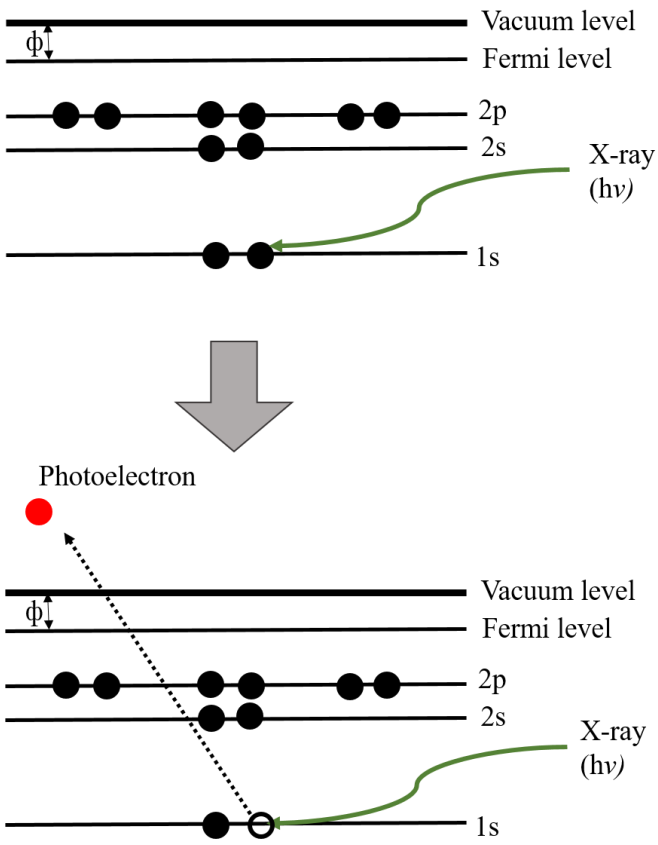

Figure 2.25. Schematic diagram of photoelectron excitation process.

XPS measurements are conducted in UHV condition. The basic components of XPS system are a source of X-ray, electron analyzer, electron detector, lens, sample chamber, manipulator etc. For surface analysis, an X-ray with low energy (Al K_α (1486.7 eV), Mg K_α (1253.6 eV)) is used. When the sample is irradiated by X-ray energy, elastic photoelectrons escaped from the surface are collected by electron analyzer, which has high energy resolution as well as spatial selection for emitted electrons. The kinetic energy of photoelectron is measured by the spectrometer. The kinetic energy is dependent on the photon energy of X-ray. However, for any specific element, the binding energy will remain the same, which is the main parameter to identify the chemical elements. Schematic representation of XPS system is shown in Figure 2.26.

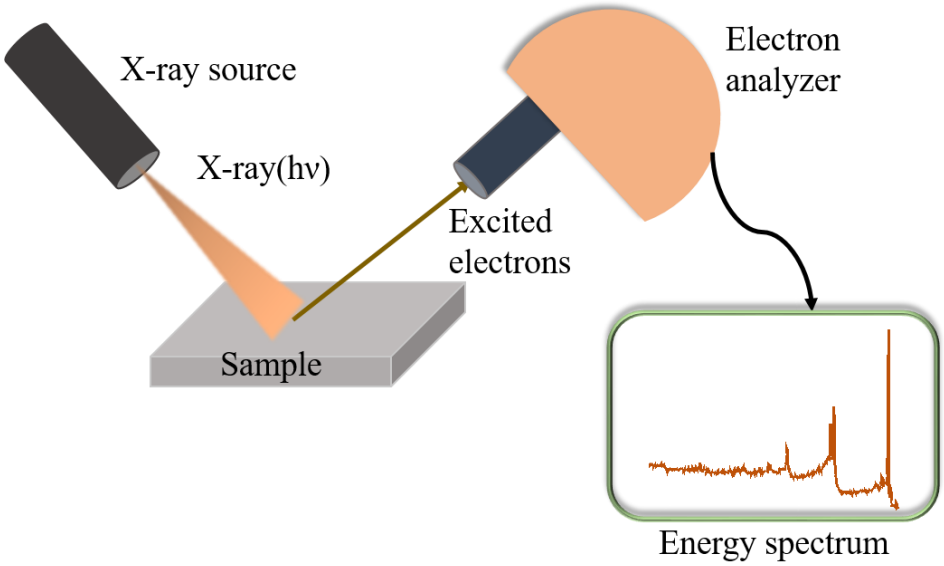

Figure 2.26. Representation of XPS system with its basic components.

The relation between binding energy and kinetic energy in XPS system is-

$$E_B = h\vartheta - E_k - \varphi$$

here, E_B = Binding energy, E_k = Electron kinetic energy, hν = X-ray photon energy and φ = Work function.

The obtained XPS spectrum will generate the electronic structure of a material quite accurately if the binding energy of the electrons of that material remains lower than the incident photon energy. An XPS spectrum superimposed on a schematic of electron orbitals is shown in Figure 2.27. The detected photoelectrons which are escaped without losing any energy contribute in the characteristic peaks of the spectrum. The inelastically scattered electrons which lose energy due to collision contribute to the background of the spectrum.

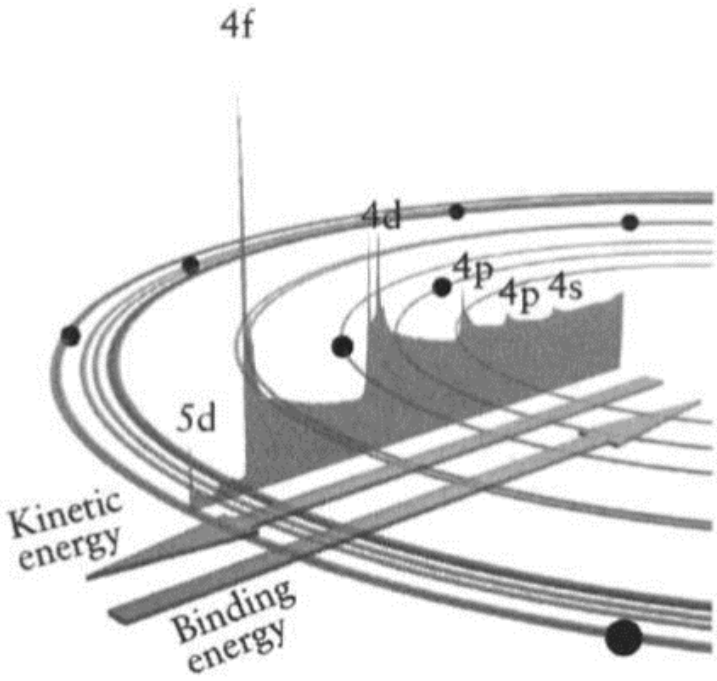

Figure 2.27. Photoelectron spectrum showing the way electrons are escaping from bulk [Copied from ref [45]*].*

XPS measurements provide more information except identifying the elements. Intensity of peak will give the idea about the quantity of a certain element as the peak area is proportional to the number of atoms for that element. More, peak position reveals the chemical state of a specific material. The binding energy of a pure element is fixed. When this element makes bond with each other or different material, then charge transfer will occur. This phenomenon leads to change the peak position of that element from the original position.

Therefore, XPS is a fundamental tool for characterizing chemical properties of different surfaces. Chemical composition, as well as presence of contaminants, can be identified by XPS.

2.3.3 Scanning tunneling microscopy (STM)

STM is a powerful tool for surface imaging at the atomic level which was invented in 1981 by Heinrich Rohrer and Gerd Bining. For the recognition of STM technique development, they were awarded Nobel prize in 1986. STM can image the surface of metal, semiconductor or any conductive materials through tunneling effect by using a sharp conducting tip which is held over the surface at a distance of few angstroms.

The main principle for STM is the tunneling effect. According to the wave nature, electrons of surface atoms are comparatively lightly bonded with the nucleons than the electrons of bulk atoms. Moreover, the electron density does not become zero in space at the outer side of the surface; it exponentially decreases with the increase of distance between electron and surface. Thus, if a metal tip brings closer to any conductive material within few angstroms, then electron clouds generated from both sides will overlap with each other. Thereby, a tunneling current will be generated if a small voltage is applied between tip and substrate.

The dependency of tunneling current, I, on the distance, Z, is expressed as-

$$I \propto e^{-2Z[2m/h^2(<\varphi>-e|V|/2)]^{\frac{1}{2}}}$$

here, h is plank constant, m is the mass of electron, e is electron charge, φ is work function and V is bias voltage.

For simplicity, let,

$$k_0 = [2m/h^2(< \varphi > -e|V|/2)]^{\frac{1}{2}}$$

then,

$$I = e^{-2k_0 Z}$$

The above equation shows that increase in distance between tip and sample will decrease the tunneling current.

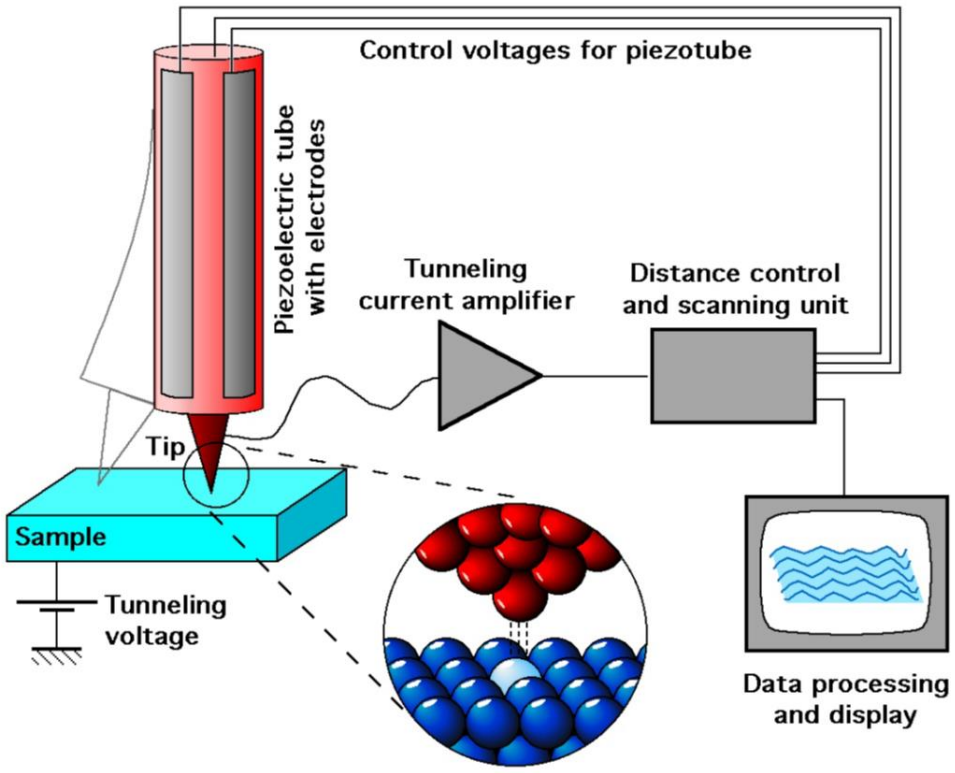

Figure 2.28. Schematic view of STM system with its basic components [Copied from ref [46]].

In STM, the basic components are the tip, piezoelectrically controlled scanner, sample to tip approach mechanism. First, the metallic tip, which is attached to the three piezoelectric transducers, is approached closer to the sample within few angstroms for scanning in the X-Y plane of the sample, and the magnitude of tunneling current is recorded, which is

dependent on the applied voltage and the distance between tip to sample. Then, the tunneling current is converted to voltage by current amplifier, and the measured voltage is compared with the initial condition to control the piezoelectric device using a feedback circuit. Peizo materials control the tip movement in three dimensions (X, Y and Z) to scan the entire sample. In Figure 2.28, a schematic of STM process is shown. There are two modes for STM process, constant current mode and constant height mode.

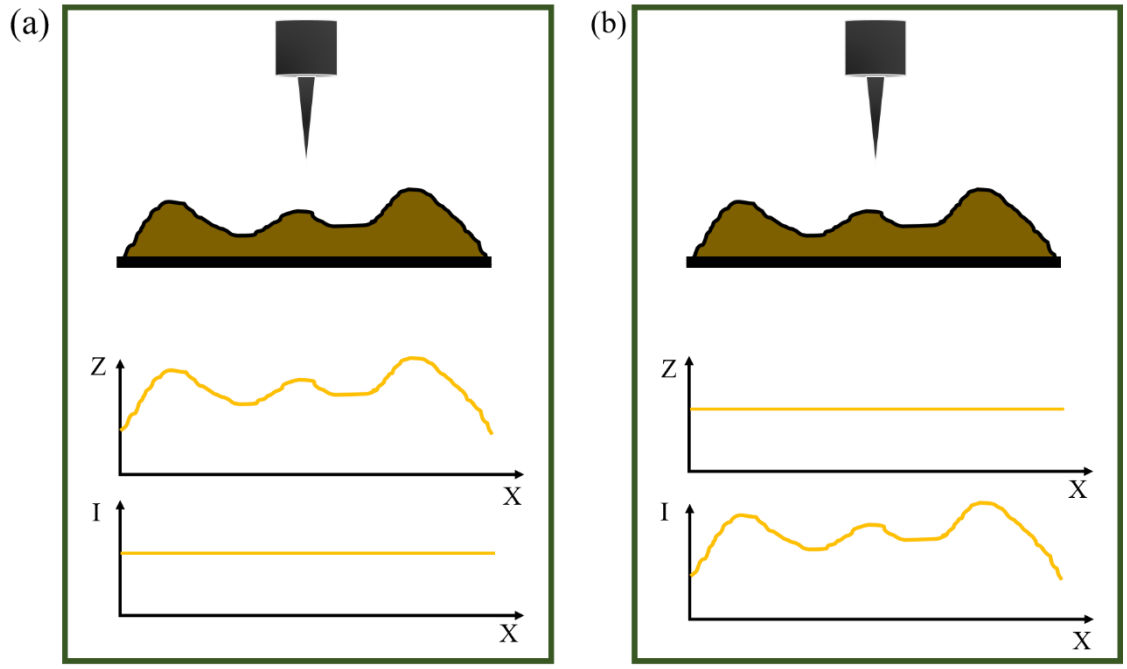

Figure 2.29. STM imaging in two different modes. (a) constant current mode and (b) constant height mode.

In constant current mode, the tunneling current is fixed, which is known as set point. Then, the measured tunneling current from each position is compared with the set point. If this value is higher than that target value, then the tip is moved backward from the sample using piezoelectric transducer to maintain the tunneling current fixed. Conversely, the tip will move towards the sample if the tunneling current drops below the target value. On the other hand, tip position is fixed in constant height mode. In this case, tunneling current is measured from the entire sample by keeping the tip in certain position. This mode of STM is useful only for smooth surface. Rough surface containing large particles

can damage the tip as well as the surface of the sample can also be affected. In Figure 2.29, schematic of constant current and constant height mode for STM are depicted.

References

[1] M. Kabiruzzaman, R. Ahmed, T. Nakagawa, S. Mizuno, Investigation of c(2×2) phase of Pb and Bi coadsorption on Cu(001) by low energy electron diffraction, Evergreen. 4 (2017) 10–15. https://doi.org/10.5109/1808306.

[2] S. Mizuno, H. Tochihara, T. Kawamura, Determination of the c(2 × 2) structure formed on Cu(001) upon Li adsorption: a low-energy electron diffraction analysis, Surf. Sci. 293 (1993) 239–245. https://doi.org/10.1016/0039-6028(93)90317-D.

[3] K. Oura, M. Katayama, A. V. Zotov, V.G. Lifshits, A.A. Saranin, Atomic structure of clean surfaces, Surf. Sci. (2003) 171–194. https://doi.org/10.1007/978-3-662-05179-5_8.

[4] D.L. Adams, H.B. Nielsen, M.A.Van Hove, A. Ignatiev, LEED study of the Pt(110)-(1×2) surface, Surf. Sci. 104 (1981) 47–62. https://doi.org/10.1016/0167-2584(81)90182-1

[5] W. Moritz, D. Wolf, Structure determination of the reconstructed Au(110) surface, Surf. Sci. 88 (1979) L29–L34. https://doi.org/10.1016/0039-6028(79)90093-1.

[6] R. Koch, M. Borbonus, O. Haase, K.H. Rieder, Reconstruction behaviour of fcc(110) transition metal surfaces and their vicinals, Appl. Phys. A Solids Surfaces. 55 (1992) 417–429. https://doi.org/10.1007/BF00348329.

[7] C.A. Chan, M.A. Van Hove, W.H. Weinberg, E.D. Williams, Structural study of the reconstructed Ir(110)-(1×2) surface by low-energy electron diffraction, Solid State Commun. 30 (1979) 47–49. https://doi.org/10.1016/0038-1098(79)91130-X

[8] R.A. Barker and P.J. Estrup, Structural models of the reconstructed W{001} surface, Solid State Commun. 32 (1978) 147–156. https://doi.org/10.1016/0038-1098(78)90079-0.

[9] K. Oura, M. Katayama, A. V. Zotov, V.G. Lifshits, A.A. Saranin, Surface Science, Springer Berlin Heidelberg, Berlin, Heidelberg (2003) https://doi.org/10.1007/978-3-662-05179-5.

[10] J.H. Petersen, C. Søndergård, S. V. Hoffmann, A. Mikkelsen, D.L. Adams, Surface alloy formation by adsorption of Li on Al(100): Studied by high-resolution core-level spectroscopy and low energy electron diffraction, Surf. Sci. 437 (1999) 317–329. https://doi.org/10.1016/S0039-6028(99)00621-4.

[11] D. Fick, H. Kleine, M. Eckhardt, H.J. Jansch, Adsorption of Li on a Si (100)-2×1 surface, Surf. Sci. 323 (1995) 51–56. https://doi.org/10.1016/0039-

6028(94)00629-6

[12] G. Schmidt, H. Zagel, H. Landskron, K. Heinz, K. Müller, J.B. Pendry, The clean and H-induced reconstruction of W(100) studied by LEED at slanting primary bean incidence, Surf. Sci. 271 (1992) 416–426. https://doi.org/10.1016/0039-6028(92)90905-L.

[13] R.L. Park, H.H. Madden, Annealing changes on the (100) surface of palladium and their effect on CO adsorption, Surf. Sci. 11 (1968) 188–202. https://doi.org/10.1016/0039-6028(68)90066-6.

[14] E.A. Wood, Vocabulary of surface crystallography, J. Appl. Phys. 35 (1964) 1306–1312. https://doi.org/10.1063/1.1713610.

[15] H. Davy, An account of some new analytical researches on the nature of certain bodies, particularly the alkalies, phosphorus, sulphur, carbonaceous matter, and the acids hitherto undecomposed: with some general observations on chemical theory, Philos. Trans. R. Soc. London. 15 (1808) 39–104. https://doi.org/10.7248/jjrhi.50.418.

[16] A.W. Laubengayer, D.T. Hurd, A.E. Newkirk, J.L. Hoard, Boron. I. preparation and properties of pure crystalline boron, J. Am. Chem. Soc. 65 (1943) 1924–1931. https://doi.org/10.1021/ja01250a036.

[17] Z. Zhang, Y. Yang, E.S. Penev, B.I. Yakobson, Elasticity, flexibility, and ideal strength of borophenes, Adv. Funct. Mater. 27 (2017) 1605059. https://doi.org/10.1002/adfm.201605059.

[18] X. Sun, X. Liu, J. Yin, J. Yu, Y. Li, Y. Hang, X. Zhou, M. Yu, J. Li, G. Tai, W. Guo, Two-dimensional boron crystals: structural stability, tunable properties, fabrications and applications, Adv. Funct. Mater. 27 (2017) 1603300. https://doi.org/10.1002/adfm.201603300.

[19] B.F. Decker, J.S. Kasper, The crystal structure of a simple rhombohedral form of boron, Acta Crystallogr. 12 (1959) 503–506. https://doi.org/10.1107/s0365110x59001529.

[20] L.V. McCarty, J.S. Kasper, F.H. Horn, B.F. Decker, A.E. Newkirk, New crystalline modification of boron, J. Am. Chem. Soc. 80 (1958) 2592. https://doi.org/10.1021/ja01543a066

[21] D.E. Sands, J.L. Hoard, Rhombohedral elemental boron, J. Am. Chem. Soc. 79 (1957) 5582–5583. https://doi.org/10.1021/ja01577a072

[22] I. Boustani, Systematic ab initio investigation of bare boron clusters: Determination of the geometry and electronic structures of B_n (n=2-14), Phys. Rev. 55 (1997) 16426–16438. https://doi.org/10.1103/PhysRevB.55.16426.

[23] J.M. Mercero, A.I. Boldyrev, G. Merino, J.M. Ugalde, Recent developments and future prospects of all-metal aromatic compounds, Chem. Soc. Rev. 44 (2015) 6519–6534. https://doi.org/10.1039/c5cs00341e.

[24] A.I. Boldyrev, L.S. Wang, Beyond organic chemistry: Aromaticity in atomic clusters, Phys. Chem. Chem. Phys. 18 (2016) 11589–11605. https://doi.org/10.1039/c5cp07465g.

[25] L. Hanley, J.L. Whitten, S.L. Anderson, Collision-induced dissociation and ab initio studies of boron cluster ions: determination of structures and stabilities, J. Phys. Chem. 92 (1988) 5803–5812. https://doi.org/10.1021/j100368a090

[26] H.J. Zhai, L.S. Wang, A.N. Alexandrova, A.I. Boldyrev, Electronic structure and chemical bonding of B5- and B5 by photoelectron spectroscopy and ab initio calculations, J. Chem. Phys. 117 (2002) 7917–7924. https://doi.org/10.1063/1.1511184.

[27] H.J. Zhai, A.N. Alexandrova, K.A. Birch, A.I. Boldyrev, L.S. Wang, Hepta- and Octacoordinate boron in molecular wheels of eight- and nine-atom boron clusters: observation and confirmation, Angew. Chemie - Int. Ed. 42 (2003) 6004–6008. https://doi.org/10.1002/anie.200351874.

[28] H.-J. Zhai, B. Kiran, J. Li, L.-S. Wang, Hydrocarbon analogues of boron clusters — planarity, aromaticity and antiaromaticity, Nat. Mater. 2 (2003) 827–833. https://doi.org/10.1038/nmat1012.

[29] B. Kiran, S. Bulusu, H.J. Zhai, S. Yoo, X.C. Zeng, L.S. Wang, Planar-to-tubular structural transition in boron clusters: B_{20} as the embryo of single-walled boron nanotubes, Proc. Natl. Acad. Sci. U. S. A. 102 (2005) 961–964. https://doi.org/10.1073/pnas.0408132102.

[30] A.P. Sergeeva, Z.A. Piazza, C. Romanescu, W.L. Li, A.I. Boldyrev, L.S. Wang, B_{22}- and B_{23}-: All-boron analogues of anthracene and phenanthrene, J. Am. Chem. Soc. 134 (2012) 18065–18073. https://doi.org/10.1021/ja307605t.

[31] Z.A. Piazza, H. Hu, W. Li, Y. Zhao, J. Li, L. Wang, Planar hexagonal B_{36} as a potential basis for extended single-atom layer boron sheets, Nat. Commun. (2014). https://doi.org/10.1038/ncomms4113.

[32] S. Xie, Y. Wang, X. Li, Flat Boron: A new cousin of graphene, Adv. Mater. 31

(2019) 1900392. https://doi.org/10.1002/adma.201900392.

[33] N. Gonzalez Szwacki, A. Sadrzadeh, B.I. Yakobson, B_{80} fullerene: An ab initio prediction of geometry, stability, and electronic structure, Phys. Rev. Lett. 98 (2007) 1–4. https://doi.org/10.1103/PhysRevLett.98.166804.

[34] H. Tang, S. Ismail-Beigi, Novel precursors for boron nanotubes: The competition of two-center and three-center bonding in boron sheets, Phys. Rev. Lett. 99 (2007) 115501. https://doi.org/10.1103/PhysRevLett.99.115501.

[35] Y. Liu, E.S. Penev, B.I. Yakobson, Probing the synthesis of two-dimensional boron by first-principles computations, Angew. Chemie. 125 (2013) 3238–3241. https://doi.org/10.1002/ange.201207972.

[36] A.J. Mannix, X.F. Zhou, B. Kiraly, J.D. Wood, D. Alducin, B.D. Myers, X. Liu, B.L. Fisher, U. Santiago, J.R. Guest, M.J. Yacaman, A. Ponce, A.R. Oganov, M.C. Hersam, N.P. Guisinger, Synthesis of borophenes: Anisotropic, two-dimensional boron polymorphs, Science. 350 (2015) 1513–1516. https://doi.org/10.1126/Xscience.aad1080.

[37] F. Albert Cotton, Transition metal, Encycl. Br. (2020). https://www.britannica.com/science/transition-metal.

[38] T.E. of E. Britannica, Tungsten, Encycl. Br. (2021). https://www.britannica.com/science/tungsten-chemical-element.

[39] T.E. of E. Britannica, Molybdenum, Encycl. Br. (2016). https://www.britannica.com/science/molybdenum.

[40] G. Held, Low-energy electron diffraction: crystallography of surfaces and interfaces, Methods Phys. Chem. 1 (2012) 625–642. https://doi.org/10.1002/9783527636839.ch20.

[41] J. Wang, Low energy electron diffraction studies of transition metal oxide surfaces and films, Metal Oxide Surfaces. 4 (2005) 7-22.

[42] G. Attard, C. Barnes, Surfaces, Oxford University Press. (1998).

[43] E. Zanazzi, F. Jona, A reliability factor for surface structure determinations by low-energy electron diffraction, Surf. Sci. 62 (1977) 61–80. https://doi.org/10.1016/0039-6028(77)90428-9.

[44] J.B. Pendry, Reliability factors for LEED calculations, J. Phys. C Solid State Phys. 13 (1980) 937–944. https://doi.org/10.1088/0022-3719/13/5/024.

[45] J.F. Watts, J. Wolstenholme, An introduction to surface analysis by XPS and AES, John Wiley Sons, (2003).

[46] M. Gruber, Electronic and magnetic properties of hybrid interfaces: From single molecules to ultra-thin molecular films on metallic substrates, (2014). https://doi.org/10.5445 / IR / 1000045289

CHAPTER 3:
B
ADSORPTION
ON W(100)

3.1 Introduction

The lightest metalloid, B, positioned in group 13 in the periodic table, is a unique element because of its complex structure and extraordinary chemical and physical properties, including super hardness, high melting point, and low density [1,2]. Furthermore, B forms multi-center-two-electrons bonds because of the electron deficiency in its outer shell [1–5]. Due to these bonding configurations, B has 16 allotropic structures composed of B_{12} icosahedra, small B clusters, and supericosahedra [5–9]. Despite that, small clusters of B can form simple planar or quasiplanar structures, which are different from their 3D bulk structures [10]. The formation of planner clusters indicates that boron may exhibit many characteristics of its neighboring element, carbon [11]. However, fabrication of monolayer B sheet took great research efforts compared to 2D sp^2 hybridized graphene due to the electron-deficient nature of B atom, making its structures fluxional [12]. Recently, B sheet fabrication has attracted much attention because of its predicted extraordinary properties, such as high mechanical strength and flexibility, metallicity, optical transparency etc. First successful experimental synthesis of 2D B sheet on Ag(111) surface leads to conduct numerous researches to understand the B growth and interaction of B with different substrates. It was found that various phases of 2D boron sheet formed on several other substrates, such as Cu(111), Au(111), Al(111), Ir(111) [12–16] and the growth of 2D boron sheet as well as its structural phase were dependent on the surface faces of substrates [17–19].

Recently, investigation of B interaction with refractory metal surfaces has drawn attention for determining B structure on these metal substrates. It was reported theoretically earlier that a new phase of borophene named as, π phase, could be formed on W(110) surface [20]. Moreover, in previous works, Tucker investigated the interaction of B with the different crystal surfaces of W substrate by LEED [21]. Lu et al., determined the adsorption-diffusion phenomena of B with three low index W surfaces by first principles calculations and found that hollow site was the most stable position for B adsorption on W surfaces, and the energy barrier of B diffusion was largest for W(100) surface compared to the other surfaces [22]. Among other refractory metal surfaces, W(100) is one of the most extensively studied refractory metal surfaces because of its surface

reconstruction below room temperature [23]. So far, surface reconstruction of W(100) surface after inducing foreign adsorbates, including several metals and molecules, was conducted by LEED [24,25]. However, extensive study of reconstructed W(100) surface due to metalloid adsorption is not reported yet.

In this study, we investigated the B induced superstructure on W(100) in detail. An ordered structure, W(100) c(2×2)-B formed after annealing the substrate at 1200 K. The detailed structural analysis by LEED provided the information about B atoms arrangement on the W(100) surface with the bonding interaction between B and W atoms as well as the surface relaxation of W atoms. XPS analysis for W(100) c(2×2)-B revealed noticeable charge transfer from W to B. Thereby, the analyses of structural and chemical properties come up with the understanding of structure and interactivity of B with W(100) surface.

3.2 Experiment and calculation

The experiments were conducted in UHV chambers for STM, LEED, and XPS separately. The STM experiments were performed at low temperature (77K) with PtIr tip. The LEED chamber having a base pressure around 2×10^{-8} Pa was equipped with four grid LEED system and LEED I(E) measurement system. To determine the chemical interactions of B/W(100) by XPS, the measurements were carried out by using PHOIBOS100 analyzer in UHV with a base pressure of $\sim2\times10^{-10}$ Torr and a non-monochromatic Mg K_α X-ray with a photon energy ($h\upsilon$) of 1253.6 eV was used as X-ray source. Both XPS and STM chambers were equipped with LEED apparatus for sample preparation.

To prepare the sample, W(100) crystal was cleaned first by repeated cycles of annealing approximately at 1500 K in oxygen atmosphere with a pressure around 6×10^{-6} Pa followed by a flash at ~2100 K. The cleanliness of sample was confirmed by cooling down the sample using liquid nitrogen. A sharp with low background c(2×2) LEED pattern was observed due to the surface reconstruction of clean W(100) at 120K confirming the

cleanliness of sample. Afterwards, the substrate was brought back to room temperature first and then, highly pure B was evaporated from a carbon crucible on the cleaned W(100) surface by e-beam evaporator (7.55A, 2 kV, 50 mA) with a deposition rate of ~0.1ML/min which was monitored by quartz crystal microbalance (QCM). After the growth of B on W(100), the substrate was annealed at high temperature. The growth condition of B and annealing temperature were varied. Therefore, sharp c(2×2) LEED pattern was obtained for B deposition followed by annealing the substrate at high temperature. After the preparation of sample, LEED chamber was cooled down to 120 K, and LEED patterns were observed and recorded at a temperature ~120K using a digital charge-coupled device camera with a computer-controlled data acquisition system [26,27].

LEED intensity-energy curves, I(E), were obtained for incident energy range from 70 eV to 500 eV. For determining the atomic structure, Barbieri-Van Hove symmetrized automated tensor LEED package was used [28]. 13 phase shifts (L_{max} = 12) were used for calculating atomic scattering factors. The imaginary part of inner potential (V_{oi}) was fixed at -5.0 eV, while the real part of the potential was varied. Optimization of the best fitted model through the best agreement between theoretical and experimental I(E) curves was carried out by minimizing the Pendry's reliability factor (R_p). The error bars on the structural parameters were obtained from the variance of R_p, $\Delta R = R_{min}\left(\frac{8|V_{oi}|}{\Delta E}\right)^{\frac{1}{2}}$; where R_{min} is the minimum value of R_p and ΔE is the total energy range of the experimental $I(E)$ curves [29].

Density functional theory (DFT) calculations were performed using a projector-augmented wave pseudopotential with Perdew-Burke-Ernzerhof (PBE) and plane-wave basis set with an energy cutoff at 650 eV [30,31]. The calculation cell contained a B film on a five-layer c(2×2)-W(100). The surface Brillouin zone was sampled by a 12×12×1 k-mesh [32]. The lattice constant of W used in the calculations was 3.186 Å, 0.7% larger than the experimental value, and a vacuum region was set as 20 Å. All structures were fully relaxed until the force on each atom was less than 0.05 eV/Å, and the bottom layer of W atoms was fixed. All calculations were performed with the Quantum ESPRESSO

package [33,34], and simulated STM images were plotted using critic2 with the constant current mode [35].

3.3 Results and discussion

3.3.1 Low energy electron diffraction(LEED)

To analyze the surface structure for B induced W(100) surface, the LEED patterns for clean W(100) surface, as deposited B on W(100) surface, and B covered W(100) surface after annealing were observed.

Clean W(100) surface

A clean W(100) surface showed p(1×1) periodicity above 300 K temperature, which exhibited a reversible phase transition to c(2×2) periodicity at the temperature lower than 300 K. LEED patterns for this phase transition from (1×1) to c(2×2) with temperature for clean W(100) are shown in Figure 3.1.

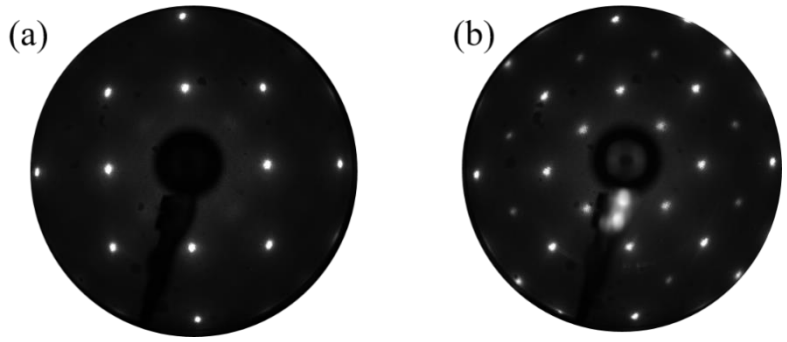

Figure 3.1. LEED patterns of W(100) surface taken at electron energy of 120 eV (a) clean W(100) surface at high temperature showing p(1×1) periodicity and (b) reconstructed clean W(100) surface at low temperature indicating the phase transition to c(2×2) structure.

B adsorbed W(100) surface

The adsorption of B on W(100) at room temperature generated obscured p(1×1) LEED pattern with a diffuse background over the pattern. A sharp c(2×2) superstructure was obtained after annealing the substrate at high temperature. LEED patterns of clean W(100) substrate, B deposited on W(100) as well as sharp c(2×2) pattern after annealing the substrate are shown in Figure 3.2.

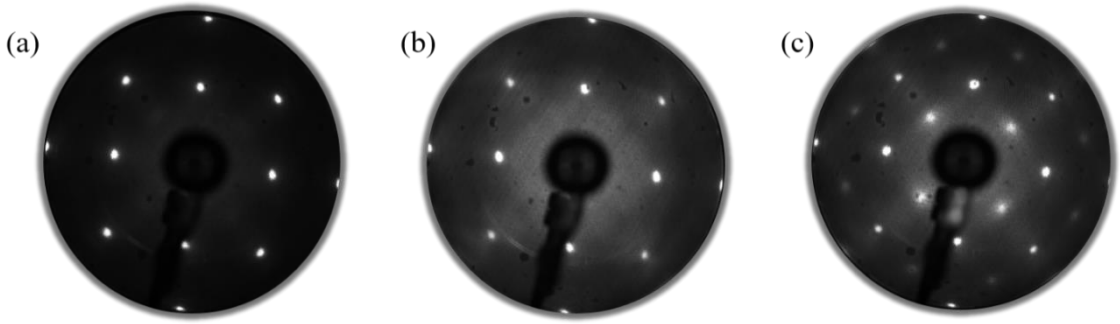

Figure 3.2. LEED patterns of W(100) surface taken at electron energy of 120 eV for (a) clean W(100) surface, (b) B deposited W(100) for 10 min at room temperature and (c) subsequently annealed the sample.

The growth of B was strongly dependent on the deposition conditions. If the substrate was kept in room temperature during deposition, then LEED pattern exhibited p(1×1) structure with obscure background and the background became more obscure with the increase of deposition time (Figure 3.3(a,b)). On the other hand, new weak spots appeared on LEED pattern if the substrate kept at high temperature (700 K) during deposition (Figure 3.3(c,d)). Hence the substrate temperature has an impact on the growth of B on W(100) surface. Moreover, deposition time also acted as an important to be considered. When B was deposited for different times, annealing temperature increased with the increase of deposition time. For longer deposition time, diffracted spots of W atoms become weaker in LEED pattern, indicating the amount of B was high on surface. Due to this reason, annealing temperature increased to obtain sharp c(2×2) structure. No other superstructure was found be formed on the surface, which was verified by changing the growth condition and annealing temperature very precisely. The reason behind not

forming other structures on W(100) surface is the preference of B atoms to be diffused into the bulk. Thereby, increasing B concentration over the substrate requires higher annealing temperature to diffuse the additional B atoms which scattered over the surface randomly into the bulk. Variation of B deposition time from 5 to 30 min, we observed the increase of annealing temperature from 800 K to 1350 K to get the clear c(2×2) structure, which are shown in Figure 3.4.

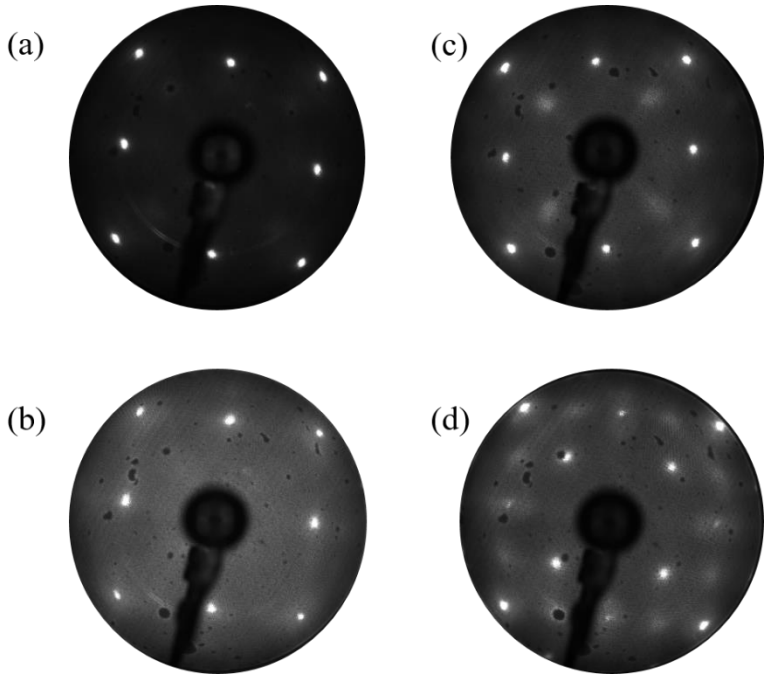

Figure 3.3. LEED patterns of B/W(100) at electron energy of 80 eV for different deposition conditions; B deposited for (a) 10 min and (b) 30 min at room temperature, and (c) 10 min and (d) 30 min at high temperature (700 K).

The c(2×2) superstructures formed upon B deposition on W(100) at different conditions might be occurred from the different or similar B orientations over the surface keeping the unit cell size same. To understand this, LEED I(E) curves for four different conditions were compared with each other. In Figure 3.5, a comparison in LEED I(E) curves for a fraction order beam, (0.5,0.5), is shown; which shows that the peak shape for all cases is almost similar with having a discrepancy in peak intensity. The change in peak intensity with slide peak shifting occurs due to the sample position with respect to the LEED

camera. As the peak shape is nearly same, this indicates the c(2×2) structure for B/W(100) possesses similar B orientation on surface for all conditions.

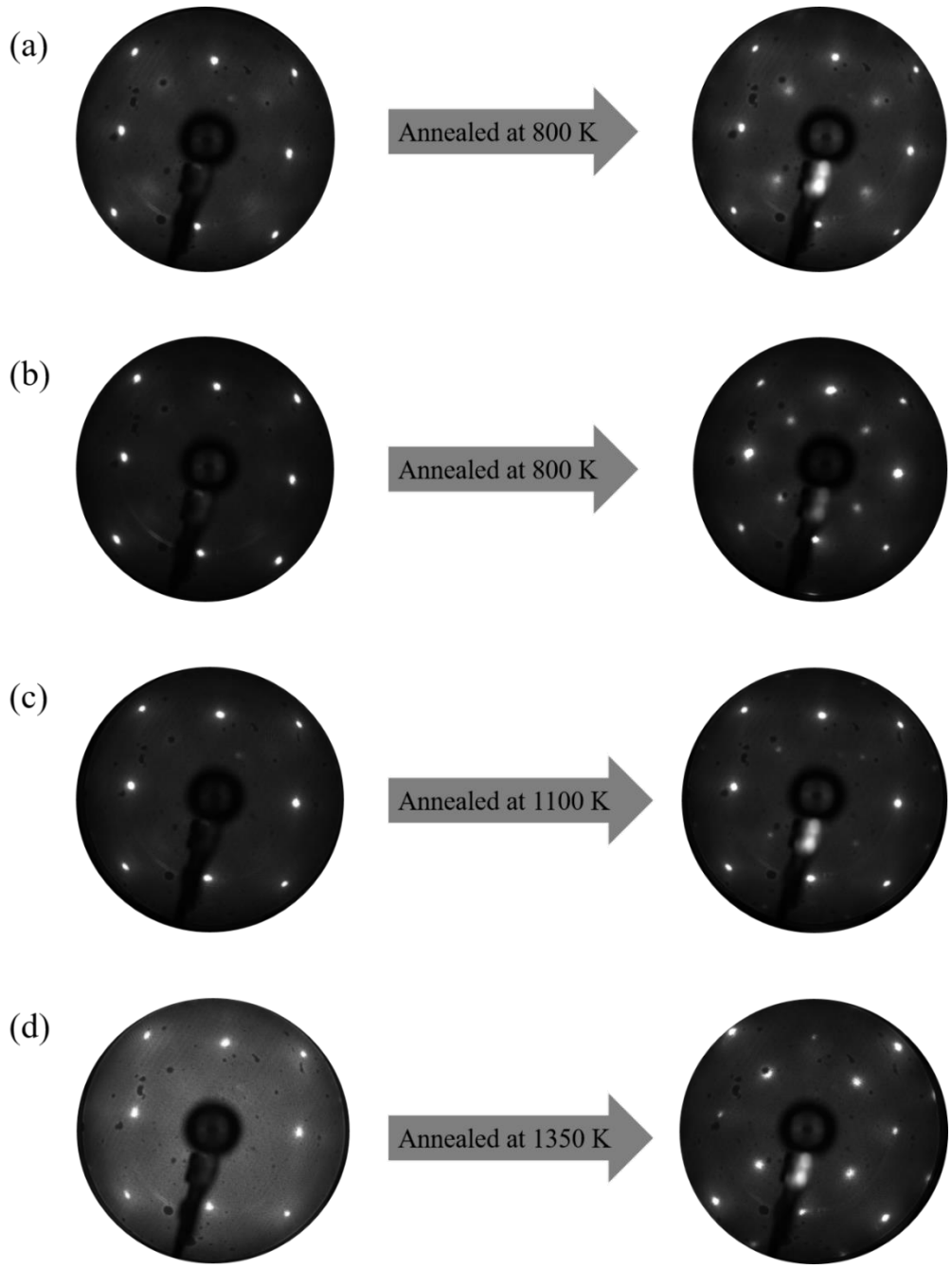

Figure 3.4. LEED patterns of B/W(100) at electron energy of 80 eV, B deposited at room temperature (a) for 5 min and subsequently annealed at 800 K, (b) for 10 min and subsequently annealed at 800 K, (c) for 20 min and subsequently annealed at 1100 K, and (d) for 30 min and subsequently annealed at 1350 K.

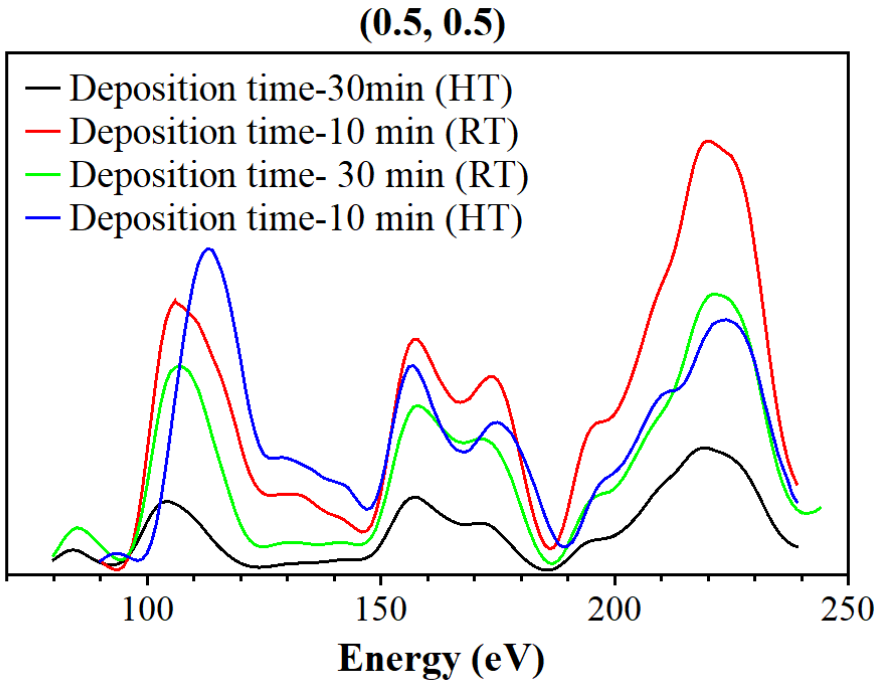

Figure 3.5. Peak intensities of (0.5,0.5) beam for c(2×2) superstructure formed at different deposition conditions.[HT- High temperature, RT- Room temperature]

Comparison of c(2×2) structures for clean and B/W(100) surface

It is quite important to understand the difference between c(2×2) structures for clean W(100) and B/W(100) surface. For clean W(100) surface, c(2×2) structure appeared at below room temperature and this structure reversed back to the initial p(1×1) structure when temperature increased above 300 K. However, c(2×2) structure for B induced W(100) surface was stable in the temperature below or above room temperature. This discrepancy indicates the existence of structural differences in clean W(100) and B/W(100) surface. Moreover, the comparison between LEED I(E) curves of these two structures also shows the presence of dissimilarities in fractional order beams, which is shown in Figure 3.6. Therefore, the surface structure for W(100) c(2×2)-B is different from the clean one.

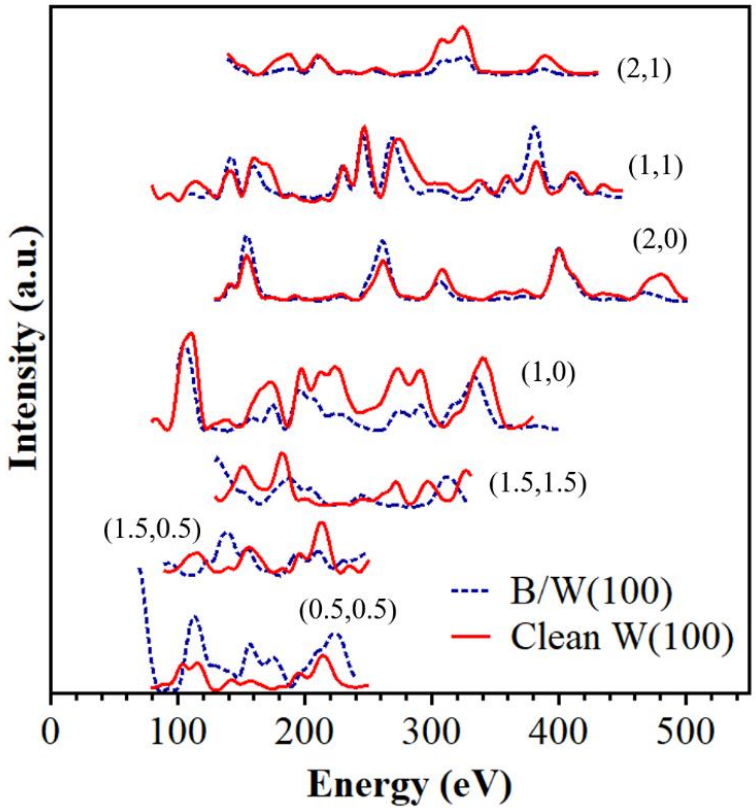

Figure 3.6. Comparison between LEED I(E) spectra for c(2×2) structures of clean W(100) surface (red line) and B/W(100) surface (blue dashed line).

LEED I(E) analysis for W(100) c(2×2)-B structure

To determine W(100) c(2×2)-B structure, we have employed LEED I(E) analysis. The intensities of non-equivalent beam spots of c(2×2) pattern were recorded for structural analysis. To determine the structural model of W(100) c(2×2)-B, 50 models were analyzed by varying the B coverage from 0.5 to 6.5 ML. These optimized 50 models with their corresponding R_p factor are shown in Figures 3.7 and 3.8, respectively. Among these models, a model with p4mm symmetry showed the lowest R_p factor of 0.23 in which B atoms were positioned at one of the high symmetry sites, four-fold hollow site, for W(100) surface.

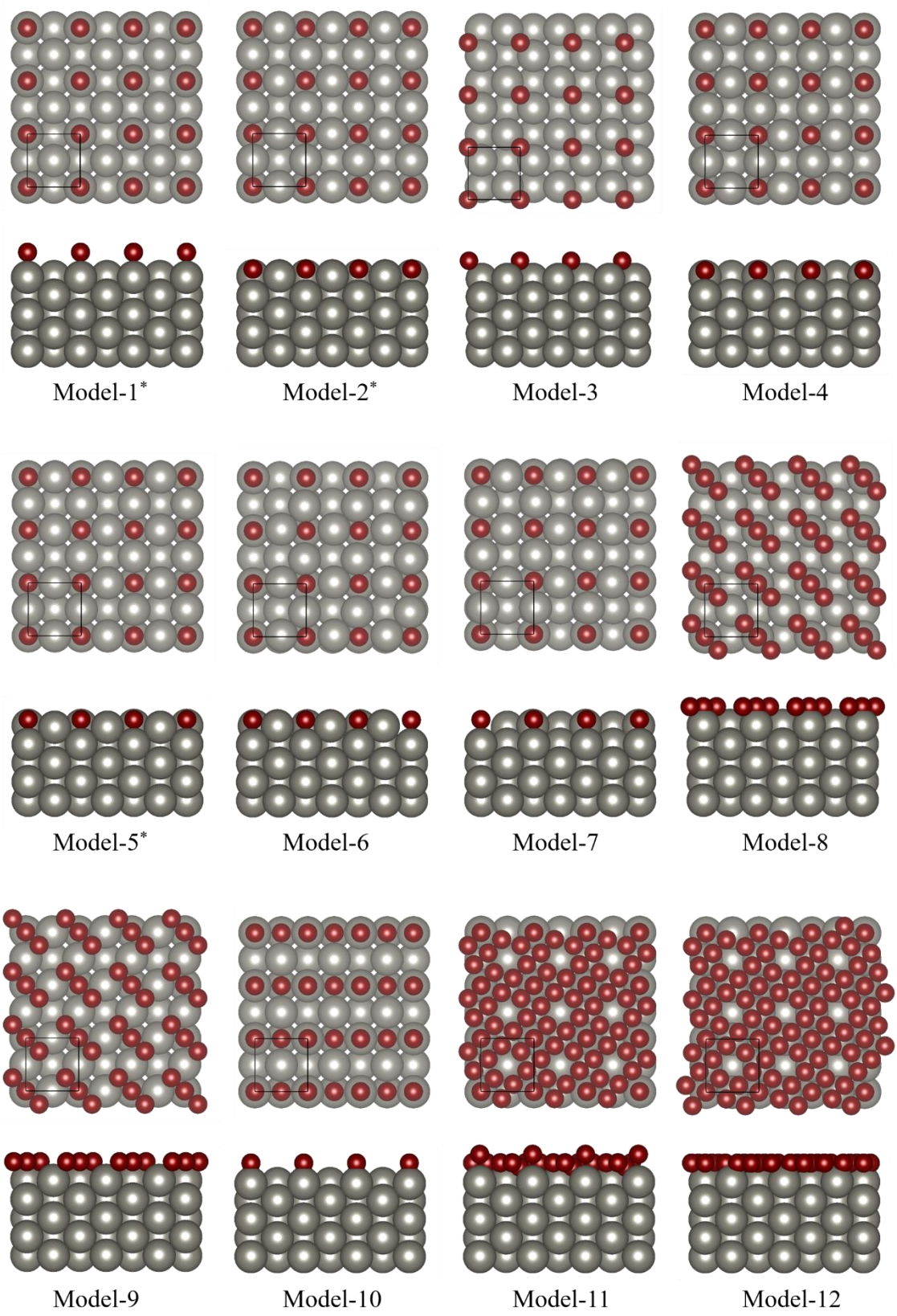
Model-1*
Model-2*
Model-3
Model-4
Model-5*
Model-6
Model-7
Model-8
Model-9
Model-10
Model-11
Model-12

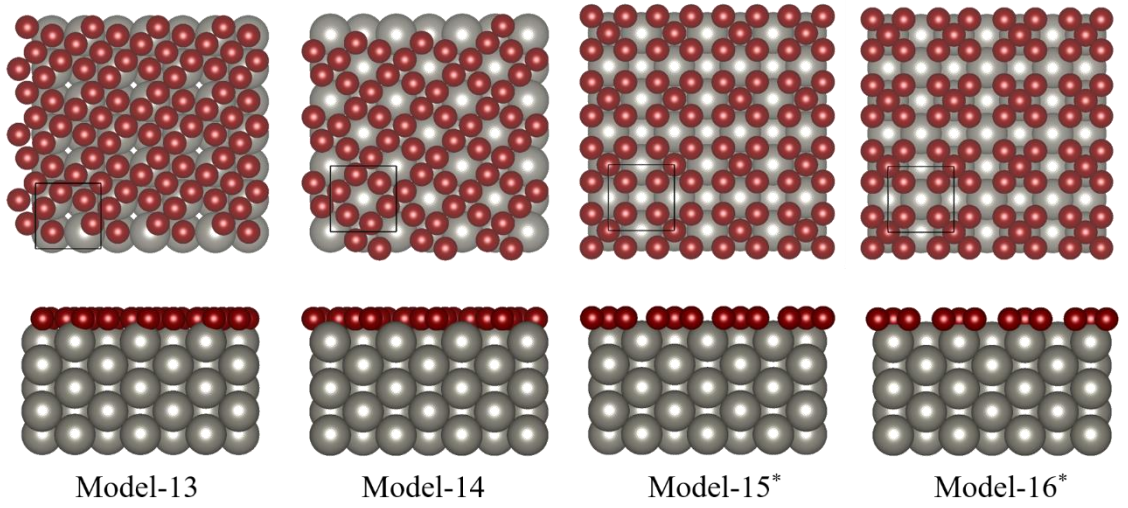

Model-13 Model-14 Model-15* Model-16*

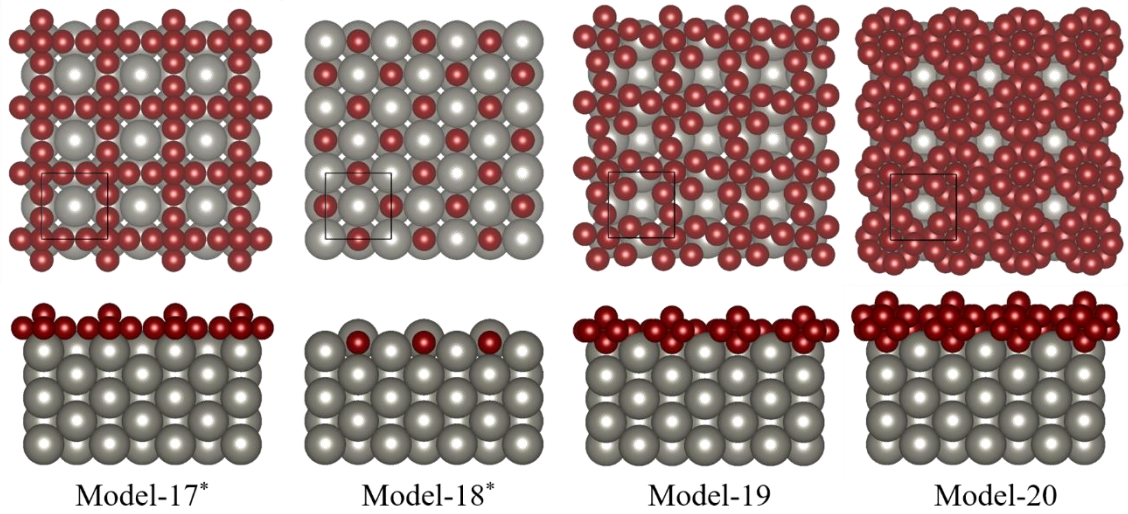

Model-17* Model-18* Model-19 Model-20

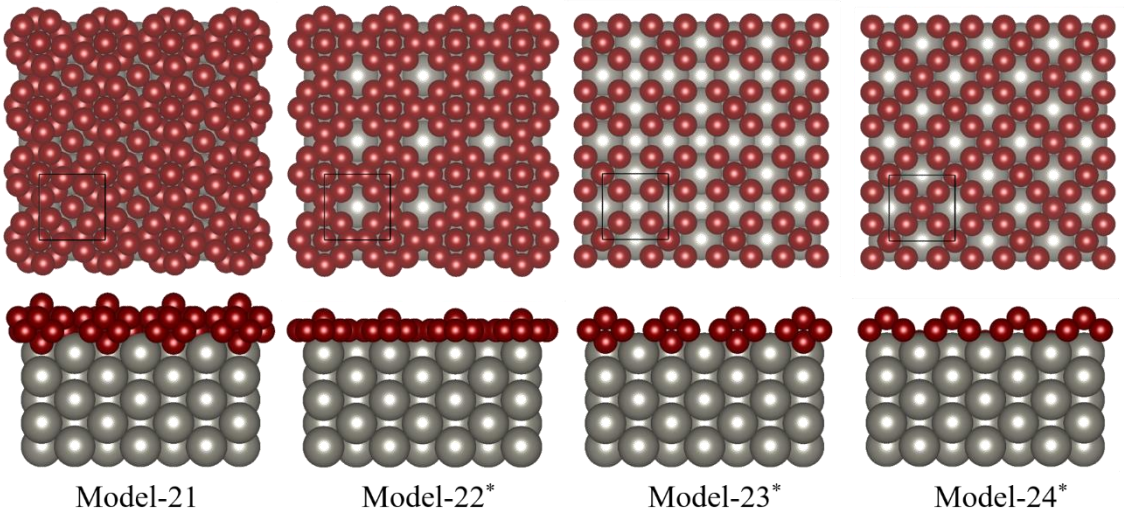

Model-21 Model-22* Model-23* Model-24*

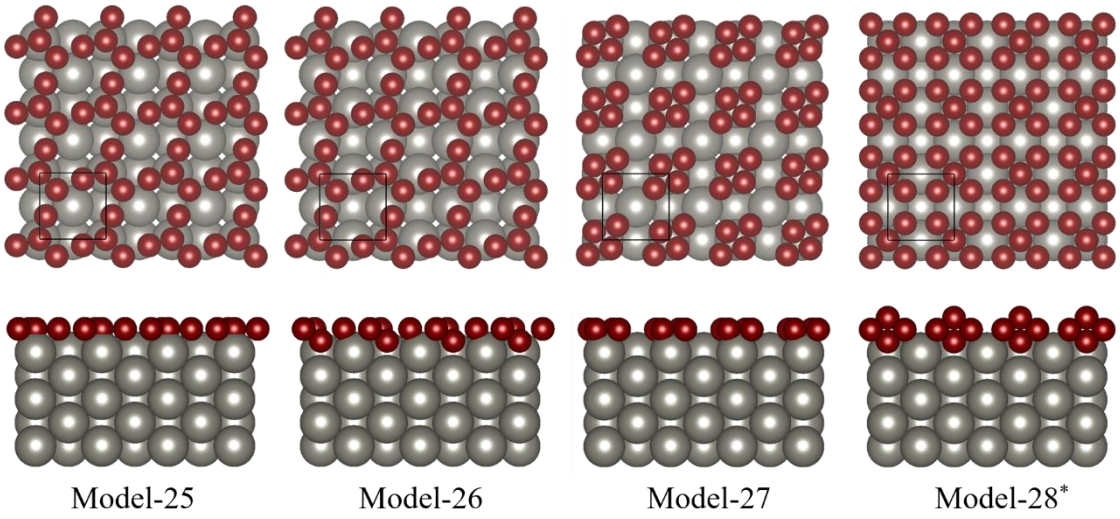

Model-25 Model-26 Model-27 Model-28*

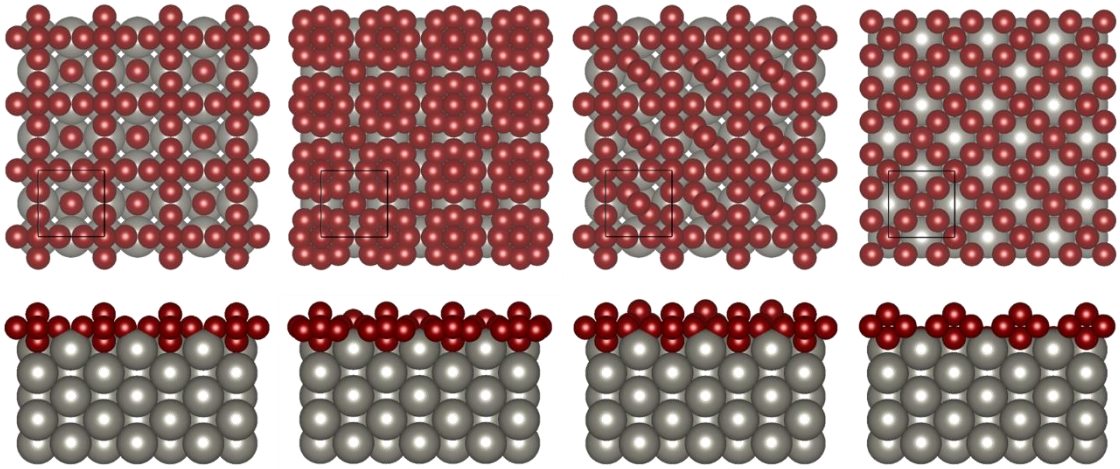

Model-29* Model-30* Model-31 Model-32*

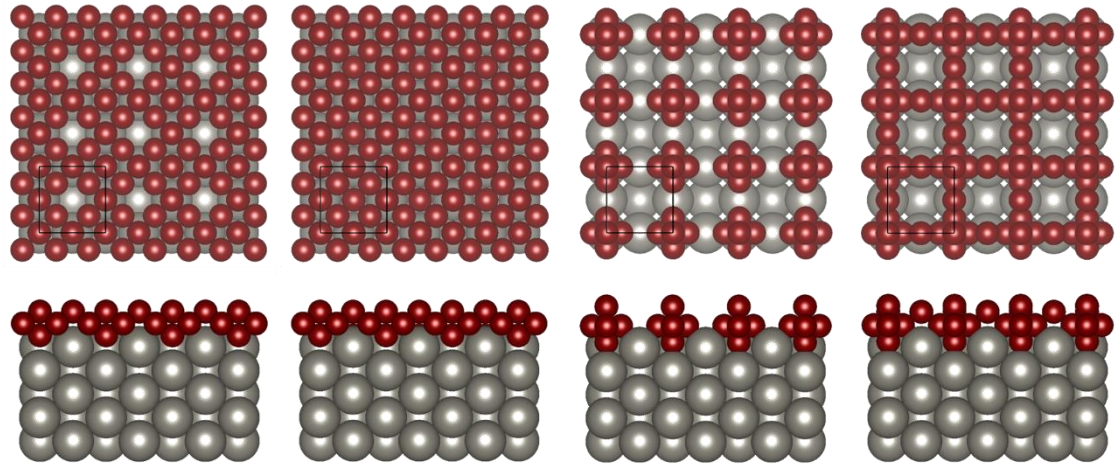

Model-33* Model-34* Model-35* Model-36*

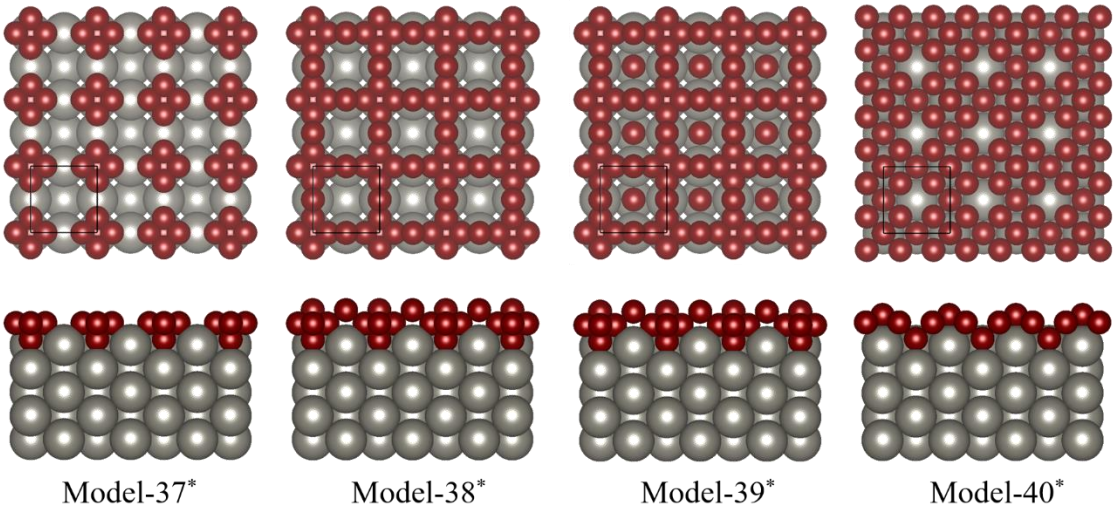

Model-37* Model-38* Model-39* Model-40*

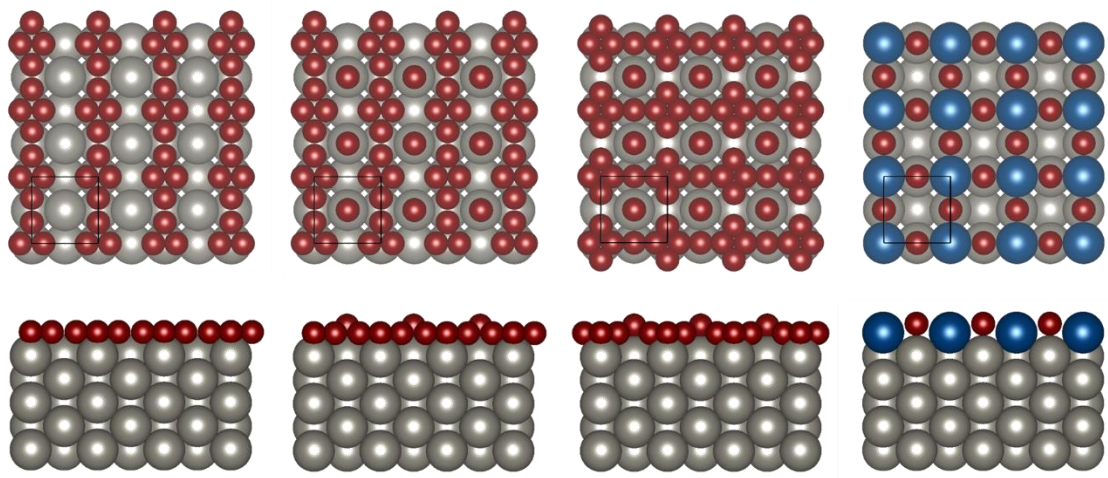

Model-41 Model-42 Model-43 Model-44*

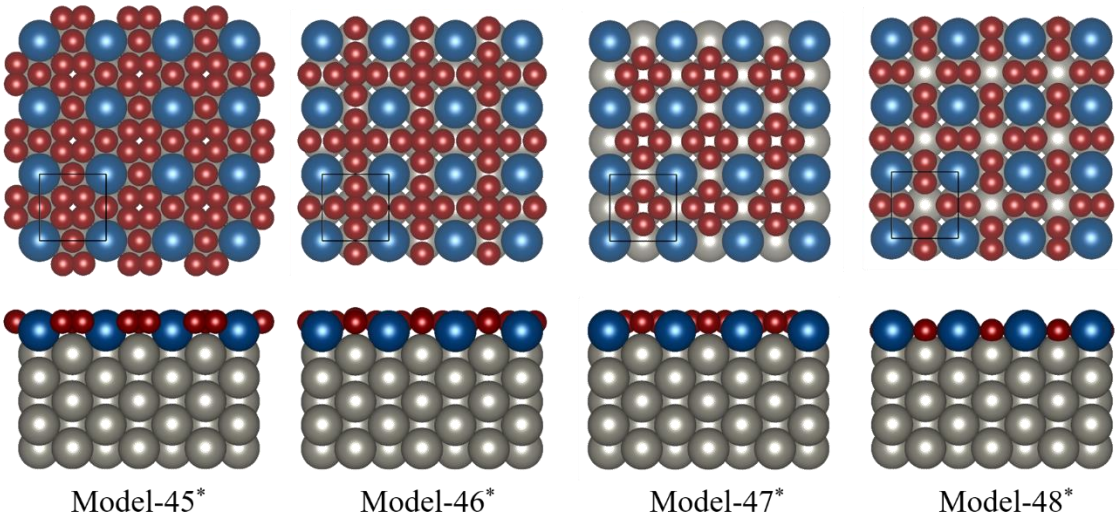

Model-45* Model-46* Model-47* Model-48*

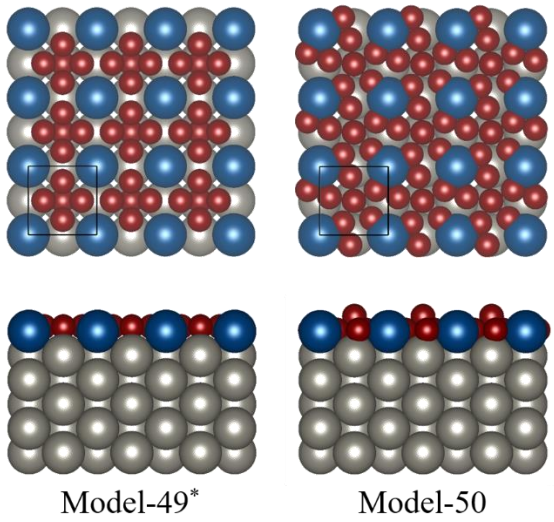

Figure 3.7. Top and side views of 50 ball models for the structure determination of W(100) c(2×2)-B.

[For models (1-43), red and grey balls represent B and W atoms, respectively. In models (43-50), one W atom within the unit cell is replaced by B atoms (red balls) and another W atom at the surface layer is indicated by blue ball. Grey balls represent W atoms of 2^{nd}, 3^{rd}… layers beneath the surface. Black square represents the unit cell. '*' is the indicative for the models with four-fold symmetry.]

Top and cross-sectional views of the best-fitted structure are shown in Figure 3.9. The Debye temperatures were optimized for B, top layer W, second layer W and bulk layer of Was 260, 120, 160 and 400 K, respectively.; and the operating temperature was optimized as 130 K. In Figure 3.10, a comparison between calculated I(E) curves with the experimental curves of the best fit model in the total energy range, ΔE, of 3158 eV for 16 symmetrically inequivalent beams is shown. The numerical values of lateral and vertical displacements of B and W atoms ($W_{1\text{-}1} - W_{5\text{-}2}$) are listed in Table 3.1 with the error range which were calculated from the variance of R_p factor. The lateral displacements and vertical displacements for this model were calculated relative to the ideal four-fold hollow site and ideal top layer of W atoms, respectively.

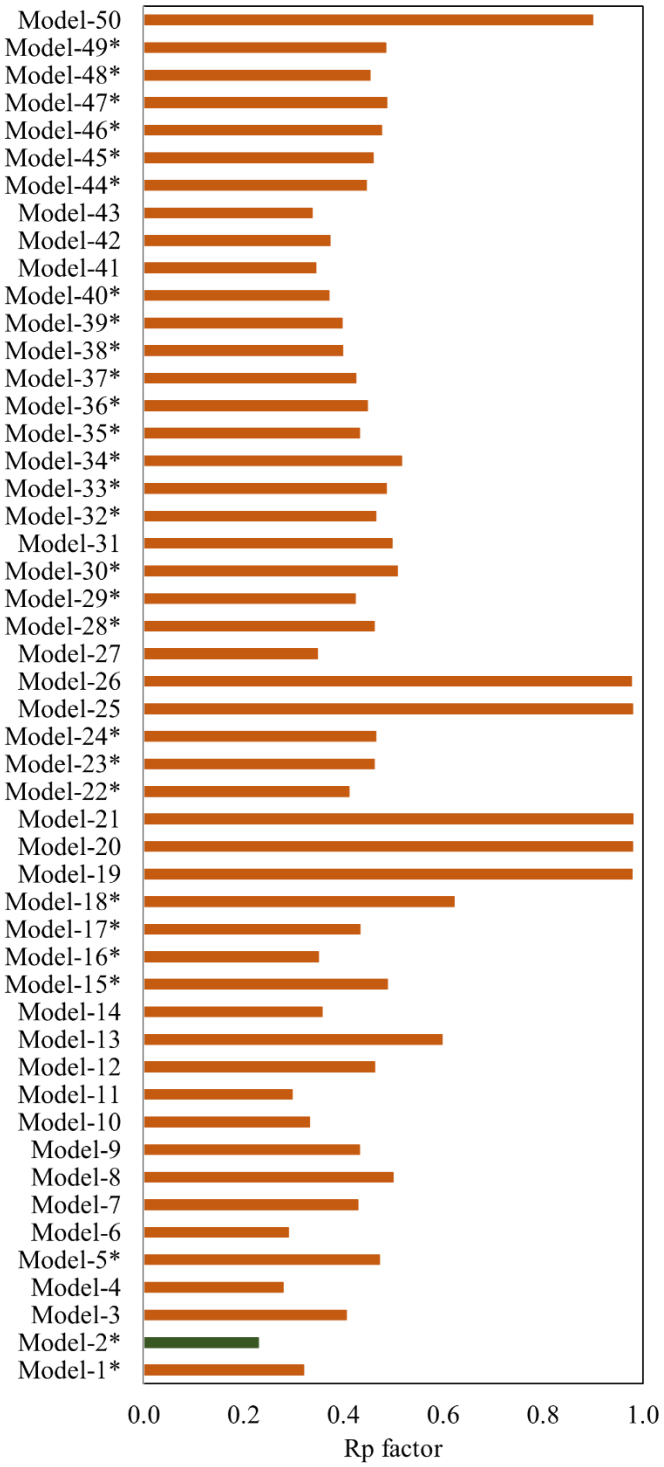

Figure 3.8. Obtained R_p factors for the optimized models (shown in Figure 3.7). ['' is the indicative for the models with four-fold symmetry]*

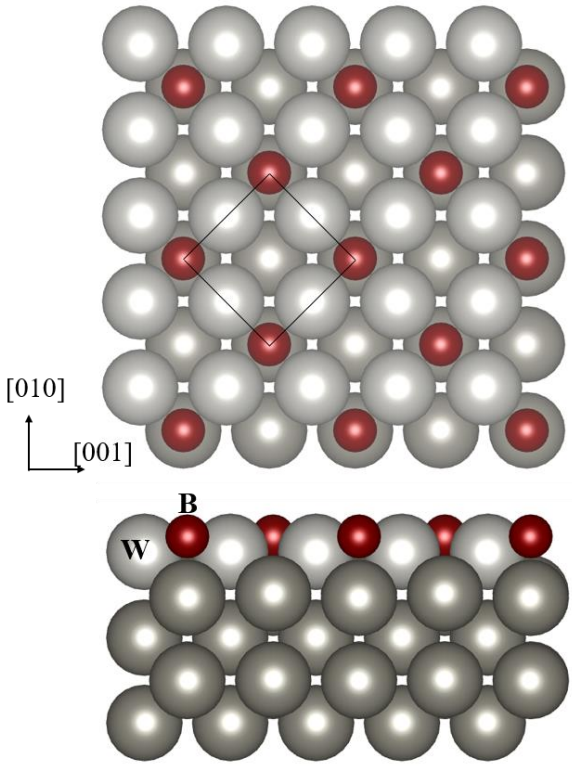

Figure 3.9. Top and cross-sectional views of optimized the best-fit structure of W(100) c(2×2)-B.[Red and grey balls specify B and W atoms, respectively. There are two W atoms in the unit cell of each layer.]

The coverage for the best fit four-fold hollow site structure for W(100) c(2×2)-B was 0.5ML in one unit cell, in which one B atom was located at hollow site position for every two W atoms. In Figure 3.11, side view of the best model with detailed structural parameters after optimization is shown. The vertical distance between B and first layer of W was 0.57 Å forming bond of 2.30 Å between B-$W_{1\text{-}1}$ and B-$W_{1\text{-}2}$. From the LEED analysis, it was found that W atoms in the second and fourth layers ($W_{2\text{-}2}$, $W_{4\text{-}2}$) beneath the B atom shifted downward and other W atoms ($W_{2\text{-}1}$, $W_{4\text{-}1}$) buckled upward. The buckling of W atoms in second layer was found to be 0.16 Å which was comparatively larger than the buckling of fourth layer W atoms of 0.05 Å. A similar buckling condition was observed for S adsorption on other refractory metal, Mo(100), by LEED analysis confining the movement of atom in perpendicular direction [36].

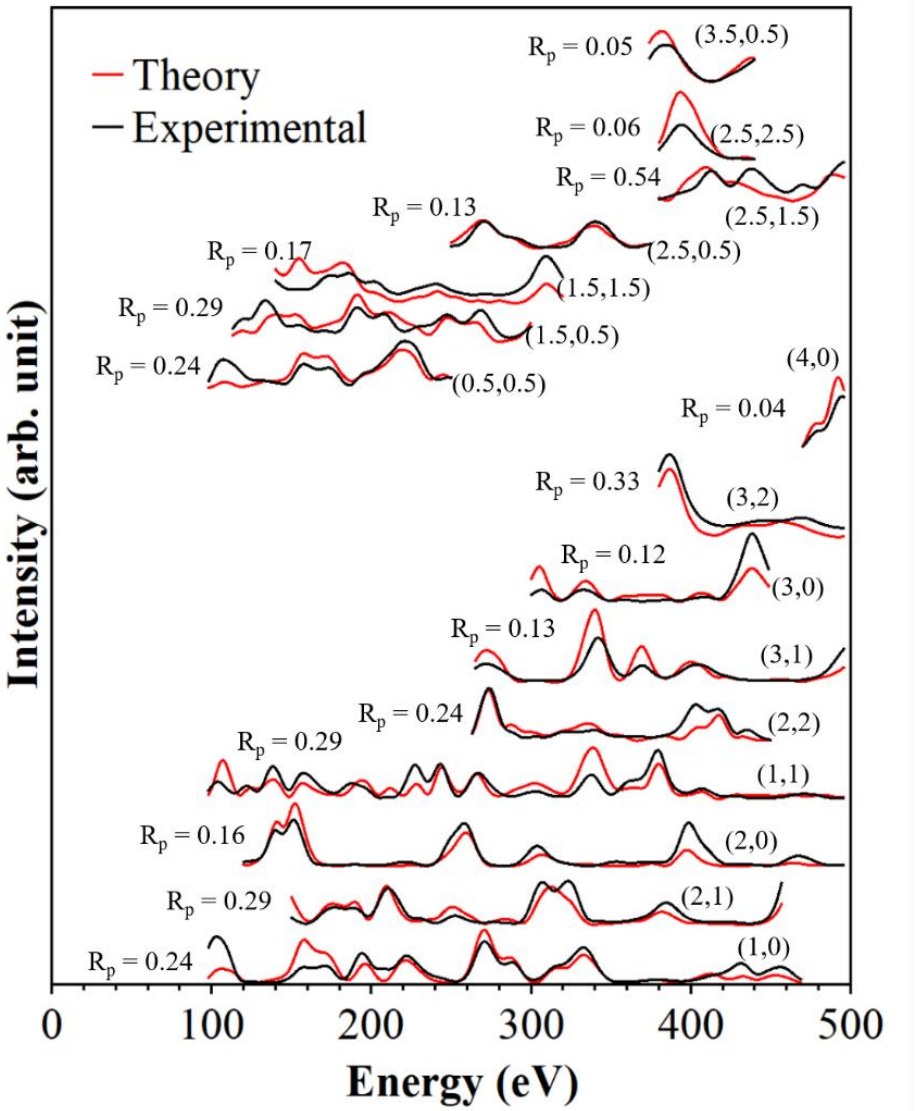

Figure 3.10. Comparison between the experimental (black line) and theoretical (red line) LEED I(E) spectra for best-fit model of W(100)-c(2×2)-B structure.

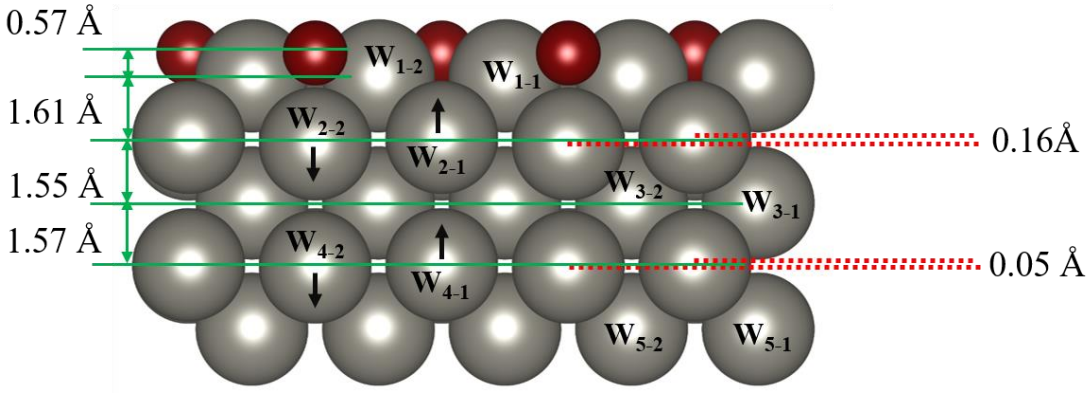

Figure 3.11. Side view of the best fit structure of W(100)-c(2×2)-B, indicating the buckled state in second and fourth layer of W atoms.[W atoms in each layer are designated by W_{n-1}, W_{n-2} (n denotes the number for layers, such as 1,2…..). Red and grey balls represent B and W atoms, respectively.]

In our LEED calculation, the movement of atoms was fixed to the vertical direction for the limitation of symmetry condition. Each B atom interacted with five W atoms forming bond length of 2.3 Å with four W atoms at top layer and 2.26 Å with the W atom at the second layer. It was predicted earlier by first principle calculation that the atomic distance of W-B was 2.264 Å for adsorbing B atom on W(100) surface and B adsorbed on the most stable hollow site position [22]. Interaction of B with five W atoms formed a tungsten boride compound, W_2B, which has low boron concentration. In W_2B, the distance between B atoms is too long to form B-B bond, and therefore, B atoms remain isolated from each other [37,38]. Moreover, theoretically, it was confirmed by Lu et al. that strong chemical bond was formed between B and W atoms at the first layer for W(100) surface and the charge density between B and W atom for this case was the largest, which lead to the formation energy barrier for B diffusion along W(100) surface [22]. Therefore, from the LEED calculation in this study, it is found that B atom positioned at hollow site of W(100) surface with the coverage of 0.5 ML is the best fit model for B adsorption on W(100) with the lowest R_p factor of 0.23 which shows the consistency with the STM observation.

To understand the effect of B adsorption on W(100) surface, we determined the surface relaxation in [100] direction of B adsorbed W(100) surface. Previous LEED analysis for

clean W(001) surface reported contraction between the first and second layer of W; values of contraction varied between 4.4 to 11% [39,40]. On the other hand, for B/W(100) surface, the interlayer spacing between the first two layers of W, $d_{w1\text{-}w2}$, was found to be 1.61 Å which was larger than the bulk interlayer distance of W of 1.5824 Å. In this case, surface relaxation exhibited expansion of 1.7% for the top two layers, followed by a contraction of 2% for the second and third layers of W. The reason behind the expansion between first and second layers was the presence of buckling at the second layer of W atoms. W atom directly below the B atom moved downward, enhancing the distance between first atomic layers. This vertical movement of W atoms at the second layer created bond between B-$W_{2\text{-}2}$ of 2.26 Å forming W_2B compound at the surface.

Therefore, LEED analysis suggests that B adsorption on W(100) restored the four-fold symmetry by positioning at the hollow site of W(100) surface compared to two-fold symmetry of c(2×2) structure of clean reconstructed W(100) surface [40]. The lower R_p factor for the hollow site model and structural parameters confirmed the formation lower boride compound at the surface.

Furthermore, DFT calculation was performed to confirm the hollow site model for W(100) c(2×2)-B structure. Structural parameters for the optimized structure are found to be very similar to that given by LEED calculation which are shown in Table 1, where the interlayer distance between B and W_1 is 0.61 Å, in good agreement with the LEED simulation, 0.57 Å.

Table 3.1. Optimized structural parameters for best fit structure of W(100) c(2×2)-B as determined by LEED. Atoms and their numbers are specified according to the Figure. 3.11. Calculated structural parameters along [100] direction by DFT are also listed here.

Atoms	**[011] (Å)**	**[0$\bar{1}$1] (Å)**	**[100] (Å) LEED**	**[100] (Å) DFT**
B	0.0000	0.0000	-0.57 ± 0.23	-0.61
W_{1-1}	1.5824	1.5824	0.00 ± 0.02	0.00
W_{1-2}	1.5824	-1.5824	0.00 ± 0.02	0.00
W_{2-1}	3.1648	0.0000	1.53 ± 0.03	1.52
W_{2-2}	0.0000	0.0000	1.69 ± 0.04	1.68
W_{3-1}	1.5824	1.5824	3.16 ± 0.02	3.16
W_{3-2}	1.5824	-1.5824	3.16 ± 0.02	3.16
W_{4-1}	3.1648	0.0000	4.70 ± 0.03	4.79
W_{4-2}	0.0000	0.0000	4.75 ± 0.04	4.82
W_{5-1}	1.5824	1.5824	6.3 ± 0.03	6.21
W_{5-2}	1.5824	-1.5824	6.3 ± 0.03	6.21

3.3.2 Scanning tunneling microscopy (STM)

The STM image of clean W(100) surface is shown in Figure 3.12. The large scale STM image (Figure 3.12(a)) exhibited almost flat terrace with a step height of ~1.6 Å which confirmed the cleanliness of surface. In addition, from the high resolution STM topography of clean W(100) surface as shown in Figure 3.12(b), it was found that the average lattice constant for the unit cell was 3.3 Å which nearly matched with the defined lattice constant of W(100) surface (3.2 Å)

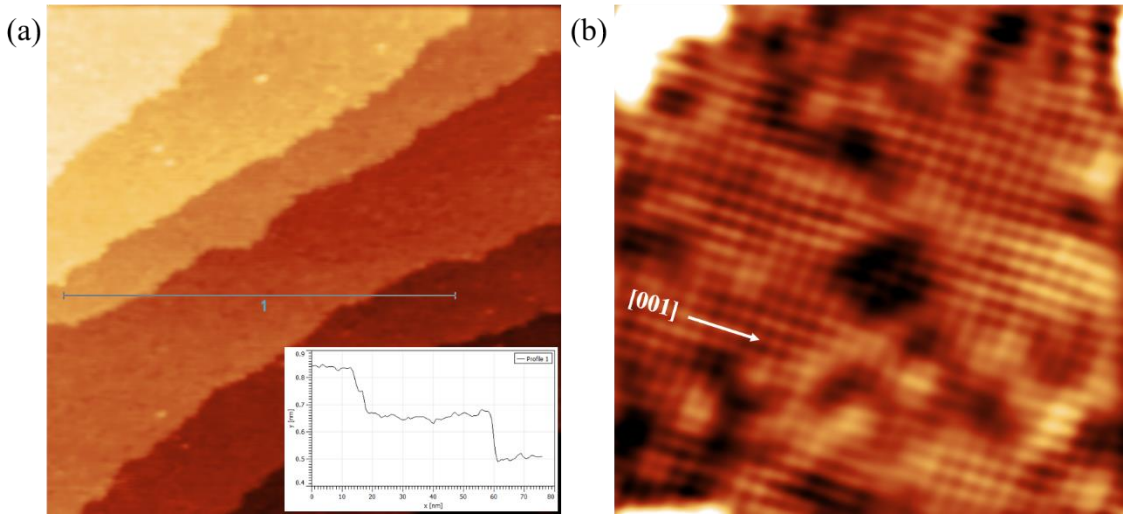

Figure 3.12. (a) Large scale (100nm×100nm) (V_s = 0.02 V, I_t = 0.1 nA) and (b) High resolution (10nm×10nm) (V_s = 0.0 V, I_t = 0.5 nA) STM images of clean W(100) surface. Inset of (a) is showing the step height of clean W(100) surface.

Figure 3.13 shows STM images of B deposited W(100) surfaces. The as-deposited B layer on W(100) at room temperature exhibited a grainy morphology as shown in Figure 3.13 (a), where an obscure LEED (1×1) pattern appeared as shown in the inset of Figure 3.13 (a). B was scattered over the substrate arbitrarily, and some B islands with the height of more than 2 Å were observed, shown in Figure 3.13(b). Some portions of substrate were not covered by B.

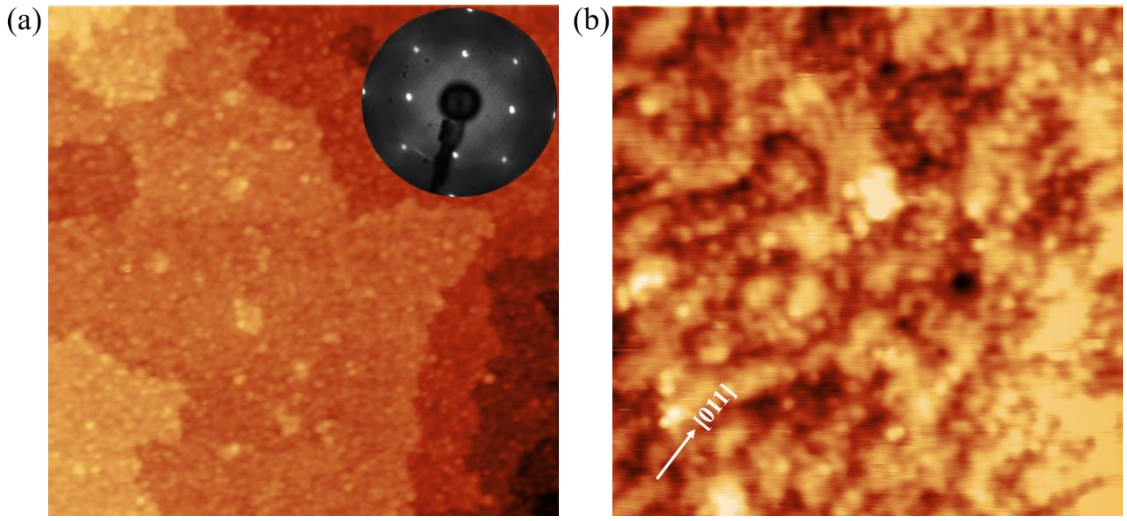

Figure 3.13. (a) Large scale STM image (100nm×100nm) after depositing B on W(100) surface at room temperature (V_s = 0.02 V, I_t = 0.15 nA) and inset in (a) shows the corresponding LEED pattern; exhibiting (1×1) structure with obscure background. (b) A high resolution STM image (20nm×20nm) for the sample shown in (a) revealing the arbitrary B position on W(100) surface (V_s = 2 mV, I_t = 0.5 nA).

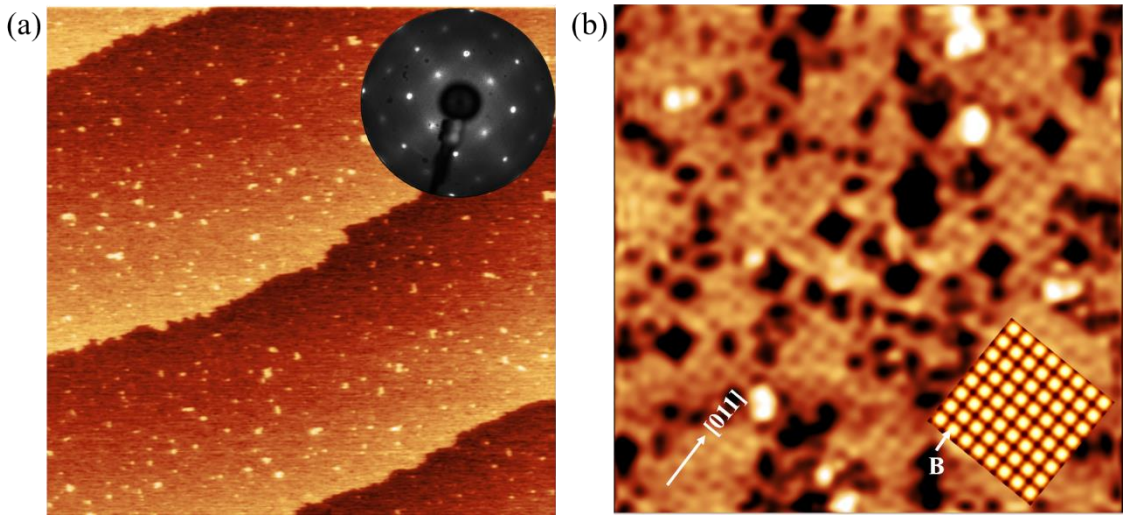

Figure 3.14. (a) Large scale STM image (300nm×300nm) after annealing B covered W(100) surface at 1200 K (V_s = 0.3 V, I_t = 0.3 nA) and inset shows the corresponding LEED pattern; exhibiting c(2×2) structure. (b) A high resolution STM image (15nm×15nm) for the sample shown in (a) (V_s = 2 mV, I_t = 0.15 nA) and the inset shows the simulated STM image.

After annealing at 1200 K, the surface became relatively flat as shown in Figure 3.14(a), and steps with a height of 0.16 nm were clearly observed. The high resolution STM image in Figure 3.14(b) shows regularly arranged square cells and darker regions, indicating the uncovered portion of W(100) surface by B. The length of the unit cell was 4.6 ± 0.2 Å, which is in good agreement with the c(2×2) structure (4.5 Å). Annealed sample shows single domain c(2×2) superstructure, and it seems that the surface has a four-fold symmetry. Based on the optimized structure, a simulated STM image was obtained for it, which is shown in the inset of Figure 3.14(b). In the simulated STM image, bright protrusions correspond to B atoms.

3.3.3 X-ray photoelectron spectroscopy (XPS)

The chemical interactivity of B and W for W(100) c(2×2)-B structure was determined by analyzing the B1s, W 4d, and W 4f spectra obtained from XPS measurements. B 1s spectra of clean W(100) substrate, as deposited B on W(100) and after annealing the substrate in the range of binding energy between 185 eV to 194 eV are shown in Figure 3.15.

No observable peak was found in B1s spectrum for clean W(100) surface, indicating the sample was clean and free from B atoms. A wide scan of XPS spectrum, as shown in Figure 3.16, revealed that the substrate contained no contamination. After depositing B on W(100), the binding energy of B1s peak was found at the binding energy of ~187.6 eV, which was slightly shifted from the pure bulk state of boron (188.5 eV) [41]. The spectrum of B1s for pure boron is shown in Figure 3.17. For the formation of c(2×2) structure for B/W(100), sample was annealed at ~1200 K for 10 min. XPS spectrum exhibited the existence peak of B1s at the binding energy of 187.8 eV for the sample with c(2×2) ordered structure. Hence, no significant peak shifting was observed for c(2×2) structure of B/W(100) after annealing. B1s peak was shifted towards lower binding energy after the deposition of B and annealing the sample at higher temperature by 0.9 eV and 0.7 eV, respectively, compared to the B1s peak for bulk boron.

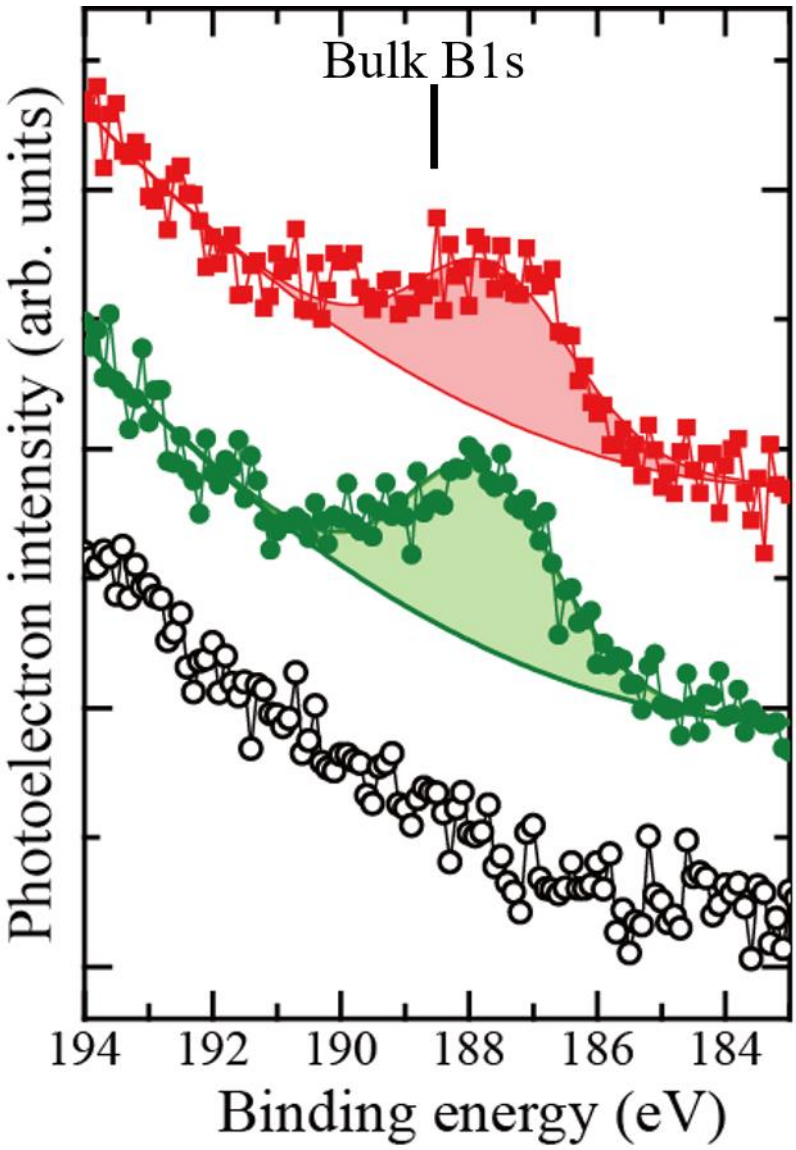

Figure 3.15. XPS spectra of B1s core level for clean W(100) (open circles), B 10 min deposition (filled green circles), and subsequently annealed sample (filled red squares).The solid lines are fitting results with backgrounds. Each spectrum is shifted vertically for clarity]

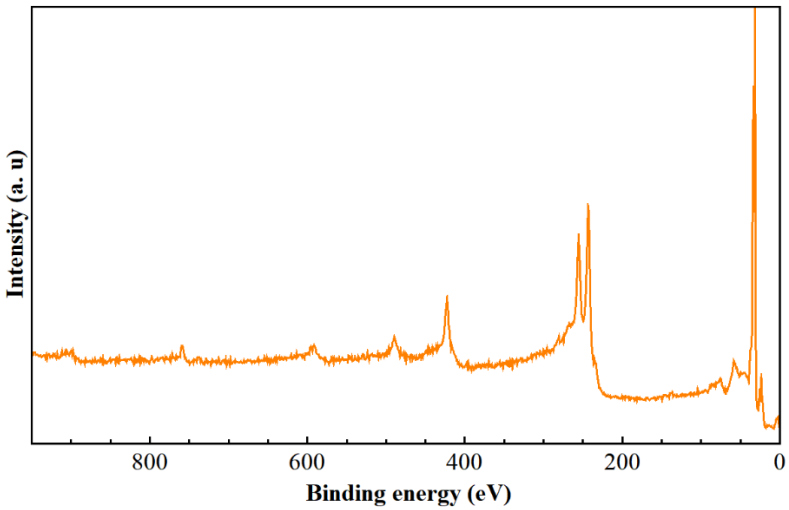

Figure 3.16. Wide scan XPS spectrum of clean W(100).

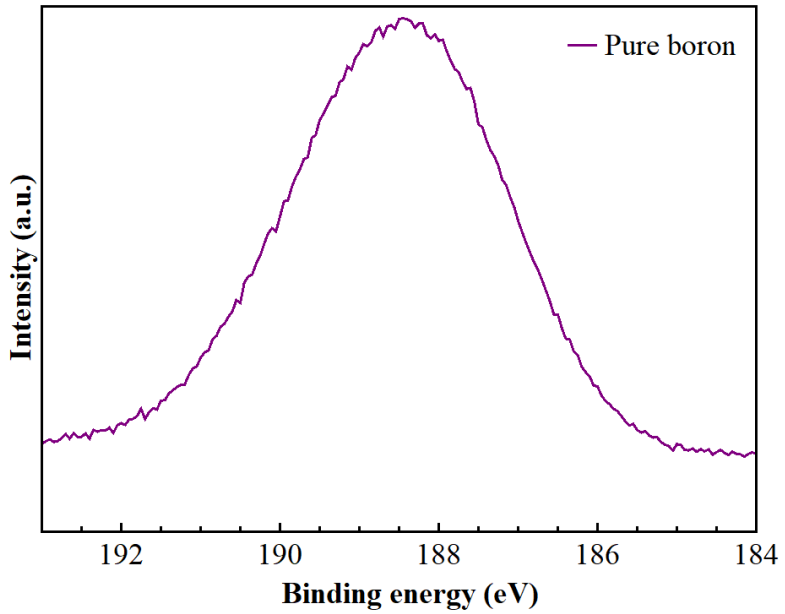

Figure 3.17. XPS spectrum of B-1s for pure boron.

Moreover, XPS spectra of B1s for B covered W(100) surface with the increase of annealing temperatures are shown in Figure 3.18. Peak intensity variation with respect to the annealing temperature was depicted in Figure 3.19. It can be seen that peak intensity remains almost the same up to annealing the substrate at 1500 K. As the superstructure

formed in the range of temperature between 800-1400 K, and the peak intensity in that range were nearly constant, indicating no significant change of B amount over the surface after deposition and subsequently annealed at higher temperature to form c(2×2) structure. Annealing temperature above 1500 K led to diffuse B into the bulk which caused to reduce the peak intensity of B. Further annealing at more than 1600 K decreased the B amount very sharply indicating the surface became almost free from B atoms which was also observed from LEED as it exhibits p(1×1) structure at this condition.

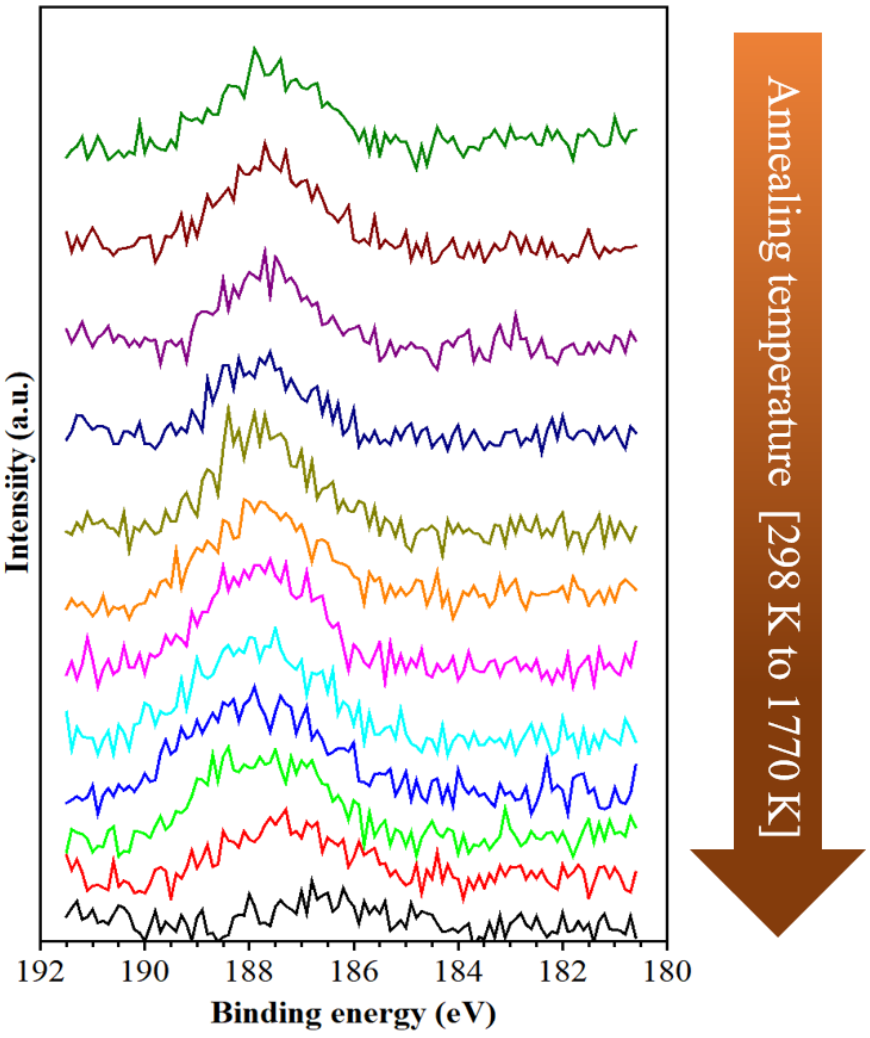

Figure 3.18. XPS spectra of B1s with the increase of annealing temperature of the substrate.

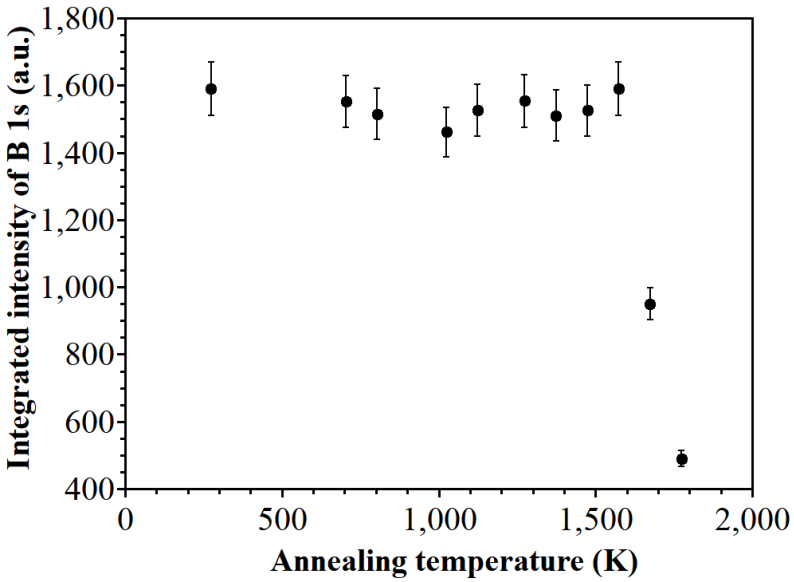

Figure 3.19. Change of peak intensities of B1s with the annealing temperature of the substrate.

According to the electronegativities of B and W, the electron will transfer from W to B atom for higher boride components, whereas, for lower boride compounds, such as W_4B, B valance electrons are shared with the refractory metal atom [38]. However, the B1s binding energy of boron rich boride compounds, such as WB_2 and MoB_2, were found at 188.1 eV and 188.2 eV, while adsorption of B on refractory metal substrate at lower coverage exhibited the presence of B1s peak at the binding energy of 186.8 eV [42,43]. Therefore, increasing B coverage shifted the peak to the higher binding energy due to the B-B interaction [43]. In our study, B1s peak was observed at ~187.8 eV after forming c(2×2) superstructure indicated the formation of tungsten boride compound with low concentration of B at the surface of W(100). Moreover, the downward peak shifting of B1s, indicating the transfer of electrons occurred from metal (W) to B atom. The ratio peak intensity of B1s for the ordered pattern after annealing and only B adsorption on W(100) was 0.91, indicating that forming c(2×2) structure after annealing did not involve B diffusion significantly. The number of B atoms after deposition and annealing remained almost the same. Previously it was predicted that the energy barrier for B diffusion along W(100) surface was the largest of 2.31 eV as well as the behavior of charge transfer from W to B atom was stronger for this surface compared to the other surface of W [22]. It can

be concluded from XPS measurements that B atoms scattered over the W(100) surface just after deposition and formed chemical bond with W atoms. After annealing the sample, B oriented at crystallographic positions forming an ordered structure, and adjacent B and W atoms created strong chemical bonds at the surface by transferring electrons from W atoms to B atoms. The presence of strong interaction between B and W atoms before and after annealing the sample was confirmed by the peak position of B1s; as no significant peak shifting was observed by XPS measurements. Along with, the obtained peak intensities for B1s before and after annealing the sample were comparatively small, which indicated a few B atoms were arranged over W(100) surface. Lack of B atoms on W(100), formation of strong chemical bond between B and W atom, and no significant B diffusion along W(100) surface attributed to the formation of metal(W) rich boride compounds at the surface as for a metal-rich boride compound, W_2B, B atom has the ability to accept electron and the bond created between B-W is ionic [37,38]. Thus, XPS analysis for B/W(100) manifested that a tungsten boride compound with lower concentration of B was formed for W(100) c(2×2)-B structure which coincided with the LEED result.

In summary, B on W(100) shows c(2×2) structure with B on the hollow site upon annealing to ~1200 K, while the as-deposited B atoms are scattered on W(100) at room temperature. The detailed surface structure was confirmed by LEED analysis, which reveals that the B atoms are surrounded by five W atoms with distances of 2.26-2.30 Å, which is close to the atomic distance in W_2B. High resolution STM image exhibits some small regions containing few unit cells with the lattice constant of 4.6±0.2 Å along both $[\bar{1}10]$ and [110] directions which confirm the formation of c(2×2) superstructure maintaining four-fold symmetry upon B deposition. XPS measurement shows that B1s peak shifting towards lower binding energy compared to pure B1s, indicating the charge transfer from W to B. The analysis of these experimental results makes it plausible to attribute the W(100) c(2×2)-B superstructure to W_2B ordered surface alloy. The lack of boron sheet on W(100) would originate from the stable tungsten boride formation on the surface.

References

[1] W.L. Li, X. Chen, T. Jian, T.T. Chen, J. Li, L.S. Wang, From planar boron clusters to borophenes and metalloborophenes, Nat. Rev. Chem. 1 (2017). https://doi.org/10.1038/s41570-017-0071.

[2] X. Sun, X. Liu, J. Yin, J. Yu, Y. Li, Y. Hang, X. Zhou, M. Yu, J. Li, G. Tai, W. Guo, Two-dimensional boron crystals: structural stability, tunable properties, fabrications and applications, Adv. Funct. Mater. 27 (2017). https://doi.org/10.1002/adfm.201603300.

[3] C.B. Kah, M. Yu, P. Tandy, C.S. Jayanthi, S.Y. Wu, Low-dimensional boron structures based on icosahedron B_{12}, Nanotechnology. 26 (2015). https://doi.org/10.1088/0957-4484/26/40/405701.

[4] Z. Zhang, Y. Yang, E.S. Penev, B.I. Yakobson, Elasticity, flexibility, and ideal strength of borophenes, Adv. Funct. Mater. 27 (2017). https://doi.org/10.1002/adfm.201605059.

[5] A.J. Mannix, X.F. Zhou, B. Kiraly, J.D. Wood, D. Alducin, B.D. Myers, X. Liu, B.L. Fisher, U. Santiago, J.R. Guest, M.J. Yacaman, A. Ponce, A.R. Oganov, M.C. Hersam, N.P. Guisinger, Synthesis of borophenes: Anisotropic, two-dimensional boron polymorphs, Science. 350 (2015) 1513–1516. https://doi.org/10.1126/Xscience.aad1080.

[6] B. Feng, J. Zhang, S. Ito, M. Arita, C. Cheng, L. Chen, K. Wu, F. Komori, O. Sugino, K. Miyamoto, T. Okuda, S. Meng, I. Matsuda, Discovery of 2D anisotropic Dirac cones, Adv. Mater. 30 (2018) 2–7. https://doi.org/10.1002/adma.201704025.

[7] D. Ayodhya, G. Veerabhadram, A brief review on synthesis, properties and lithium-ion battery applications of borophene, FlatChem. 19 (2020) 100150. https://doi.org/10.1016/j.flatc.2019.100150.

[8] Z. Zhang, Y. Yang, G. Gao, B.I. Yakobson, Two-dimensional boron monolayers mediated by metal substrates, Angew. Chemie - Int. Ed. 54 (2015) 13022–13026. https://doi.org/10.1002/anie.201505425.

[9] A.J. Mannix, Z. Zhang, N.P. Guisinger, B.I. Yakobson, Borophene as a prototype for synthetic 2D materials development, Nat. Nanotechnol. 13 (2018) 444–450. https://doi.org/10.1038/s41565-018-0157-4.

[10] S. Xie, Y. Wang, X. Li, Flat Boron: A new cousin of graphene, Adv. Mater. 31 (2019) 1900392. https://doi.org/10.1002/adma.201900392.

[11] H.-J. Zhai, B. Kiran, J. Li, L.-S. Wang, Hydrocarbon analogues of boron clusters — planarity, aromaticity and antiaromaticity, Nat. Mater. 2 (2003) 827–833. https://doi.org/10.1038/nmat1012.

[12] W. Li, L. Kong, C. Chen, J. Gou, S. Sheng, W. Zhang, H. Li, L. Chen, P. Cheng, K. Wu, Experimental realization of honeycomb borophene, Sci. Bull. 63 (2018) 282–286. https://doi.org/10.1016/j.scib.2018.02.006.

[13] R. Wu, A. Gozar, I. Božović, Large-area borophene sheets on sacrificial Cu(111) films promoted by recrystallization from subsurface boron, Quantum Mater. 4 (2019) 40. https://doi.org/10.1038/s41535-019-0181-0.

[14] R. Wu, I.K. Drozdov, S. Eltinge, P. Zahl, S. Ismail-Beigi, I. Božović, A. Gozar, Large-area single-crystal sheets of borophene on Cu(111) surfaces, Nat. Nanotechnol. 14 (2019) 44–49. https://doi.org/10.1038/s41565-018-0317-6.

[15] B. Kiraly, X. Liu, L. Wang, Z. Zhang, A.J. Mannix, B.L. Fisher, B.I. Yakobson, M.C. Hersam, N.P. Guisinger, Borophene synthesis on Au(111), ACS Nano. 13 (2019) 3816–3822. https://doi.org/10.1021/acsnano.8b09339.

[16] N.A. Vinogradov, A. Lyalin, T. Taketsugu, A.S. Vinogradov, A. Preobrajenski, Single-phase borophene on Ir(111): Formation, structure, and decoupling from the support, ACS Nano. 13 (2019) 14511–14518. https://doi.org/10.1021/acsnano.9b08296.

[17] B. Feng, J. Zhang, Q. Zhong, W. Li, S. Li, H. Li, P. Cheng, S. Meng, L. Chen, K. Wu, Experimental realization of two-dimensional boron sheets, Nat. Chem. 8 (2016) 563–568. https://doi.org/10.1038/nchem.2491.

[18] Q. Zhong, L. Kong, J. Gou, W. Li, S. Sheng, S. Yang, P. Cheng, H. Li, K. Wu, L. Chen, Synthesis of borophene nanoribbons on Ag(110) surface, Phys. Rev. Mater. 1 (2017) 021001. https://doi.org/10.1103/PhysRevMaterials.1.021001.

[19] Y. Wang, L. Kong, C. Chen, P. Cheng, B. Feng, K. Wu, L. Chen, Realization of regular-mixed quasi-1D borophene chains with long-range order, Adv. Mater. 32 (2020) 1–6. https://doi.org/10.1002/adma.202005128.

[20] Z.H. Cui, E. Jimenez-Izal, A.N. Alexandrova, Prediction of two-dimensional phase of boron with anisotropic electric conductivity, J. Phys. Chem. Lett. 8 (2017) 1224–1228. https://doi.org/10.1021/acs.jpclett.7b00275.

[21] W. Tucker, Interaction of boron with tungsten single crystal substrates, Surf. Sci. 5 (1966) 179–186. https://doi.org/10.1016/0039-6028(66)90079-3.

[22] C. Lu, J. Yang, X. Lei, J. Huang, Z. Ye, S. Chen, Y. Zhao, First-principles calculations on adsorption-diffusion behavior of Boron atom with tungsten surface, Comput. Mater. Sci. 183 (2020) 109908. https://doi.org/10.1016/j.commatsci.2020.109908.

[23] T.E. Felter, R.A. Barker, P.J. Estrup, Phase transition on Mo(100) and W(100) surfaces, Phys. Rev. Lett. 38 (1977) 1138–1142. https://doi.org/10.1103/PhysRevLett.38.1138.

[24] K. Kankaala, T. Ala-Nissila, S.C. Ying, Theory of adsorbate-induced surface reconstruction on W(100), Phys. Rev. B. 47 (1993) 2333–2343. https://doi.org/10.1103/PhysRevB.47.2333.

[25] P. Hu, A. Wander, L.M. de la Garza, M.P. Bessent, D.A. King, An adsorbate-stabilised vacancy structure for Cu on W{100}: A surface alloy, Surf. Sci. 286 (1993) 542–546. https://doi.org/10.1016/0039-6028(93)90546-V.

[26] M. Kabiruzzaman, R. Ahmed, T. Nakagawa, S. Mizuno, Ordered mixed rows of (Pb + Sn) and (Pb + Sb) on Cu(001): A coadsorption study and structure determination using low energy electron diffraction, Surf. Sci. 677 (2018). https://doi.org/10.1016/j.susc.2018.06.002.

[27] R. Ahmed, T. Nakagawa, S. Mizuno, Structure determination of ultra-flat stanene on Cu(111) using low energy electron diffraction, Surf. Sci. 691 (2020) 121498. https://doi.org/10.1016/j.susc.2019.121498.

[28] M.A. Van Hove, W. Moritz, H. Over, P.J. Rous, A. Wander, A. Barbieri, N. Materer, U. Starke, G.A. Somorjai, Automated determination of complex surface structures by LEED, Surf. Sci. Rep. 19 (1993) 191–229. https://doi.org/10.1016/0167-5729(93)90011-D.

[29] J.B. Pendry, Reliability factors for LEED calculations, J. Phys. C Solid State Phys. 13 (1980) 937–944. https://doi.org/10.1088/0022-3719/13/5/024.

[30] D. Vanderbilt, Soft self-consistent pseudopotentials in a generalized eigenvalue formalism, Appl. Opt. 41 (1990) 7892–7895. https://doi.org/10.1016/S0016-5085(77)80340-5.

[31] J.P. Perdew, J.A. Chevary, S.H. Vosko, K.A. Jackson, M.R. Pederson, D.J. Singh, C. Fiolhais, Atoms, molecules, solids, and surfaces: Applications of the generalized gradient approximation for exchange and correlation, Phys. Rev. B. 48 (1993) 4978. https://doi.org/10.1103/PhysRevB.48.4978.2.

[32] H.J. Monkhorst, J.D. Pack, Special points for Brillouin-zone integrations, Phys.

Rev. B. 13 (1976) 5188–5192. https://doi.org/10.1103/PhysRevB.13.5188.

[33] P. Giannozzi, S. Baroni, N. Bonini, M. Calandra, R. Car, C. Cavazzoni, D. Ceresoli, G.L. Chiarotti, M. Cococcioni, I. Dabo, A. Dal Corso, S. de Gironcoli, S. Fabris, G. Fratesi, R. Gebauer, U. Gerstmann, C. Gougoussis, A. Kokalj, M. Lazzeri, L. Martin-Samos, N. Marzari, F. Mauri, R. Mazzarello, S. Paolini, A. Pasquarello, L. Paulatto, C. Sbraccia, S. Scandolo, G. Sclauzero, A.P. Seitsonen, A. Smogunov, P. Umari, R.M. Wentzcovitch, Quantum espresso: a modular and open-source software project for quantum simulations of materials, J. Phys. Condens. Matter. 21 (2009) 395502. https://doi.org/10.1088/0953-8984/21/39/395502.

[34] P. Giannozzi, O. Andreussi, T. Brumme, O. Bunau, M. Buongiorno Nardelli, M. Calandra, R. Car, C. Cavazzoni, D. Ceresoli, M. Cococcioni, N. Colonna, I. Carnimeo, A. Dal Corso, S. De Gironcoli, P. Delugas, R.A. Distasio, A. Ferretti, A. Floris, G. Fratesi, G. Fugallo, R. Gebauer, U. Gerstmann, F. Giustino, T. Gorni, J. Jia, M. Kawamura, H.Y. Ko, A. Kokalj, E. Kücükbenli, M. Lazzeri, M. Marsili, N. Marzari, F. Mauri, N.L. Nguyen, H. V. Nguyen, A. Otero-De-La-Roza, L. Paulatto, S. Poncé, D. Rocca, R. Sabatini, B. Santra, M. Schlipf, A.P. Seitsonen, A. Smogunov, I. Timrov, T. Thonhauser, P. Umari, N. Vast, X. Wu, S. Baroni, Advanced capabilities for materials modelling with Quantum espresso, J. Phys. Condens. Matter. 29 (2017) 465901. https://doi.org/10.1088/1361-648X/aa8f79.

[35] A. Otero-De-La-Roza, E.R. Johnson, V. Luaña, Critic2: A program for real-space analysis of quantum chemical interactions in solids, Comput. Phys. Commun. 185 (2014) 1007–1018. https://doi.org/10.1016/j.cpc.2013.10.026.

[36] D.W. Jentz, Surface structure determinations of ordered sulfur overlayers on Mo(100) and Re(0001) by low-energy electron diffraction intensity analysis, Berkeley, CA (United States), (1992). https://doi.org/10.2172/10186839.

[37] Q. Li, L. Wang, X. Ai, H. Chen, J. Zou, G.D. Li, X. Zou, Multiple crystal phases of intermetallic tungsten borides and phase-dependent electrocatalytic property for hydrogen evolution, Chem. Commun. 56 (2020) 13983–13986. https://doi.org/10.1039/d0cc06072k.

[38] D.R. Glasson, J.A. Jones, Formation and reactivity of borides, carbides and silicides. I. review and introduction, J. Appl. Chem. 19 (2007) 125–137. https://doi.org/10.1002/jctb.5010190501.

[39] J.B. Pendry, K. Heinz, W. Oed, H. Landskron, K. Müller, G. Schmidtlein, A disordered model for the W(100)1×1 surface, Surf. Sci. 193 (1988) L1–L6. https://doi.org/10.1016/0039-6028(88)90310-X.

[40] M.K. Debe, D.A. King, The clean thermally induced W {001} (1 × 1) → (√2 × √2) R 45° surface structure transition and its crystallography, Surf. Sci. 81 (1979) 193–237. https://doi.org/10.1016/0039-6028(79)90513-2.

[41] J.F. Moulder, W.F. Stickle, P.E. Sobol, K.D. Bomben, Handbook of X-ray Photoelectron Spectroscopy, Perkin-Elmer Corp., John Wiley & Sons, Ltd, Chichester, UK, (2005). https://doi.org/10.1002/0470014229.ch22.

[42] C. Wang, Q. Tao, S. Ma, T. Cui, X. Wang, S. Dong, P. Zhu, WB_2 : not a superhard material for strong polarization character of interlayer W–B bonding, Phys. Chem. Chem. Phys. 19 (2017) 8919–8924. https://doi.org/10.1039/C6CP04287B.

[43] T.B. Fryberger, J.L. Grant, P.C. Stair, Adsorption of boron on molybdenum(100) and its effect on chemisorption of carbon monoxide, ethene, propene, and 3,3,3-trifluoropropene, Langmuir. 3 (1987) 1015–1025. https://doi.org/10.1021/la00078a024.

CHAPTER 4:
B
ADSORPTION
ON Mo(110)

4.1 Introduction

Due to the unique nature and complex bonding configurations, B can form many stable 2D B sheets comprised of triangular lattices with a different arrangement of periodic holes [1,2]. The hexagonal hole concentration is defined by η, which is the ratio of the number of holes in the triangular lattice to the number of boron atoms within the unit cell [3]. However, the synthesis of borophene experimentally was a great challenge as the bulk B compound is not a naturally layered material like graphite, and thereby, preparing 2D B sheet cannot be possible by exfoliating from bulk B compound [4]. Recently, borophene synthesis was carried out on different metal substrates as the borophene structure is dependent on the interaction between the metal-borophene interface.

Among other surfaces of refractory metal, Mo(110) substrate is considered as one of the most promising substrates for the growth of 2D B sheet as it was predicted earlier by Cui et al., [5] that a new 2D B phase (named as π phase) could be grown on W(110) surface. In previous studies, adsorption of various elements on Mo(110) surface were conducted [6–12]. While only concerning on B adsorption of molybdenum surface, Magkoev et al. [13] observed that unstable state of B atoms remained on Mo(110) at room temperature while increasing the annealing temperature diffused B into the bulk completely at 2000 K as well as XPS results showed the formation of bond between B and Mo at 1150 K. The interactivity between B and Mo was analyzed with the variation of temperature and coverage by Fryberger et al. [14], the B arrangement over Mo(110) surface at different temperatures has remained unspecified.

In this study, growth of B on Mo(110) at various temperatures has been reported by STM and LEED. STM observations determined the structural condition of B atoms over Mo(110) surface. It was noticed that arbitrary distribution of B atoms took place on the substrate after deposition at room temperature and ordered structure forms by annealing the substrate at the higher temperature. LEED results confirmed the generation of ordered structure as the LEED pattern exhibited $\begin{pmatrix} 0 & -9 \\ 1 & 1 \end{pmatrix}$ superstructure formation upon heating the substrate at high temperature. Combining the STM results with LEED, alignment of B atoms in continuous 2D sheet on Mo(110) surface has been obtained.

4.2 Experiment

All the experiments for B growth onto Mo(110) surface were conducted in *in-situ* UHV chamber with a base pressure of 2×10^{-8} Pa. STM image was taken at low temperature (77 K), and this chamber was equipped with four grid LEED system and e-beam evaporator. For sample preparation, Mo(110) substrate was fixed in a nonmagnetic sample holder and cleaned by repeatedly annealing in oxygen atmosphere with a pressure of 6×10^{-6} Pa at 1500 K for 10 minutes and flashing at 2100 K for 10 seconds. Ar^{+} sputtering (1.5KV, 5μA, 10 min) and subsequent annealing at 1700 K were also carried out for getting sharp p(1×1) LEED pattern which indicated the cleanliness of substrate. After preparing clean Mo(110) substrate, highly pure B was evaporated from a crucible on cleaned Mo(110) surface by e-beam evaporator at room temperature. The deposition rate of B was monitored by quartz crystal microbalance (QCM). After the deposition of B on Mo(110) at room temperature, sample was annealed at several temperatures (800 K, 1200K and 1500 K). Then, the LEED patterns at different conditions were taken at the image chamber. After the sample preparation, sample was brought to the low temperature STM chamber without interrupting the UHV condition for recording topographic image by electrochemically etched PtIr tip.

4.3 Results and discussion

4.3.1 Low energy electron diffraction (LEED)

After repeated oxidation followed by flushing at high temperature, LEED pattern exhibited sharp p(1×1) structure for Mo(110) surface, which is shown in Figure 4.1 confirming the cleanliness of Mo(110) surface.

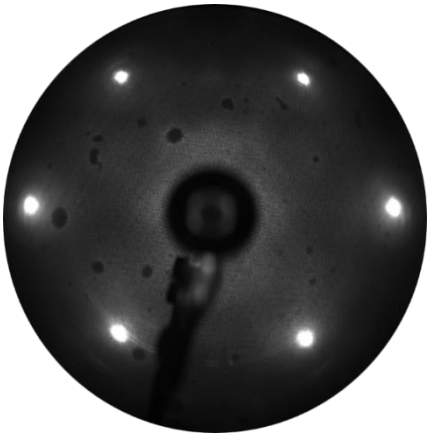

Figure 4.1. LEED pattern (Ep = 80eV) of clean Mo(110) surface.

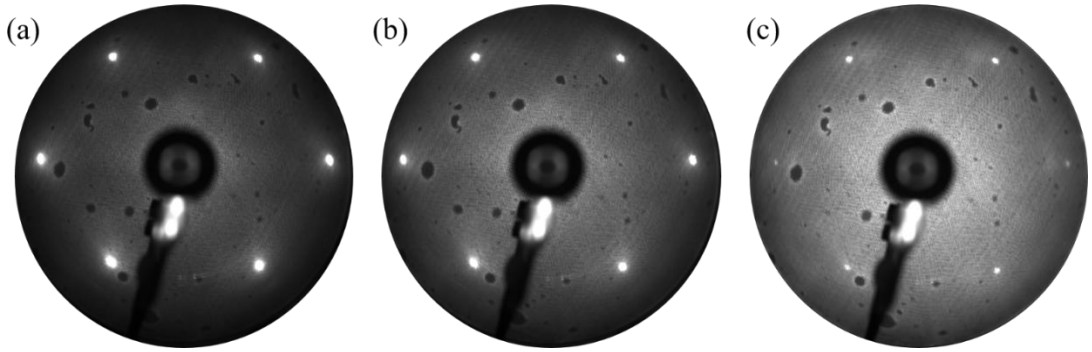

Figure 4.2. LEED patterns (Ep = 80eV) of Mo(110) surface after B deposition at room temperature for (a) 20 min, (b) 40 min and (c) 110 min.

The LEED pattern of Mo(110) surface after B deposition at room temperature remained the same as the clean surface with the change of background. When the increase of B deposition time from 20 min to 110 min, the background became more diffused and the diffracted spots for Mo got weaker which is shown in Figure 4.2. This background diffusion was occurred due to the disordered state of B on Mo(110).

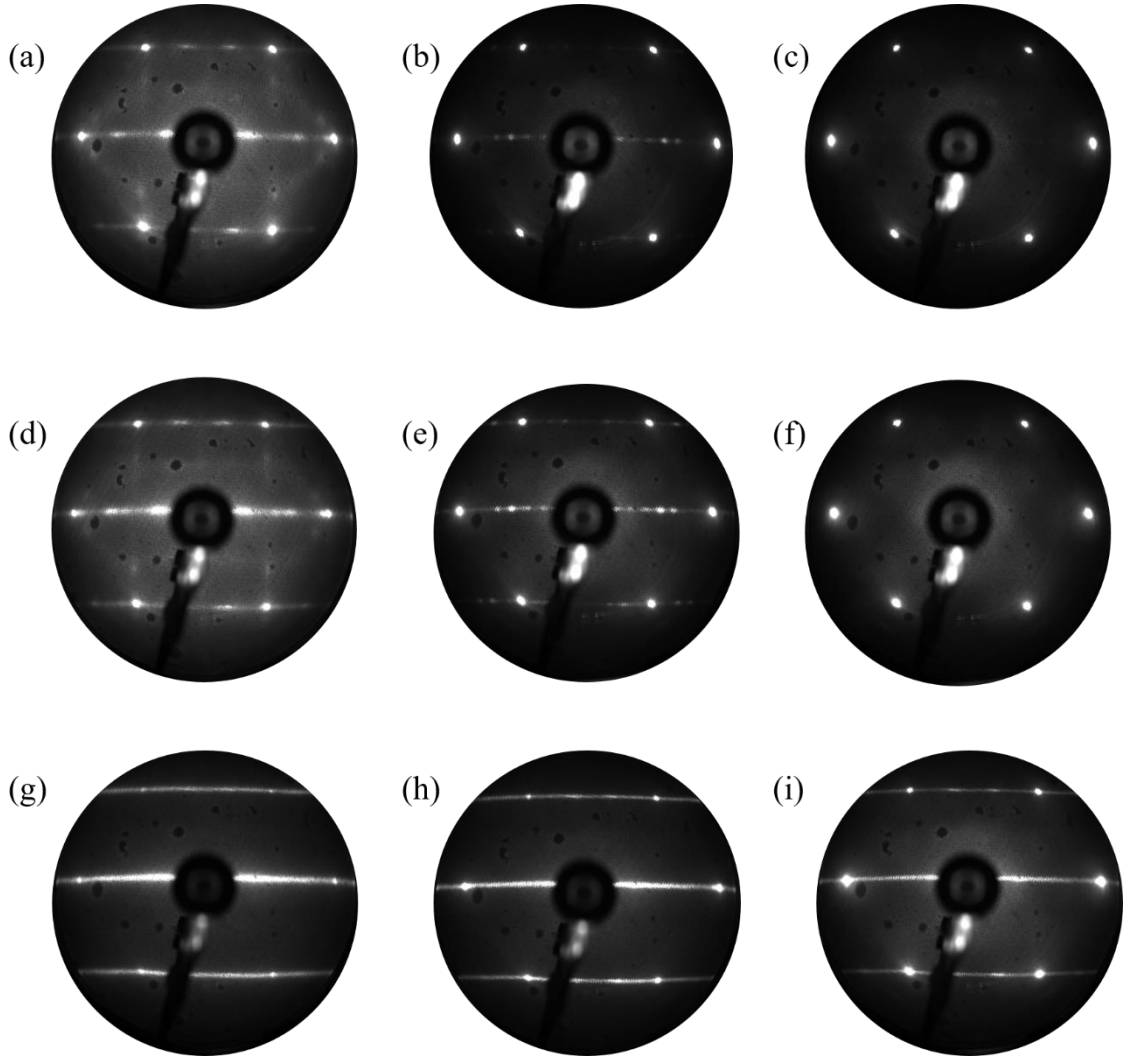

Figure 4.3. LEED patterns (Ep = 80eV) of B deposited Mo(110) surfaces after annealing at 800 K, 1200 K, and 1500 K for different deposition times.[Case I: B deposited for 20 min and subsequently annealed at (a) 800 K, (b) 1200 K and (c) 1500 K. Case II: B deposited for 40 min and subsequently annealed at (d) 800 K, (e) 1200 K and (f) 1500 K. Case III: B deposited for 110 min and subsequently annealed at (g) 800 K, (h) 1200 K and (i) 1500 K.]

Then, these B deposited Mo(110) substrates were annealed at different temperatures (800 K, 1200 K, and 1500 K). B was deposited for 20 min, 40 min, and 110 min on Mo(110) [Consider the samples prepared by 20 min, 40 min and 110 min B deposition on Mo(110) as case I, case II and case III, respectively]. When annealed at 800 K, comparatively weak streaks with some distinct spots appeared along [$1\bar{1}0$] and [001] directions for case I and case II (Figure 4.3(a,d)) and for case III, streaks were noticed only along [$1\bar{1}0$] direction with obscuring the diffracted spots for Mo atoms (Figure 4.3(g)). With the increase of annealing temperature to 1200 K for case I and case II, streaks along [001] direction disappeared, and distinctive spots became visible along [$1\bar{1}0$] direction (Figure 4.3(b,e)). These new diffracted spots are comparatively more clear for 40 min deposition time. The substrate with higher deposition time (case III) again exhibited streaks along [$1\bar{1}0$] direction relatively weaker than the prior case, which is shown in Figure 4.3(h). Furthermore, annealing at 1500 K diffused B atoms into the bulk Mo crystal as the spots became disappeared and the p(1×1) structure formed for the case I and case II. This ordered structure was the same as clean Mo(110) which is shown in Figure 4.1. Streaks were still apparent but weaker for case III, and diffraction spots for Mo atoms turned sharper (Figure 4.3(i)). These results indicate that B coverage on Mo(110) surface plays a strong role in forming ordered structure on surface.

4.3.2 Scanning tunneling microscopy (STM)

The cleanliness of Mo(110) surface was also confirmed from STM measurements, as shown in Figure 4.4. Atomically flat terrace with the step height of ~2.1 Å was observed from the line profile which is shown in Figure 4.4(b). Obtained step height is close to the calculated value of step height of Mo(110) (2.23 Å), indicating the clean state of the substrate.

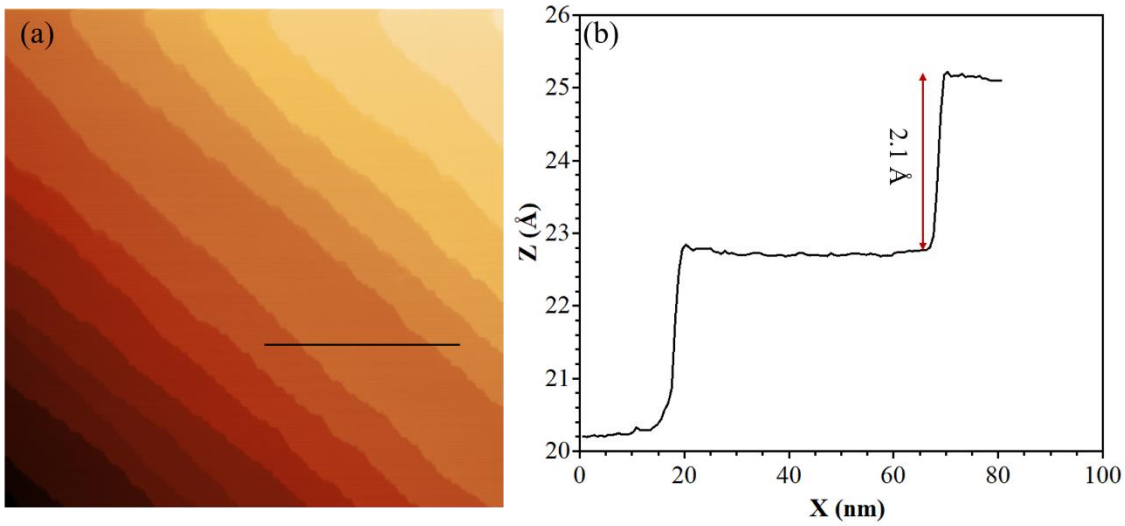

Figure 4.4. (a) Large scale (200nm×200nm) STM topographic image of clean Mo(110) surface and (b) the line profile of black line marked in Figure (a).

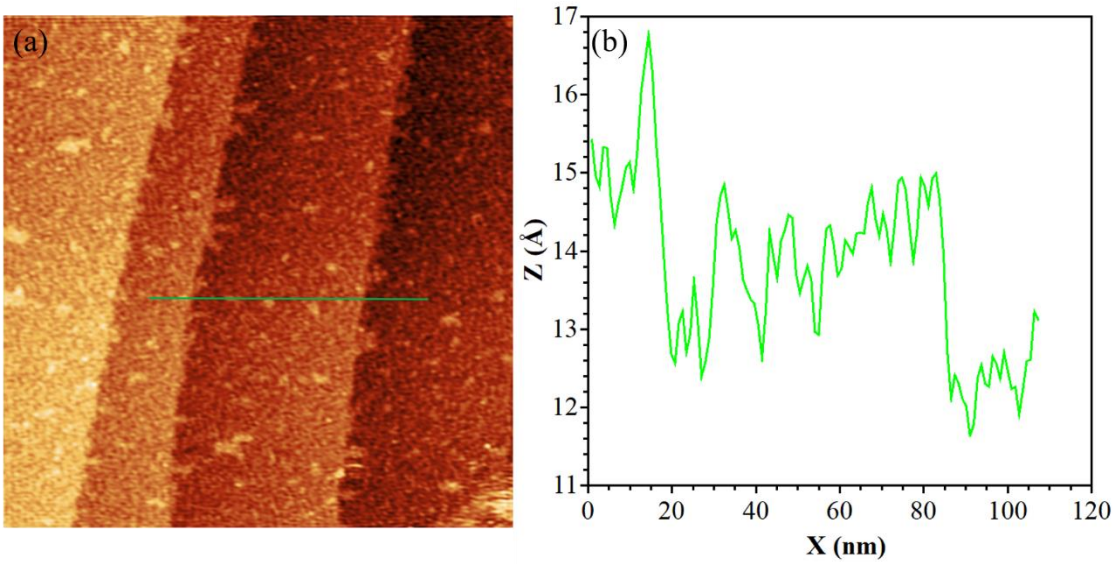

Figure 4.5. Large scale (200nm×200nm) STM topographic image of (a) B adsorbed Mo(110) surface at room temperature and (b) the line profile of green line marked in Figure (a).

On clean Mo(110) surface, B was deposited for 40 min at room temperature. It was found from the STM topographic image of that B covered Mo(110) surface that substrate was completely covered by randomly distributed B atoms which is shown in Figure 4.5(a).

The line profile in Figure 4.5(b) shows that B atoms scatter over the surface arbitrarily with different heights. This disordered state of B on Mo(110) leads to the background diffusion, which coincides with the LEED observations.

Thereafter, the substrate covered with B atoms was annealed at 800 K. It is observed from STM image which is shown in Figure 4.6(a), that very small B islands with a height around 2 Å form on the surface. Those islands are scattered almost over the substrate. In Figure 4.6(b), high resolution STM image reveals that B atoms assemble in ordered position in those small islands as indicate by the brighter lines, but some B atoms still orient in random directions, which are appeared as intermediate brighter spots. Hence, this leads to generate LEED pattern consisting of bright and very weak streaks along [1$\bar{1}$0] and [001] directions, respectively (inset of Figure 4.6(b)).

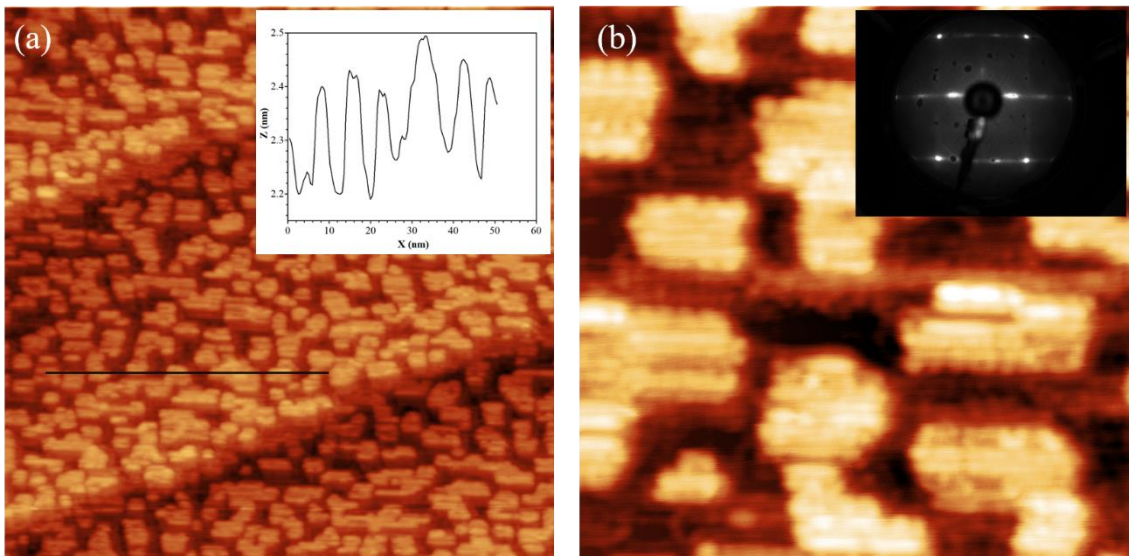

Figure 4.6. (a) Large scale (100nm×100nm) and (b) High resolution (20nm×20nm) STM topographic images of B deposited Mo(110) surface for 40 min followed by annealed at 800 K. [The inset of Figure 4.6(a) showing the line profile of black line and inset of Figure 4.6(b) showing LEED pattern (Ep = 60 eV) of that B deposited Mo(110) surface after annealing at 800 K indicating the origination of ordered structure]

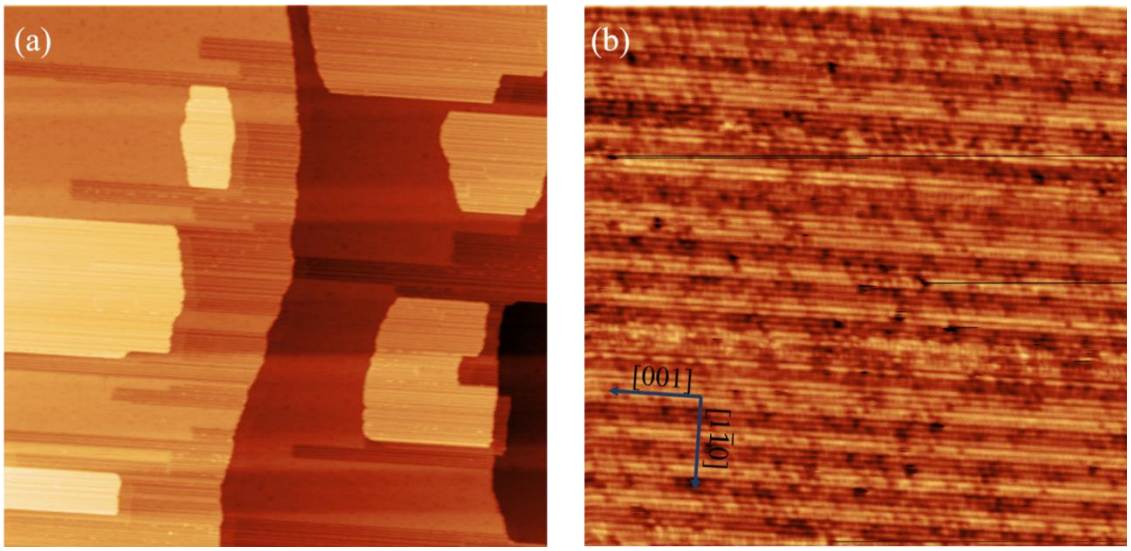

Figure 4.7. (a) Large scale (200nm×200nm) and (b) High resolution (35nm×35nm) STM topographic images of B deposited on Mo(110) surface for 40 min followed by annealing at 1200 K.

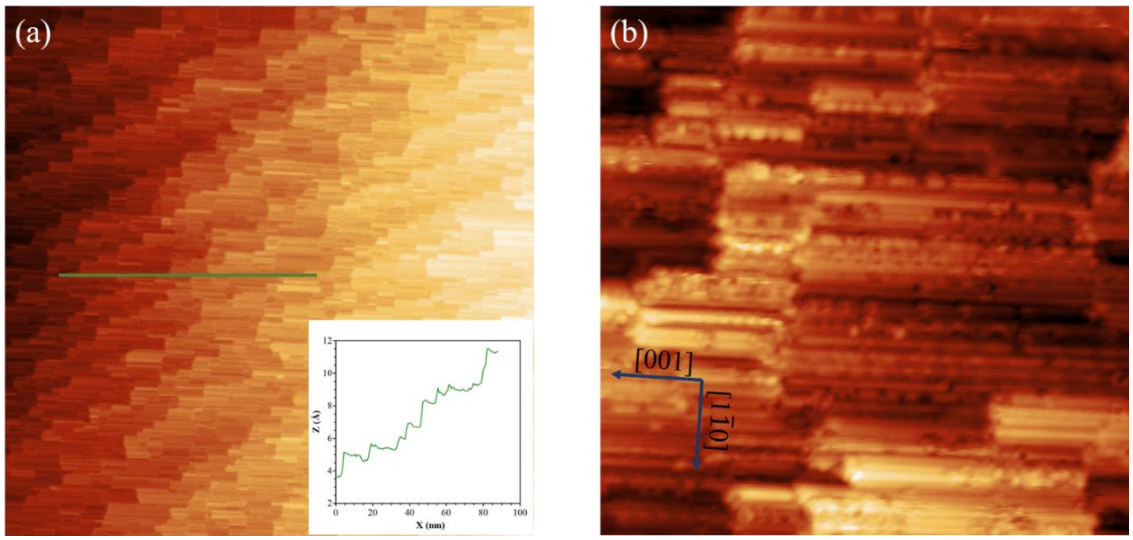

Figure 4.8. (a) Large scale (200nm×200nm) and (b) High resolution (30nm×30nm) STM topographic images of B deposited Mo(110) surface for 110 min followed by annealed at 1200 K.[Inset of Figure 4.8(a) is showing the line profile of green line marked in Figure]

Moreover, annealing the substrate at 1200 K after B deposition for 40 min, large scale STM image shown in Figure 4.7(a) shows that surface is almost covered with perfectly ordered structure indicating the growth of ordered B structure on Mo(110) surface. It can be seen from high resolution STM image as shown in Figure 4.7(b) that one type of structure consisting of parallel chains along [001] direction is formed on B covered Mo(110) surface. Therefore, a B overlayer grown on Mo(110) forms a single structural phase. It is observed from the closer inspection of that single phase B structure that parallel chains assembled along [001] direction comprise of various brightness levels, which might be due to the different number of B atoms along the chains. Moreover, the inter-distance between the stripes is found to be 4±0.3 Å.

In addition, when B deposition was continued for 110 min on Mo(110) followed by annealing at 1200 K, the surface was found to be completed covered by B atoms in multiple layers which is shown in Figure 4.8(a). From the high resolution STM image (Figure 4.8(b)), it is evident that B atoms are oriented in ordered position comprising stripes along [001] direction similar to the condition in which B deposited for 40min and annealed at 1200 K. However, in this case, B stripes formed in several layers on Mo(110) surface. For this reason, no distinguishable spots were visible in LEED pattern for higher B coverage (Figure 4.3(h)).

Structure determination from LEED and STM:

Annealing the sample after B deposition for 40 min at the temperature around 1200 K, LEED pattern changed from p(1×1) structure with an obscure background to a pattern containing discernable spots along [$1\bar{1}0$] direction. Besides, a close investigation of this LEED pattern of B/Mo(110) comparing with the p(1×1) LEED pattern of clean Mo(110) surface revealed that a superstructure with matrix notation, $\begin{pmatrix} 0 & -9 \\ 1 & 1 \end{pmatrix}$ was formed. The unit cells of clean Mo(110), and the superstructure formed for B/Mo(110) are shown in real and reciprocal space in Figure 4.9.

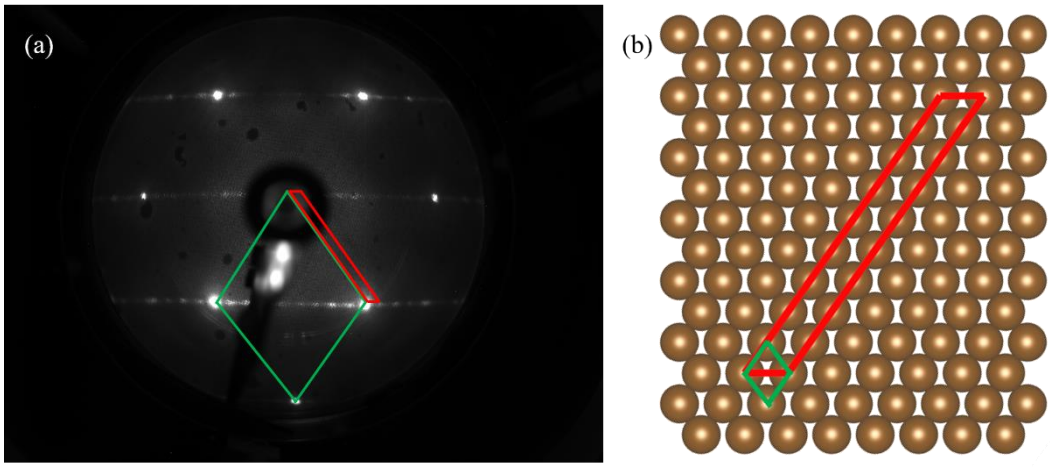

Figure 4.9. (a) LEED pattern ((Ep = 106 eV) of B deposited Mo(110) surface followed by annealed at 1200 K exhibiting the unit cells of clean Mo(110) surface and superstructure formed for B/Mo(110) and (b) Schematic of corresponding unit cells in real space.

[The unit cells of clean Mo(110) and superstructure for B/Mo(110) are indicated by green and red parallelogram, respectively in reciprocal space (Figure 4.9(a)) and real space (Figure 4.9(b)); Brown balls in Figure 4.9(b) resemble as Mo atoms].

The superstructure observed from the LEED pattern as shown in Figure 4.9(a) revealed that lattice constants along [001] and $[1\,\bar{1}\,1]$ directions were 3.15 Å and 24.6 Å, respectively which almost coincided with the obtained periodicities from STM image (Figure 4.7(b)); approximately 3.4 Å along the chain in [001] direction and 24.5 Å across the chains in $[1\bar{1}1]$ direction. It can be seen from STM image of B covered Mo(110) for 40 min and subsequently annealed at 1200 K that surface consists of parallel stripes along [001] direction with different brightness levels. Neither any single stripe was observed in STM image nor the darker contrast in between the chains of the STM image came from the Mo atoms; thereby, a continuous 2D B structure might be formed which is referred to borophene. The darker area between the chains resembles hexagonal hollows in borophene structure.

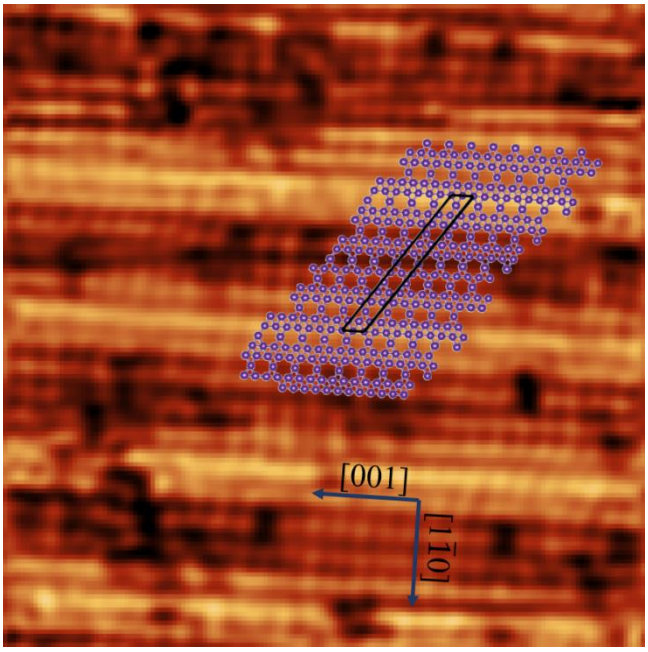

Figure 4.10. STM image of B structure on Mo(110) surface with the superimposition of atomic model of B sheet.[Black parallelogram indicates the unit cell of the structure]

Considering these facts, the formation of single phase borophene structure on Mo(110) is proposed in this study which is shown in Figure 4.10 in which atomic model of B structure is superimposed on STM image. Since 2D boron sheet showed polymorphism, numerous atomic models can be predicted based on the LEED and STM observations. In this study, a 2D B sheet is proposed to form on Mo(110) based on the observed various brightness levels of stripes along [001] direction.

As the periodicity along the chain (in [001] direction) is 3.15 Å, B-B bond along [001] is contracted by ~3% from its equilibrium value of 1.62 Å to overcome the lattice mismatching; hence, two B-B bonds match with one Mo-Mo bond in [001] direction. Furthermore, seven times the distance between neighboring nodes of B sheet (2.86 × 7 = 20.02 Å) perfectly fits with 4.5 times the lattice constant of Mo(110) (4.45 × 4.5 = 20.025 Å). Therefore, along [1$\bar{1}$1] direction B sheet contracts very slightly which is negligible. In Figure 4.11, the top view of atomic configuration of B sheet on Mo(110) surface is depicted. Therefore, it can be claimed from the STM observation along with the LEED pattern of B/Mo(110) that a triangular B sheet with 28 nodes within the unit cell is formed on Mo(110) surface, in which 5 nodes are empty and 23 are filled. Coordination numbers

for B atoms for this structure are 4 and 5. Because of possessing these coordination numbers, this type of B sheet structure is denoted as χ- type [15] structure. Thus, B sheet of χ- type structure with the hexagonal hole density, η= 5/28 can be formed on Mo(110) surface.

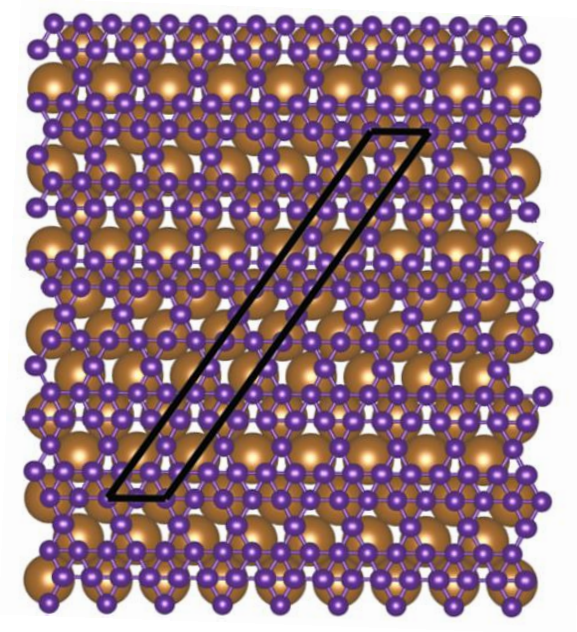

Figure 4.11. Top view of the atomic configuration of χ type B sheet on Mo(110). [Unit cell is shown by black parallelogram. Brown and purple balls resemble Mo and B atoms, respectively]

In summary, it can be manifested that direct deposition of B at room temperature followed by annealing the substrate at 1200 K forms a novel single phase planar B sheet on Mo(110) surface with which B atoms strongly interact. B atoms orient randomly on Mo(110) after deposition at room temperature. Annealing at high temperature dissolves some B atoms into the bulk, and the remaining B atoms create an ordered structure over the substrate in planner form. According to the STM measurements with the LEED observations, B atoms form a continuous 2D sheet on Mo(110) which is referred as χ-type borophene with hexagonal hole density η=5/28. Formation of new borophene structure depends on the interaction between B atoms with the underlying Mo atoms of

substrate as well as the lattice parameter matching. Origination of new phases of 2D B sheet on different substrates facilitates more opportunities to investigate those structures which may evolve fascinating physical and chemical properties for future nanoscale devices.

References

[1] Z. Zhang, A.J. Mannix, Z. Hu, B. Kiraly, N.P. Guisinger, M.C. Hersam, B.I. Yakobson, Substrate-induced nanoscale undulations of borophene on silver, Nano Lett. 16 (2016) 6622–6627. https://doi.org/10.1021/acs.nanolett.6b03349.

[2] Z. Zhang, Y. Yang, E.S. Penev, B.I. Yakobson, Elasticity, flexibility, and ideal strength of borophenes, Adv. Funct. Mater. 27 (2017) 1605059. https://doi.org/10.1002/adfm.201605059.

[3] N.A. Vinogradov, A. Lyalin, T. Taketsugu, A.S. Vinogradov, A. Preobrajenski, Single-phase borophene on Ir(111): Formation, structure, and decoupling from the support, ACS Nano. 13 (2019) 14511–14518. https://doi.org/10.1021/acsnano.9b08296.

[4] X. Sun, X. Liu, J. Yin, J. Yu, Y. Li, Y. Hang, X. Zhou, M. Yu, J. Li, G. Tai, W. Guo, Two-dimensional boron crystals: Structural stability, tunable properties, fabrications and applications, Adv. Funct. Mater. 27 (2017) 1603300. https://doi.org/10.1002/adfm.201603300.

[5] Z.H. Cui, E. Jimenez-Izal, A.N. Alexandrova, Prediction of Two-dimensional phase of boron with anisotropic electric conductivity, J. Phys. Chem. Lett. 8 (2017) 1224–1228. https://doi.org/10.1021/acs.jpclett.7b00275.

[6] S.A. Shakirova, V.A. Pleshkov, G.A. Rump, Adsorption of rare-earth metals (Tb,Dy,Er) on a Mo(110) surface, Surf. Sci. 279 (1992) 113–118. https://doi.org/10.1016/0039-6028(92)90747-T.

[7] A. Krupski, Scanning tunnelling microscopy study of Au growth on Mo(110), Surf. Sci. 605 (2011) 424–428. https://doi.org/10.1016/j.susc.2010.11.012.

[8] J. Kröger, D. Bruchmann, S. Lehwald, H. Ibach, Adsorption of lithium on Mo(110): An EELS study of the adsorbate vibrations and substrate phonons, Surf. Sci. 449 (2000) 227–235. https://doi.org/10.1016/S0039-6028(00)00058-3.

[9] M. Wiejak, M. Jankowski, I. Yakovkin, J. Kołaczkiewicz, Adsorption of Nd on the Mo(110) surface, Appl. Surf. Sci. 256 (2010) 4834–4838. https://doi.org/10.1016/j.apsusc.2010.01.112.

[10] A. Krupski, Pb on Mo(110) studied by scanning tunneling microscopy, Phys. Rev. B - Condens. Matter Mater. Phys. 80 (2009). https://doi.org/10.1103/PhysRevB.80.035424.

[11] M.L. Ernst-Vidalis, E. Bauer, Hydrogen on Mo(110): Adsorption and electron

stimulated H+ desorption, Surf. Sci. 215 (1989) 378–384. https://doi.org/10.1016/0039-6028(89)90267-7.

[12] S. Thomas, T.W. Haas, LEED/Auger spectroscopy study of the adsorption of alkali metals on Mo(110), J. Vac. Sci. Technol. 9 (1972) 840–843. https://doi.org/10.1116/1.1317798.

[13] T.T. Magkoev, A.M. Turiev, N.I. Tsidaeva, D.G. Panteleev, G.G. Vladimirov, G.A. Rump, Adsorption of boron on a Mo(110) surface, J. Phys. Condens. Matter. 20 (2008) 485007. https://doi.org/10.1088/0953-8984/20/48/485007.

[14] T.B. Fryberger, J.L. Grant, P.C. Stair, Adsorption of boron on molybdenum(100) and its effect on chemisorption of carbon monoxide, ethene, propene, and 3,3,3-trifluoropropene, Langmuir. 3 (1987) 1015–1025. https://doi.org/10.1021/la00078a024.

[15] X. Wu, J. Dai, Y. Zhao, Z. Zhuo, J. Yang, X.C. Zeng, Two-dimensional boron monolayer sheets, ACS Nano. 6 (2012) 7443–7453. https://doi.org/10.1021/nn302696v.

CHAPTER 5: CONCLUSIONS AND FUTURE PROSPECTS

5.1 Conclusions

Investigation of B adsorption on different substrates will help to understand structure formed on the surface and the properties of the interface which are considered very crucial for the applications in future nanoscale devices. The research works presented in this thesis are focusing on determining the B structures over two refractory metal surfaces; W(100) and Mo(110). Both of these surfaces show interesting phenomena on the growth of B. W and Mo, both possess BCC crystal structure. In BCC structure, (110) surface is the most stable faces due to having the highest atomic density, and (100) surface is comparatively less stable than (110) but more stable than (111) surface. The concluding results of B on W(100) and B on Mo(110) surface are summarized here.

For B adsorption on W(100) surface, a new superstructure of c(2×2) appeared in LEED pattern after annealing the substrate at higher temperatures, which indicated the formation of ordered structure because of B atoms placed in crystallographic positions. The detailed structural analysis from I(E) results obtained by LEED manifested that B atoms positioned at four-fold hollow site of W(100) surface. The lowest Rp factor of 0.23 was found for c(2×2) superstructure by LEED calculation, and in the best-fit model, one B atom was placed in the unit cell of the superstructure and each B atom bonded with four neighboring W atoms of the top layer and one W atom of the underlying layer which was beneath B atom. Thereby, it was found from LEED analysis that a metal rich surface alloy, W_2B, was formed at the surface. Some small clusters containing few unit cells with the lattice constant of 4.6±0.2 Å along both [$\bar{1}$10] and [110] directions were noticed in the high resolution STM image. Comparing this measured lattice parameter of B/W(100) with the lattice constant of clean W(100) surface from STM results clearly confirmed the formation of c(2×2) superstructure upon B deposition. In addition, it was revealed from STM that the ordered structure maintained 4-fold symmetry, which is in agreement with LEED analysis. Furthermore, the B 1s peak position for W(100) c(2×2)-B was found at the binding energy of 187.8 eV by XPS measurements, and B 1s peak at this binding energy indicated the formation of low B concentrated compound at the surface. In addition, the observation of small peak intensity of B 1s confirmed that fewer number of

B atoms was existed on W(100) surface suggesting the origination of metal rich tungsten boride compound at surface as well.

In the following research work, depositing B on Mo(110) surface at room temperature generated p(1×1) surface with obscuring the LEED background due to the random orientation of B over this surface. Annealing at high temperature, ~1200 K, some B atoms dissolved into the bulk, and the remaining B atoms formed an ordered structure over the substrate in a planar form which was revealed from LEED and STM measurements. With the detailed analyzes of STM results combined with LEED pattern, it was evident that continuous 2D B sheet was formed on Mo(110) and it was referred as χ- type borophene with hexagonal hole density η=5/28. This new phase of borophene structure strongly depends on the presence of interaction between B and Mo atoms as well as the lattice parameter matching.

Recently formation of single layer B sheets, borophene, on metal surfaces have attracted tremendous interest. From these two researches, it is apparent that origination of 2D B sheet is dependent on substrates as well as their crystalline faces. B atoms on W(100) surface prefer to form tungsten-boride alloy despite forming any B sheet. The reason behind this would be the stable adsorption of B on the hollow site. According to the theoretical calculation [1], the adsorption energy of B on the hollow site is calculated to be 4.83 eV, which is the highest among B on low index surfaces of W. On the other hand, the diffusion barrier of B into the bulk on W(100) is low compared with that along the surface. Moreover, the high temperature annealing, which would be necessary to initiate the formation of B sheets, results in the diffusion of B into bulk. Thus the high adsorption energy associated with the low diffusion barrier into bulk makes it unlikely to produce B sheets on W(100). However, B atoms form a 2D overlayer on Mo(110)surface, which is the most stable low-index surface of BCC crystal. It was reported earlier that for W(110), the required diffusion energy for B atoms is higher to diffuse into the bulk compared to the diffusion along the surface [1]. In addition, B atom adsorbed at a distance, 2 Å, away from the W(110) surface is found to be in favorable condition in terms of energy [2]. Theoretically, it was predicted that W(110) surface is prominent candidate for the formation of B sheet [3]. As the Mo(110) surface shows almost similar properties of

W(110) surface, it is feasible to form a single layer B sheet on Mo(110). B atoms prefer to reorient along the Mo(110) surface and forms a single layer B sheet upon annealing the substrate at high temperature rather diffusing into the bulk because of the high diffusion barrier. Hence, the surface properties play a vital role on the formation B structure on any specific substrate.

5.2 Future prospects

The findings of the research work reported in this thesis make a small effort in realizing the surface and interfacial properties of B on two refractory metal surfaces. Till now, it is very challenging to synthesize 2D B sheets experimentally while theoretically it was predicted that B sheets could form on metals or metal-borides [4]. Many more researches are required to find the suitable substrates for the growth of single layer B sheet with intriguing properties. So far, the successfully synthesized B sheet on several substrates are reported by STM measurement with theoretical calculations. Thus, determining the B covered surface structure by LEED can give strong evidence of B structure over the substrate.

Moreover, it was reported that 2D B sheet on Ag(111) surface can easily get oxidized in ambient conditions [5] which makes B sheet unsuitable for application. In future, it will be interesting to observe the chemical properties of B sheet on Mo(110) in UHV and ambient conditions which are not presented here.

Hydrogenating borophene by atomic hydrogen can prevent oxidation of borophene as reported by Li et al. [6]., 'Borophane' prepared by exposing B sheet to atomic hydrogen may change the surface structure. The new structure can be observed and analyzed by LEED as well in future; along with, the chemical properties of the interface can be obtained from XPS which will give valuable information about the surface's stability against oxidation.

Therefore, analyzing B structure on several substrates can open the path to obtain the best substrate and growth conditions for borophene which will have great impact in future applications.

References

[1] C. Lu, J. Yang, X. Lei, J. Huang, Z. Ye, S. Chen, Y. Zhao, First-principles calculations on adsorption-diffusion behavior of Boron atom with tungsten surface, Comput. Mater. Sci. 183 (2020) 109908. https://doi.org/10.1016/j.commatsci.2020.109908.

[2] S. Dorfman, R.R. Braga, K.C. Mundim, D. Fuks, Simulations of initial stages of boron deposition on (110) tungsten surface, Surf. Sci. 566–568 (2004) 676–682. https://doi.org/10.1016/j.susc.2004.05.128.

[3] Z.H. Cui, E. Jimenez-Izal, A.N. Alexandrova, Prediction of two-dimensional phase of boron with anisotropic electric conductivity, J. Phys. Chem. Lett. 8 (2017) 1224–1228. https://doi.org/10.1021/acs.jpclett.7b00275.

[4] Y. Liu, E.S. Penev, B.I. Yakobson, Probing the synthesis of two-dimensional boron by first-principles computations, Angew. Chemie. 125 (2013) 3238–3241. https://doi.org/10.1002/ange.201207972.

[5] B. Feng, J. Zhang, Q. Zhong, W. Li, S. Li, H. Li, P. Cheng, S. Meng, L. Chen, K. Wu, Experimental realization of two-dimensional boron sheets, Nat. Chem. 8 (2016) 563–568. https://doi.org/10.1038/nchem.2491.

[6] Q. Li, V.S.C. Kolluru, M.S. Rahn, E. Schwenker, S. Li, R.G. Hennig, P. Darancet, M.K.Y. Chan, M.C. Hersam, Synthesis of borophane polymorphs through hydrogenation of borophene, Science. 371 (2021) 1143–1148. https://doi.org/10.1126/science.abg1874.

APPENDIX

Interfacial magnetic behaviors and chemical states of Fe grown on MoS_2

Magnetic and chemical properties of ultrathin Fe films on molybdenum disulfide (MoS_2) are investigated using magneto-optic Kerr effect (MOKE) and X-ray photoemission spectroscopy (XPS). A magnetization hysteresis loop is found after nominal 10 Å of Fe deposition on MoS_2 at room temperature. The thickness dependent MOKE measurement evaluates that the magnetic dead layer (MDL) exists up to ~2 Å of Fe on MoS_2 due to the interaction between Fe and MoS_2. X-ray photoemission spectroscopy (XPS) shows small peak shifting for Mo3d and S2p peaks towards lower binding energies with initial Fe deposition, indicating the modification of surface band bending. Fe2p peaks for lower thickness of Fe is significantly broader than those of higher thickness, which is attributed to the coexistence of metallic and ionic Fe in the film. The presence of ionic Fe, localized at the interface, indicates strong interactions between Fe and MoS_2, and the existence of chemical bonding at the interface is corroborated with the formation of MDL.

1. Introduction

MoS_2 has been considered as one of the most promising materials due to having unique physical and chemical properties; belongs to a family of a semiconducting transition metal dichalcogenide (TMDC). Single layer of MoS_2 with a direct bandgap of 1.8 eV overcomes the limitation of zero bandgap graphene and makes this 2D material applicable in future optoelectronic devices [1–3]. In addition, its ultrafast saturable absorption, flexibility, catalytic activities make this a prominent material for the applications in solar cell, gas sensors, storage, flexible electronics [4–6]. In MoS_2, a single layer of Mo is covalently bonded with two S layers comprising trilayers which are stacked on each other by van der Waal forces. Generally available MoS_2 is found in two phases, 2H and 3R phases. 2H-MoS_2 consists of two layers of S-Mo-S per unit cell forming hexagonal symmetry with trigonal prismatic coordination which is found to be more stable than 3R-

MoS_2 and semiconducting in nature whereas 3R-MoS_2 contains three S-Mo-S layers per unit cell comprising rhombohedral symmetry with trigonal prismatic coordination [4,7,8]. In addition, metallic phase is also found in single layer MoS_2 having octahedral coordination that is denoted as 1T-MoS_2 [5,7,8]. Many researches were carried out to investigate the magnetic properties of MoS_2. As pristine MoS_2 is diamagnetic in nature, several attempts have been carried out to induce ferromagnetism in MoS_2, such as, introducing strain or defects, hydrogenation, or transition metal doping [6,8–10]. Instead of these, combination of magnetic material with 2D MoS_2 is considered an effective method for the applications in spintronic devices [11]. However, the deposition of transition metal on MoS_2 substrate can exhibit different congregations depending on the interaction between adsorbate and adsorbent or adsorbate and adsorbate [12]. Furthermore, metal/MoS_2 interface plays a crucial role as the high anisotropic behavior of MoS_2 leads to the unusual reactivity of surface and formation of Schottky barrier [13]. In addition, the interaction at metal/MoS_2 may lead to the reduction of ferromagnetic order of metal, forming no magnetic moment at the interface which is known as magnetic dead layer (MDL) [14]. The formation of MDL at the interface has adverse effect on charge and spin transportation between metal and semiconductor surface [15]. The interface of metal and MoS_2 plays an important role for future electronic device technologies. It was found that the growth mode of Pd, Au and Ag on monolayer of MoS_2 was different as Pd on MoS_2 formed a uniform layer and, Au and Ag showed the tendency to form nanometer sized clusters on MoS_2 which created inhomogeneity in contacts [12]. Structural transformation of MoS_2 from 2H to 1T phase was observed by nonmagnetic transition metal (Re) doping on MoS_2 nanosheets which introduced ferromagnetism in MoS_2 [16]. In addition, the interfacial reactions between metal and MoS_2 depend on the deposition condition. Metals with low work function (Cr, Sc) reacted with MoS_2 at ultrahigh vacuum (UHV) condition whereas, Au formed van der Waals interface with MoS_2 at different deposition conditions [17]. Therefore, magnetism and structural configuration at the interface of metal/semiconductor have become a major concern for heterostructure devices.

Ultrathin MoS_2 is a possible candidate for spin filter materials when contacted with ferromagnetic materials due to its large spin-orbit splitting since MoS_2 contains the heavy

element (Mo) and its inversion symmetry is broken at the interface. A theoretical calculation for Fe/MoS_2 indicated that the strong bonding between S-Fe drove the formation of single layer Fe film on MoS_2, but it was also expected that this strong bonding drastically transformed the electronic structure of MoS_2 [18]. STM observation showed that Fe did not form single layer films but aggregate into 3d nanoparticle at the very thin films (<10 ML) which indicated that the formation of single layer Fe film and the ferromagnetic order in the very thin film limit was unlikely [10]. In this study, we observed the magnetic and chemical properties of *in-situ* prepared ultrathin Fe films on MoS_2 which were studied by MOKE and XPS, respectively.

2. Experiment

Experiments were carried out in UHV chambers. All measurements were performed *in-situ* without capping layers on samples. Magnetic properties of Fe/MoS_2 were investigated at room temperature by MOKE measurements with a magnetic field along the longitudinal direction. A laser diode with a wavelength of 635 nm was used as a light source, which was inclined 45˚ to the sample surface. A schematic view of MOKE measurements is shown in Figure A.1.

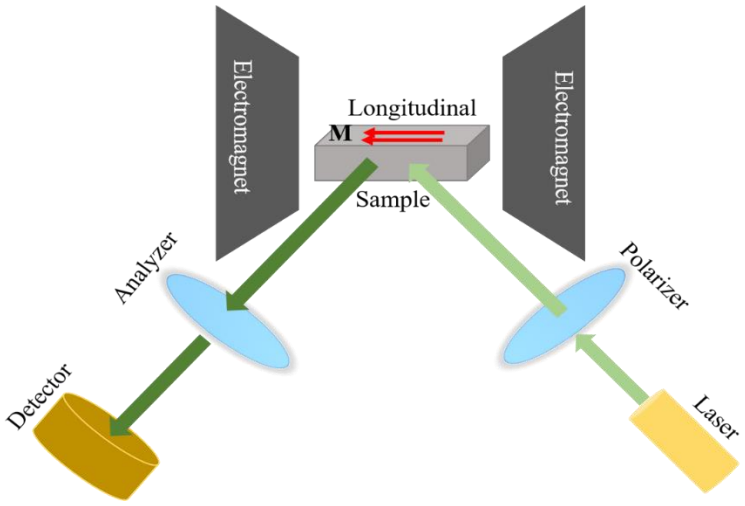

Figure A.1. Schematic view of MOKE setup.

For MOKE measurement, we used thin MoS_2 transferred on a clean SiO_2 substrate by mechanical method under ambient condition because thick MoS_2 crystal did not give good reflection of laser light hindering MOKE measurements with good signal-to-noise ratio. Sample preparation method is shown in Figure A.2.

Figure A.2. Experimental setup for transferring MoS_2 onto glass substrate.

For XPS, we used MoS_2 crystal. The deposition of Fe on MoS_2 was conducted using an electron beam evaporator. XPS was utilized to examine chemical interactions at the interface of Fe/MoS_2 at room temperature in UHV with a base pressure of ~2×10^{-10} Torr. XPS was conducted by using PHOIBOS100 analyzer and a non-monochromatic Mg K_α X-ray source with a photon energy ($h\upsilon$) of 1253.6 eV. The incident angle of the photon was 45° from the surface normal and the emitted electrons from the surface normal was collected with an acceptance angle of 8°. For both experiments, the deposition rate of Fe was approximately 1Å/min, which was monitored by a quartz crystal microbalance (QCM).

3. Results and discussion

3.1 Magnetic properties

In Figure A.3, magnetization curves for various amounts of deposited Fe on MoS_2 are shown. First hysteresis loop was become observable at the thickness of Fe, t_{Fe}, of 10 Å. The Fe thickness indicates the average thickness of Fe. With the increase of Fe thickness, the Kerr rotation as well as the coercivity increased. The curves showed high remanence magnetization above 10 Å, which indicated that the Fe films on MoS_2 had a large in-plane magnetic anisotropy. The hysteresis loops were not rectangular shape, which is in agreement with the nano particle formation that shows small uniaxial anisotropy along the surface [19].

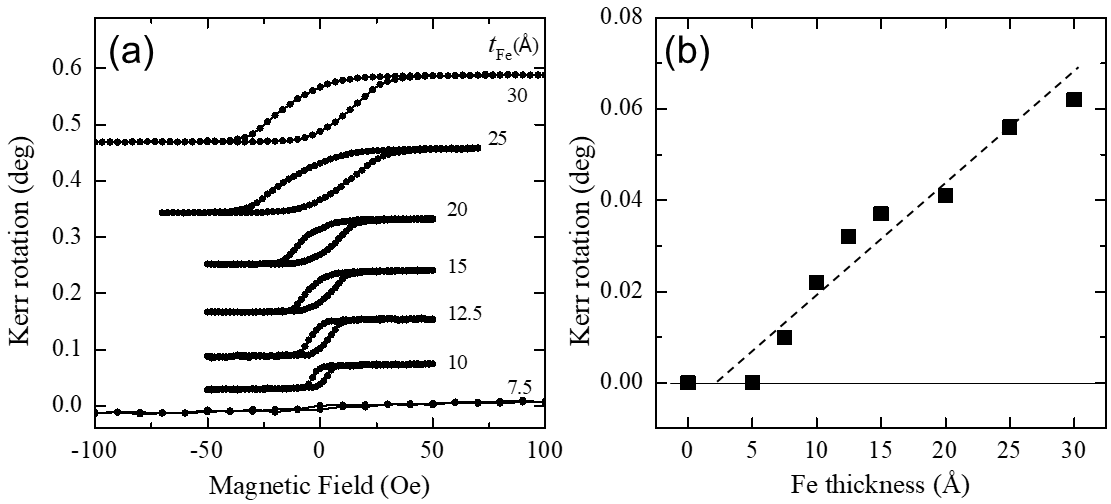

Figure A.3. (a) Magnetization curves for different thickness of Fe on MoS_2 measured by MOKE; (b) Kerr rotation angle as a function of Fe thickness indicating the MDL. [The straight line in Figure (b) indicates the linear fitting]

The absence of hysteresis below 10 Å is related to magnetic phase transition between ferromagnetic and paramagnetic (or superparamagnetic) states because of the thermal

effects and MDL formation due to the presence of non magnetic material at the interface. MDL can be determined by the thickness dependency of Kerr rotation. Within the light penetration depth, the Kerr rotation is approximately proportional to the thickness of ferromagnetic material. In the case of no MDL, Kerr rotation should increase linearly with deposition of Fe approximately up to ~100 Å [20]. A plot of Kerr rotation as a function of the Fe thickness is shown in Figure A.3(b). Note that the steep drop around 7.5 Å is due to the low Curie temperature for the thinner films. When the linear extrapolation of these points coincides zero Kerr rotation at the thickness of Fe 0 Å, the deposited entire Fe film on MoS_2 is in ferromagnetic phase and no formation of MDL at the interface [15,20]. However, the linear extrapolation of these points intersected the nominal Fe thickness at ~2 Å for Fe/MoS_2. Therefore, Fe layer was magnetically dead for the deposition of Fe up to 2 Å for MoS_2.

The formation of MDL at the interface of Fe/MoS_2 is due to the presence of interaction between Fe and MoS_2 at lower thickness of Fe. From previous STM results, Fe on MoS_2 follows the Volmer-Weber growth mode due to the absence of strong interaction between substrate and metallic atoms at MoS_2 terraces while the natural defects on MoS_2 strongly interact with Fe atoms and act as nucleation sites for the formation of nanoparticles [11,21]. Thus, the small interaction between Fe and MoS_2 would cause Fe-S (or Mo) bond formation at the interface and evolve formation of compounds responsible for originating MDL at the interface for lower amount of Fe deposition.

3.2 XPS analysis

XPS measurements were carried out to investigate the interactions between Fe and MoS_2. The Mo3d, S2p and Fe2p spectra are depicted in Figure A.4. Kinetic energies for Mo3d, S2p and Fe2p photoelectron is approximately 1024, 1092 and 547 eV, respectively, corresponding to photoelectron mean free paths of 16.5, 17.3, 10.4 Å, respectively [22]. We fitted the XPS curves to elucidate the change of peak intensities and peak positions with the deposition of Fe on MoS_2 substrate. We used Voigt function except metallic

Fe2p spectra to fit spectra, and for metallic Fe2p we used the convolution of Gaussian and Donich-Šunjić function to account for the asymmetric peak shape.

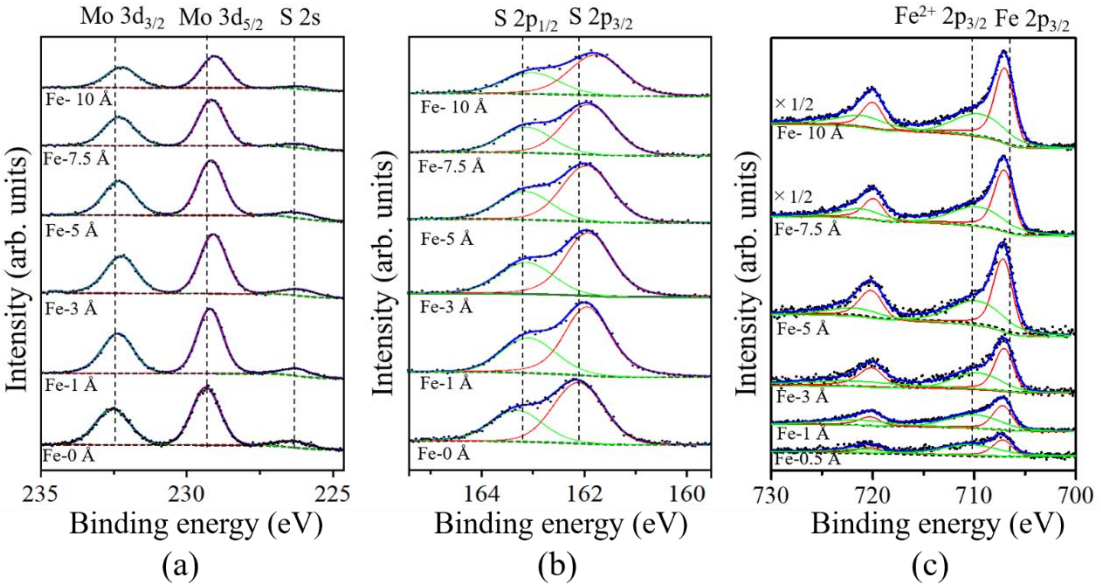

Figure A.4. XPS spectra (black dots) of (a) Mo3d, (b) S2p and (c) Fe2p with the deposition of various thickness of Fe on MoS_2 substrate. Lines show the fitting results.

In Figure A.5, peak positions for Mo3d, S2p and Fe2p are plotted as a function of Fe thickness. It was observed that Mo3d as well as S2p peaks rapidly moved towards the lower binding energies by 0.2 eV with the deposition of 1 Å Fe which is depicted in Figure A.5 (a) and (b). The binding energies for both Mo3d and S2p kept shifting to lower binding energy gradually with further increase of the Fe deposition. These results showed that the binding energy shift was mostly generated by the change of band bending due to the formation of Schottky barrier height.

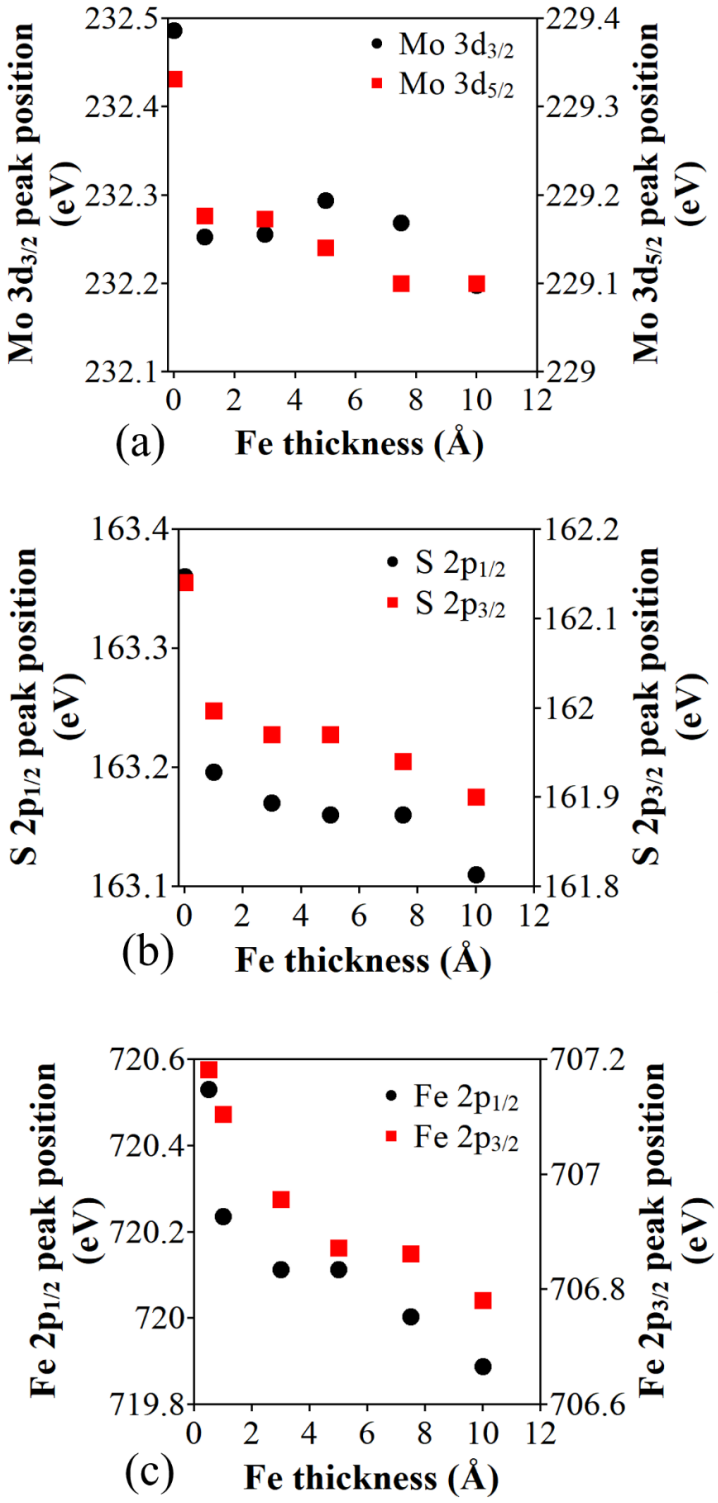

Figure A.5. Plot of peak positions for (a) Mo3d, (b) S2p, and (c) Fe2p core levels with the increase of Fe thickness on MoS_2.

The Fe2p peak showed slight broadening for lower coverage of Fe. Beside with the main peak at ~707 eV which originated from the metallic Fe, a shoulder peak existed at higher binding energy at around 710 eV, which indicated the presence of an Fe compound. Figure A.4(c) shows deconvoluted spectra of Fe2p considering the coexistence of metallic and ionic states of Fe. Normalized spectra with the background subtraction of Fe2p and fitting result for 1 Å Fe thickness are shown in Figure A.6(a). For the higher thickness of Fe (3 Å to 10 Å), the peak shapes are quite similar, while the peak shapes are broadened at lower thickness of Fe (0.5-1 Å) and this broadening indicates the roughness and the strong bonding between Fe and S(or Mo) [10]. The ratio between the ionic and the metallic peaks for $Fe2p_{3/2}$ decreased from 1.63 to 0.69 with the increase of Fe deposition from 0.5 to 10 Å as shown in Figure A.6(b), suggesting formation of Fe compounds confined at the interface of Fe/MoS_2 for lower thickness of Fe. As the metallic phase of Fe became dominant Fe at higher thickness of Fe, these findings demonstrate the reduction of interactions between Fe and MoS_2 at higher coverage. Thus, it can be concluded that the deposited Fe mostly remained in metallic Fe state with a small interaction resulting in Fe-S (or Mo) bonding at the interface of Fe/MoS_2 at low thickness of Fe [10,13,19].

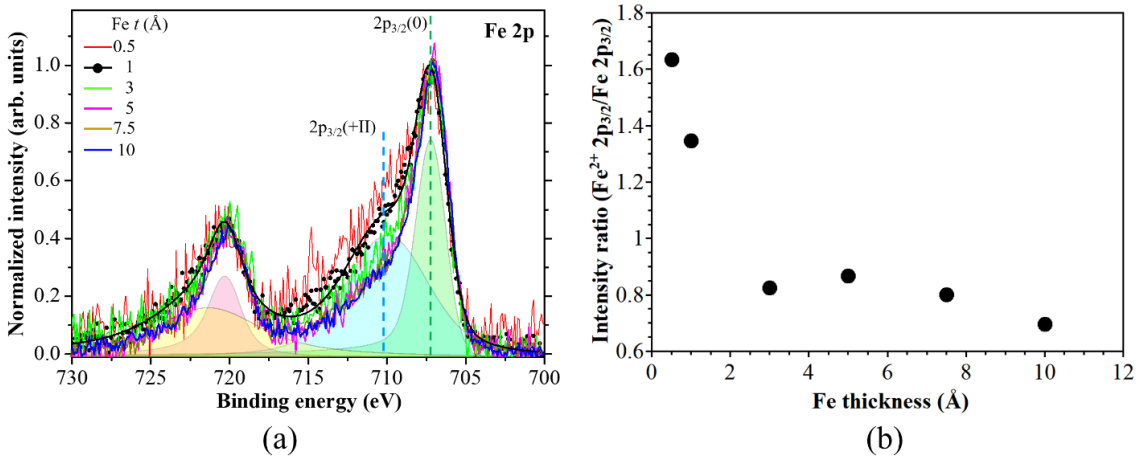

Figure A.6. (a) Normalized XPS spectra of Fe2p core level region for various Fe and (b) Ratio of intensities between ionic and metallic $Fe2p_{3/2}$ peaks as a function of Fe thickness.

The peak intensities for Mo3d and S2p as a function of Fe coverage is shown in Figure A.7. Mo3d and S2p peak intensities increased with the initial increase of Fe thickness, upto ~3 Å. Subsequently started to decrease at high amount of Fe deposition. A simple overlayer growth of Fe did not explain the unusual invariant of the substrate photoelectrons at the initial Fe deposition. Such intensity changes upon Fe deposition have been found on a graphene surface [23]. XPS results can partly be explained by Fe nucleation, intercalation and backscattering effect. The Fe nucleation started at the initial Fe deposition, which was followed by growth along the surface with keeping the Fe island height. The Fe nucleation started at defect sites of MoS_2, and the defect sites also might act as the intercalation. Furthermore, different backscattering efficiency between Fe and MoS_2 gave enhanced MoS_2 intensity after Fe deposition.

The decrease of Mo3d intensity was found to be slightly faster compared with that of S2p, which cannot be explained by the small difference of inelastic mean free path (16.5, 17.3 Å). The decease of Mo 3d showed that Mo remained more in the substrate and deposited Fe formed sulfide more than Fe-Mo alloy, which is in agreement with a previous result [13].

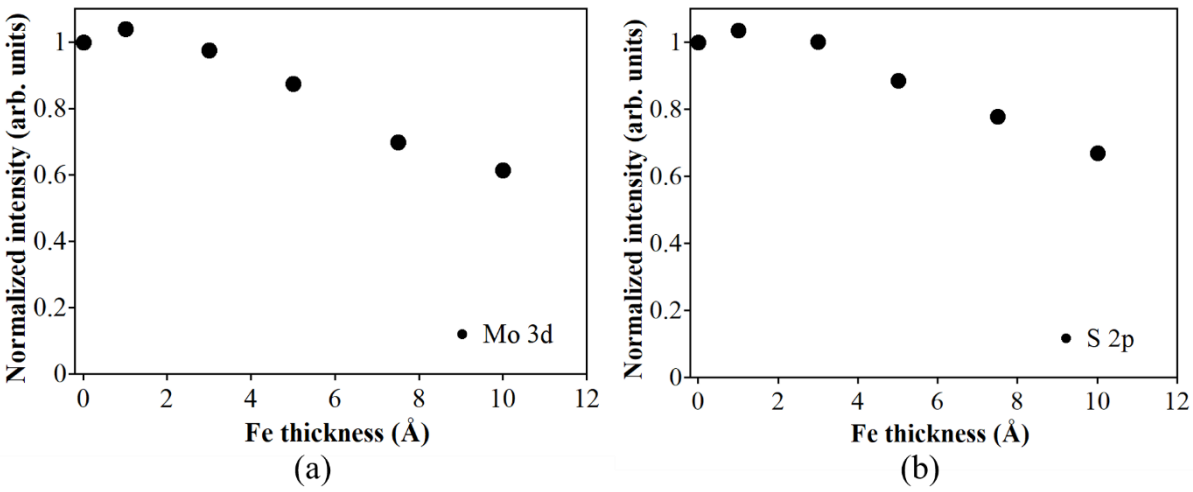

Figure A.7. Peak intensities for (a) Mo3d and (b) S2p core levels with the Fe thickness on MoS_2 substrate.

3.3 Relation between MOKE and XPS analysis

The MDL formation at the interface of Fe/MoS_2 indicated the presence of strong interactions between Fe and MoS_2 at lower thickness of Fe. Despite that, earlier STM results suggested that strong interaction was absent between substrate and metallic atoms at MoS_2 terraces as Fe follows island growth (the Volmer-Weber mode) on MoS_2 and The natural defects present on MoS_2 might interact with Fe atoms and acted as nucleation sites for the generation of nanoparticles [11,21]. It was evident from our MOKE and XPS results that small interaction was existed at the interface between Fe and MoS_2, which would cause to form Fe-S (or Mo) bond and evolve forming compounds, mainly Fe sulfide, with a low thickness of Fe ~2 Å. Afterwards, nano particles tend to form with further Fe deposition. The responsible for MDL formation was the origination of Fe-S (or Mo) bond during lower amount of Fe deposition.

Form MOKE, it was found that MDL formed at the interface of Fe/MoS_2 was evaluated to be very thin, ~2 Å. Magnetization curves obtained from MOKE measurements showed the high remanence for Fe on MoS_2. In addition, XPS results exhibited Fe2p peak broadening at lower thickness of Fe deposition which lead to generate magnetically dead layer. Upon continuation of Fe deposition, metallic phase of Fe2p became dominant at 3 Å which indicated the onset of ferromagnetic Fe growth. Thus, the formation of nano particles initiates at the defect sites, causing an interfacial Fe-S bonding. These nanoparticles are not magnetically stable, having lower Curie temperatures or exhibiting superparamagnetic state, which is in good agreement with the steep drop of the Kerr rotation below 7.5 Å. The MDL at the interface and the difficulty of ideal first Fe layer formation on MoS_2 would explain the observation of the tiny magnetoresistance [24–26].

4. Conclusion

We have studied the magnetic behavior and chemical properties at the interface of Fe/MoS_2 by MOKE and XPS, respectively. It was found that the interface was magnetically dead up to the nominal Fe thickness of 2 Å on MoS_2. The Mo3d and S2p peaks shifted downwards approximately 0.23 eV and 0.24 eV, respectively, up to the nominal Fe thickness 1 Å as observed by XPS analysis, which was due to the band bending. The quick band bending showed that the formation of the interface between Fe and MoS_2 was mostly done in the very initial Fe deposition. On the other hand, Fe2p peak position gradually moved towards lower binding energy with the increase of deposition, which indicated slow transform from ionic to metallic states of Fe. Fe2p peak shape at lower thickness of Fe was significantly broader than that of higher thickness of Fe, reflecting the strong interaction between Fe and MoS_2 at low thickness of Fe. Therefore, the interaction of Fe and Mo or S as revealed by XPS analysis caused non magnetic compounds, magnetically dead layer at the interface, which was consistent with the MOKE measurements. XPS intensity of Mo and S peaks did not decrease at the initial Fe deposition, which is in good agreement with the formation of Fe nano particle and would indicate intercalation of Fe into the substrate. The magnetic dead layer and the Fe nano particle formation at the interface would explain the unexpected lowering of the magneto-resistance at the junction [25].

Background and theory of MOKE

Magneto-optic effect

The phenomena of magnetic-optic effect can be described as the alteration of electromagnetic wave when it propagates through a medium under the influence of magnetic field. Michael Faraday first discovered the magneto-optic effect in 1845 by applying magnetic field on glass [27]. He discovered that the polarization state of transmitted light was changed when it propagated through a magnetic medium. This is known as Faraday effect. While John Kerr observed this magnetic-optic effect in 1877 by examining the polarization state of reflected light from a polished electromagnetic pole, which is known as magneto-optic Kerr effect [28].

Faraday effect:

Faraday effect or Faraday rotation, is a one type of magneto-optical phenomenon which indicates the interaction between light and magnetic field in a magnetic medium.

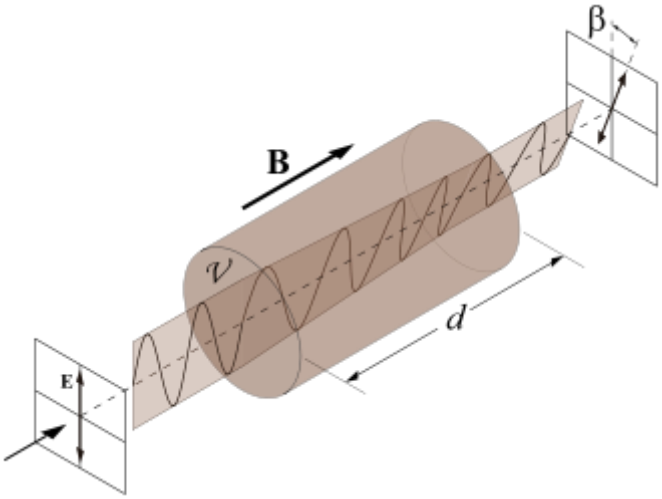

Figure A.8. A schematic view of Faraday effect on linearly polarized light propagating through a magnetic medium with a magnetic field of B.

[β and *v* are the angle of rotation and Verdet constant, respectively.]

The Faraday effect explains the rotation of the polarization plane when a linearly polarized light is passed through a sample placed in parallel direction with the applied magnetic field [29]. The angle of rotation, β, as shown in Figure A.8 is proportional to the applied magnetic field of B with a sample length of d; which can be expressed by the following equation-

$$\beta = \vartheta B d$$

where, ϑ is Verdet constant, which is a property of the transmitting substance.

Magneto-optic Kerr Effect (MOKE)

Magneto-optic Kerr effect (MOKE) demonstrates the reflection of polarized light through a material in magnetic medium which is analogous to Faraday effect. This reflection of light might include different effects, such as, rotation of the direction of polarized light, introduction of ellipticity and change in intensity of the reflected beam. MOKE has been widely utilized to study the ultra-thin magnetic films as well as this is used to investigate magnetic properties of different materials [30,31].

Principle of MOKE:

The MOKE can be described based on the property of rotation and ellipticity. In MOKE analysis, the magneto optical geometry and initial state of light determine the alteration of polarization state of reflected light from magnetic medium. Light is a transverse electromagnetic wave which is formed by oscillating electric and magnetic fields, and it can be polarized into plane, circularly or elliptically. Polarization of light specifies the orientation of oscillations of electric field. The plane of polarization refers to the plane which contains the electric field and the direction of propagation. If the electric field of linearly polarized light is parallel to the plane of incidence, it is known *p*-polarized light and for *s*-polarized light, the electric field is polarized perpendicular to the plane of incidence which as shown in Figure A.9.

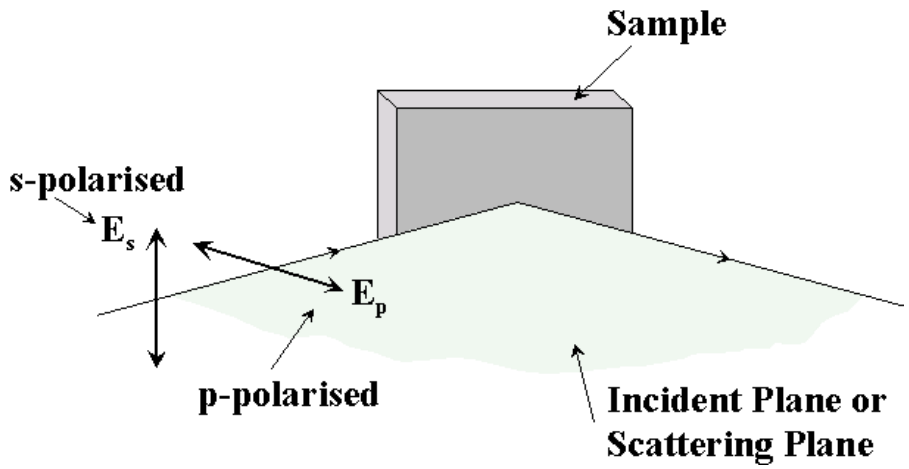

Figure A.9. Schematic illustration of p-polarized and s-polarized light [32].

The reflection of linearly polarized light from a metallic surface is generally elliptically polarized. If p-polarized light is incident upon a metallic surface, the reflected light contains a *p*-component in the ordinary metallic reflection as well as a small *s*-component also appears in the reflected light. This results the linearly polarized light to become elliptically polarized with a rotation with respect to its major axis of incident polarization plane [33]. This magneto optic interaction is depicted in Figure A.10. A similar effect is occurred for *s*-polarized light. These two effects are known as the Kerr ellipticity and the Kerr rotation.

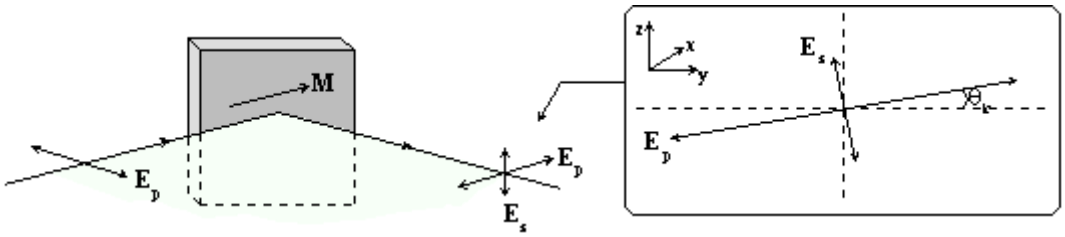

Figure A.10. Illustration of reflected light of p-polarized light form magnetic sample [32].

According to the magneto-optic geometry, MOKE can be classified into three groups-longitudinal, polar and transverse which is shown is Figure A.11. This classification is based on the dependence of the direction of magnetic field on the plane of incidence and

sample surface. For longitudinal MOKE, the magnetic field is parallel to both the plane of incidence and the sample plane, whereas, the magnetic field is perpendicular to the sample plane and is parallel to the plane of incidence in polar MOKE. In transverse MOKE, the magnetization is perpendicular to the plane of incidence and parallel to the sample plane.

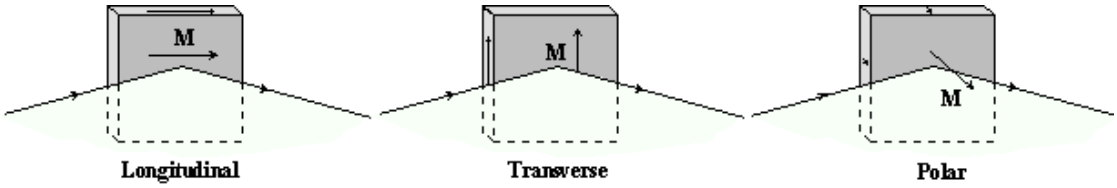

Figure A.11. Three geometries of MOKE- Longitudinal, transverse and polar [32].

For ultrathin magnetic film, when light beam is entered from a nonmagnetic medium to magnetic as shown in Figure A.12, the effect of magnetization can be described using the generalized form of dielectric tensor as follows-

$$\epsilon=\epsilon_{xx}\begin{pmatrix} 1 & -iQm_z & iQm_y \\ iQm_z & 1 & -iQm_x \\ -iQm_y & iQm_x & 1 \end{pmatrix}$$

where, Q is the magneto-optical constant which can be defined as-

$$Q = i\frac{\epsilon_{xy}}{\epsilon_{xx}}$$

and m_x, m_y and m_z are the direction cosines of the magnetization vector M_s. Solving Maxwell equations for the above dielectric tensor, magneto-optical Fresnel reflection matrix can be given as follows [34] –

$$R=\begin{pmatrix} r_{pp} & r_{ps} \\ r_{sp} & r_{ss} \end{pmatrix}$$

where r_{ij} , the ratio of the incident j polarized electric field and reflected i polarized electric field, is expressed by [34,35]-

$$r_{pp} = \frac{n_s \cos\theta_0 - n_0 \cos\theta_2}{n_s \cos\theta_0 + n_0 \cos\theta_2} + \frac{i4\pi n_0 d_1 \cos\theta_0 \,(n_s^2 cos^2\,\theta_1 - n_1^2 cos^2\,\theta_2^2)}{\lambda\,(n_0 \cos\theta_2 + n_s \cos\theta_0)^2}$$

$$r_{sp} = \frac{4\pi n_0 n_1 Q d_1 \cos\theta_0 \,(m_z n_1 \cos\theta_2 + m_y n_s \sin\theta_1)}{\lambda(n_0 \cos\theta_0 + n_s \cos\theta_2)(n_0 \cos\theta_2 + n_s \cos\theta_0)}$$

$$r_{ss} = \frac{n_0 \cos\theta_0 - n_s \cos\theta_2}{n_0 \cos\theta_0 + n_s \cos\theta_2} + \frac{i4\pi n_0 d_1 \cos\theta_0 \,(n_1^2 cos^2\,\theta_1 - n_s^2 cos^2\,\theta_2^2)}{\lambda\,(n_0 \cos\theta_0 + n_s \cos\theta_2)^2}$$

$$r_{ps} = \frac{4\pi n_0 n_1 Q d_1 \cos\theta_0 \,(m_z n_1 \cos\theta_2 - m_y n_s \sin\theta_1)}{\lambda(n_0 \cos\theta_0 + n_s \cos\theta_2)(n_0 \cos\theta_2 + n_s \cos\theta_0)}$$

here, n_0, n_1 and n_s are the refractive indices of the nonmagnetic medium 0, magnetic medium 1 and nonmagnetic medium 2, respectively. θ_0, θ_1 and θ_2 are complex refractive angles of the nonmagnetic medium 0, magnetic medium 1 and nonmagnetic medium 2, respectively.

The complex Kerr effects for s-polarization and p-polarization are defined as follows-

$$\varphi_k^s = \theta_k^s + i\eta_k^s = \frac{r_{ps}}{r_{ss}}$$

$$\varphi_k^p = \theta_k^p + i\eta_k^p = \frac{r_{sp}}{r_{pp}}$$

here,

$\theta_k = Re(\varphi_k)$ is the Kerr rotation

$\theta_k = Im(\varphi_k)$ is the Kerr ellipticity

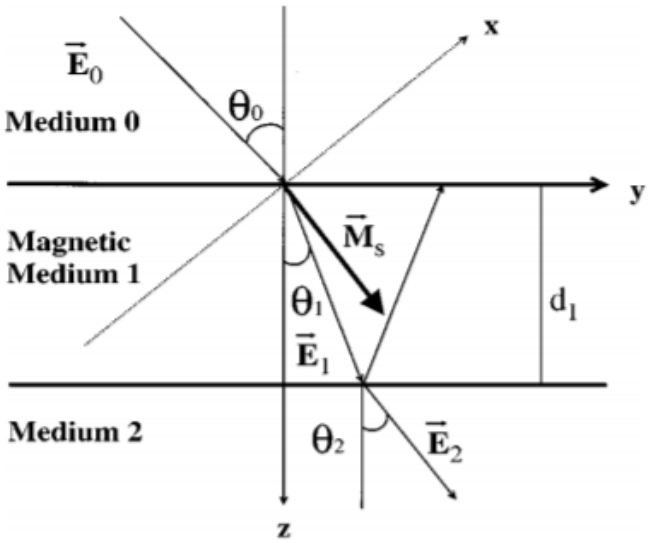

Figure A.12. Coordinate system demonstrating the reflection of light from ultra-thin magnetic film of thickness, d_1.

[Medium 0 and medium 2 are nonmagnetic, and medium 1 is magnetic. The magnetization direction of the medium 1 is arbitrary [34]]

References

[1] P. Bampoulis, R. Van Bremen, Q. Yao, B. Poelsema, H.J.W. Zandvliet, K. Sotthewes, Defect dominated charge transport and fermi level pinning in MoS_2 / metal contacts, ACS Appl. Mater. Interfaces. 9 (2017) 19278–19286. https://doi.org/10.1021/acsami.7b02739.

[2] Z. Cheng, M. Xia, S. Liu, R. Hu, G. Liang, Role of rough substrate on the growth of large single-crystal MoS_2 by chemical vapor deposition, Appl. Surf. Sci. 476 (2019) 1008–1015. https://doi.org/10.1016/j.apsusc.2019.01.211.

[3] S. Qian, R. Yang, F. Lan, Y. Xu, K. Sun, S. Zhang, Materials Science in Semiconductor processing growth of continuous MoS_2 film with large grain size by chemical vapor deposition, Mater. Sci. Semicond. Process. 93 (2019) 317–323. https://doi.org/10.1016/j.mssp.2019.01.007.

[4] S. Jayabal, J. Wu, J. Chen, D. Geng, X. Meng, Metallic 1T- MoS_2 nanosheets and their composite materials: Preparation, properties and emerging applications, Mater. Today Energy. 10 (2018) 264–279. https://doi.org/10.1016/j.mtener.2018.10.009.

[5] X. Li, H. Zhu, Two-dimensional MoS_2 : Properties, preparation, and applications, J. Mater. 1 (2015) 33–44. https://doi.org/10.1016/j.jmat.2015.03.003.

[6] H. Shu, P. Luo, P. Liang, D. Cao, X. Chen, Layer-dependent dopant stability and magnetic exchange coupling of iron-doped MoS_2 nanosheets, ACS Appl. Mater. Interfaces. 7 (2015) 7534–7541. https://doi.org/10.1021/am508843z.

[7] B. Han, Y.H. Hu, MoS_2 as a co-catalyst for photocatalytic hydrogen production from water, Energy Sci. Eng. 4 (2016) 285–304. https://doi.org/10.1002/ese3.128.

[8] W. Xu, S. Yan, W. Qiao, Magnetism in monolayer 1T- $MoS_2$and 1T- MoS_2H tuned by strain, RSC Adv. 8 (2018) 8435–8441. https://doi.org/10.1039/c7ra10304b.

[9] H. Shi, H. Pan, Y. Zhang, B.I. Yakobson, Strong ferromagnetism in hydrogenated monolayer MoS_2 tuned by strain, Phys. Rev. B - Condens. Matter Mater. Phys. 88 (2013) 205305. https://doi.org/10.1103/PhysRevB.88.205305.

[10] H.C. Hsu, C. Bin Wu, K.L. Hsu, P.C. Chang, T.Y. Fu, V.R. Mudinepalli, W.C.

Lin, Surface morphology, magnetism and chemical state of Fe coverage on MoS_2 substrate, Appl. Surf. Sci. 357 (2015) 551–557. https://doi.org/10.1016/j.apsusc.2015.09.079.

[11] C.C. Hsu, C.M. Liu, Z.Y. Lin, W.C. Lin, Morphology and magnetism of CoPd coverage on MoS_2 flakes/SiO_2, J. Alloys Compd. 785 (2019) 436–444. https://doi.org/10.1016/j.jallcom.2019.01.189.

[12] C. Gong, C. Huang, J. Miller, L. Cheng, Y. Hao, D. Cobden, J. Kim, R.S. Ruoff, R.M. Wallace, K. Cho, X. Xu, Y.J. Chabal, Metal contacts on physical vapor deposited monolayer MoS_2, ACS Nano. 7 (2013) 11350–11357. https://doi.org/10.1021/nn4052138.

[13] J.R. Lince, T.B. Stewart, M.M. Hills, P.D. Fleischauer, J.A. Yarmoff, A. Taleb-Ibrahimi, Photoelectron spectroscopic study of the interaction of thin Fe films with the MoS_2 (0001) surface, Surf. Sci. 223 (1989) 65–81.

[14] M.T. Kibria, T. Nomitsu, T. Nakagawa, S. Mizuno, Investigation of magnetic dead layer on iron silicide surfaces, E-Journal Surf. Sci. Nanotechnol. 16 (2018) 101–104. https://doi.org/10.1380/ejssnt.2018.101.

[15] Y. Xu, E. Kernohan, D. Freeland, A. Ercole, M. Tselepi, J. Bland, Evolution of the ferromagnetic phase of ultrathin Fe films grown on GaAs(100), Phys. Rev. B - Condens. Matter Mater. Phys. 58 (1998) 890–896. https://doi.org/10.1103/PhysRevB.58.890.

[16] B. Xia, P. Liu, Y. Liu, D. Gao, D. Xue, D. Jun, Re doping induced 2H-1T phase transformation and ferromagnetism in MoS_2 nanosheets, Appl. Phys. Lett. 113 (2018) 1–6. https://doi.org/10.1063/1.5027535.

[17] C.M. Smyth, S. Mcdonnell, C.L. Hinkle, R.M. Wallace, Contact Metal − MoS_2 Interfacial reactions and potential implications on MoS_2- Based Device Performance, J. Phys. Chem. C. 120 (2016) 14719–14729. https://doi.org/10.1021/acs.jpcc.6b04473.

[18] C. Jiang, Y. Wang, Y. Zhang, H. Wang, Q. Chen, J. Wan, Robust half-metallic magnetism in two-dimensional Fe/ MoS_2, J. Phys. Chem. C. 122 (2018) 21617–21622. https://doi.org/10.1021/acs.jpcc.8b06695.

[19] C.C. Hsu, Z.Y. Lin, P.C. Chang, H.C. Chiu, H.W. Chen, H.L. Liu, F. Bisio, W.C. Lin, Magnetic decoupling of Fe coverage across atomic step of MoS_2 flakes on SiO_2 surface, J. Phys. D. Appl. Phys. 50 (2017). https://doi.org/10.1088/1361-

6463/aa86d2.

[20] J. Li, Z.Y. Wang, A. Tan, P.A. Glans, E. Arenholz, C. Hwang, J. Shi, Z.Q. Qiu, Magnetic dead layer at the interface between a Co film and the topological insulator Bi_2Se_3, Phys. Rev. B - Condens. Matter Mater. Phys. 86 (2012) 2–5. https://doi.org/10.1103/PhysRevB.86.054430.

[21] I.N. Kholmanov, L. Gavioli, M. Fanetti, M. Casella, C. Cepek, C. Mattevi, M. Sancrotti, Effect of substrate surface defects on the morphology of Fe film deposited on graphite, Surf. Sci. 601 (2007) 188–192. https://doi.org/10.1016/j.susc.2006.09.021.

[22] S. Tanuma, C.J. Powell, D.R. Penn, Calculations of electron inelastic mean free paths, Surf. Interface Anal. 37 (2005) 1–14. https://doi.org/https://doi.org/10.1002/sia.1997.

[23] M.T. Kibria, T. Nakagawa, S. Mizuno, Morphology and magnetism of Fe on graphene and thick graphite grown on SiC, Appl. Surf. Sci. 505 (2020) 144209. https://doi.org/10.1016/j.apsusc.2019.144209.

[24] A. Dankert, P. Pashaei, M.V. Kamalakar, A.P.S. Gaur, S. Sahoo, I. Rungger, A. Narayan, K. Dolui, M.A. Hoque, R.S. Patel, M.P. De Jong, R.S. Katiyar, S. Sanvito, S.P. Dash, Spin-Polarized tunneling through chemical vapor deposited multilayer molybdenum disulfide, ACS Nano. 11 (2017) 6389–6395. https://doi.org/10.1021/acsnano.7b02819.

[25] H. Wu, C.Ó. Coileáin, M. Abid, O. Mauit, A. Syrlybekov, A. Khalid, H. Xu, R. Gatensby, J.J. Wang, H. Liu, L. Yang, Spin-dependent transport properties of Fe_3O_4 / MoS_2 / Fe_3O_4 junctions, Nat. Publ. Gr. (n.d.) 1–8. https://doi.org/10.1038/srep15984.

[26] W. Wang, A. Narayan, L. Tang, K. Dolui, Y. Liu, X. Yuan, Y. Jin, Y. Wu, I. Rungger, S. Sanvito, F. Xiu, Spin-valve effect in NiFe/ MoS_2/NiFe junctions, Nano Lett. 15 (2015) 5261–5267. https://doi.org/10.1021/acs.nanolett.5b01553.

[27] T. Haider, A Review of Magneto-optic effects and its application, Int. J. Electromagn. Appl. 7 (2017) 17–24. https://doi.org/10.5923/j.ijea.20170701.03.

[28] J. Kerr, On rotation of the plane of polarization by reflection from the pole of a magnet, London, Edinburgh, Dublin Philos. Mag. J. Sci. 3 (1877) 321–343. https://doi.org/10.1080/14786447708639245.

[29] N. Miura, Magneto-spectroscopy of semiconductors, Compr. Semicond. Sci. Technol. 2 (2011) 256–342. https://doi.org/10.1016/B978-0-44-453153-7

[30] D. Weller, Magneto-optical Kerr spectroscopy of transition metal alloy and compound films, Spin—orbit-influenced Spectrosc. Magn. Solids. (2007) 1–28. https://doi.org/10.1007/bfb0102339.

[31] J. Zak, E.R. Moog, C. Liu, S.D. Bader, Universal approach to magneto-optics, J. Magn. Magn. Mater. 89 (1990) 107–123. https://doi.org/10.1016/0304-8853(90)90713-Z.

[32] M. Ali, Growth And Study Of Magnetostrictive FeSiBC Thin Films For Device Applications, (1999). http://inis.iaea.org/search/search.aspx?orig_q=RN:31036409

[33] T. Nakagawa, Surface Magneto-Optic Kerr Effect, Compend. Surf. Interface Anal., Springer Singapore, Singapore, (2018) 667–671. https://doi.org/10.1007/978-981-10-6156-1_108.

[34] C.-Y. You, S.-C. Shin, Generalized analytic formulae for magneto-optical Kerr effects, J. Appl. Phys. 84 (1998) 541–546. https://doi.org/10.1063/1.368058.

[35] Z.Q. Qiu, S.D. Bader, Surface magneto-optic Kerr effect (SMOKE), J. Magn. Magn. Mater. 200 (1999) 664–678. https://doi.org/10.1016/S0304-8853(99)00311-X.

Acknowledgements

In the journey of my doctoral study, I am blessed to be surrounded by many people who gave me enormous support, care, advice, and encouragement to make this phase of my life better. I want to express my deepest gratitude to all of them.

First and foremost, I would like to express my heartfelt gratitude and indebtedness to my supervisor, *Assoc. Prof. Takeshi Nakagawa* for his guidance and continuous support throughout my Ph.D tenure. It has been a great opportunity for me to work under his supervision.

I am very grateful to *Prof. Seigi Mizuno* for being so supportive and helpful. His advices helped me a lot to improve my academic knowledge. Also, I would to thank *Prof. Hiroki Ago* and *Prof. Tsuyoshi Yoshitake* for giving their valuable time to evaluate my PhD dissertation.

I would like to express my gratitude to the Japanese Government (MEXT) and IEI program of Kyushu University for providing scholarship with a wonderful curriculum.

I am thankful to all my present and former laboratory members for their help and kindness. Especially, I would like to thank *Dr. Tawheed Kibria Siam*, *Dr. Rezwan Ahmed*, *Mr. Shahadat Hossain*, *Guansong Peng* and *Shohei Maeyama* for being so helpful and supportive.

My special gratitude goes to *Prof. Bidyut Baran Saha* and his wife, *Mrs. Tandra Bhuiyan Saha* for their support and care which make my life in Japan very comfortable.

I consider myself fortunate for being a part of a wonderful family with all supportive members who are always by my side. I am very grateful to my parents, *Md. Fazlul Hoque*, and *Monowara Hoque* for their inspiration and everything they have done for me. I am thankful to my siblings, *Farzana Jesmin Mili* and *Moinul Hoque Mamun* for understanding me and keeping me inspired always. I am also very thankful to my In-Laws for their love and support. I would like to thank my husband *Tahmid Hasan Rupam* especially for his continuous support and encouragement. My baby boy, *Tahiyaan Tarif Rayeen*, is my most precious inspiration to face the hard times.

Finally, I am thankful to my Almighty for everything.

List of publications:

1. **Farhana Jesmin Tuli**, Mohammad Tawheed Kibria, Takeshi Nakagawa, and Seigi Mizuno, "Interfacial magnetic behaviors and chemical states of Fe grown on MoS_2", *Physica Status Solidi B,* 2100124 (2021).
2. **Farhana Jesmin Tuli**, Guansong Peng, Shahadat Hossain, Kakeru Ninomiya, Rezwan Ahmed, Takeshi Nakagawa, and Seigi Mizuno, "Formation of ordered B structure on W(100)", *Surface Science,* 713, 121906 (2021).

List of publication in preparation:

1. **Farhana Jesmin Tuli**, Guansong Peng, Shahadat Hossain, Takeshi Nakagawa, and Seigi Mizuno, **"**Novel phase of two dimensional B sheet on Mo(110)".

List of conference articles:

1. **Farhana Jesmin Tuli**, Mohammad Tawheed Kibria, Takeshi Nakagawa, and Seigi Mizuno, "Interfacial magnetic properties of Fe deposited on MoS_2 flakes", *International Exchange and Innovation Conference on Engineering & Sciences (IEICES),* 5, October 24-25th 2019, Interdisciplinary Graduate School of Engineering Sciences, Kyushu University, Japan.
2. **Farhana Jesmin Tuli**, Takeshi Nakagawa, and Seigi Mizuno, "Observation of surface magnetism and chemical properties of Fe on molybdenum disulfide", *21st Cross Straits Symposium on Energy and Environmental Science,* November 24-26th 2019, Shanghai Jiao Tong University, Shanghai, China.
3. Shahadat Hossain, **Farhana Jesmin Tuli**, Peng Guansong, Takeshi Nakagawa, and Seigi Mizuno, "Surface relaxation of W(110) and 2D growth of B studied by low energy electron diffraction and Auger electron spectroscopy". *International Exchange and Innovation Conference on Engineering & Sciences (IEICES),* 6, October 22-23th 2020, Interdisciplinary Graduate School of Engineering Sciences, Kyushu University, Japan,
4. **Farhana Jesmin Tuli**, Shahadat Hossain, Peng Guansong, Takeshi Nakagawa, and Seigi Mizuno, "LEED study of clean and boron induced reconstructed surface of W(100)", *22nd Cross Straits Symposium on Energy and Environmental Science,* December 02-03rd 2020, Kyushu University, Japan
5. Shahadat Hossain, **Farhana Jesmin Tuli**, Takeshi Nakagawa, and Seigi Mizuno, "Two-dimensional growth mechanism for boron on W(110) surface", *22nd Cross*

Straits Symposium on Energy and Environmental Science, December 02-03rd 2020, Kyushu University, Japan.

6. **Farhana Jesmin Tuli**, Shahadat Hossain, Peng Guansong, Takeshi Nakagawa, and Seigi Mizuno, "Structure determination of boron on W(100) by low energy electron diffraction", *Interdisciplinary Surface Science Conference-23*, April 19-21th 2021, Institute of Physics, London.